A Consistent Segment Procedure for Solution of 2D Contact Problems with Large Displacements

by

Mirza Muhammad Ali Irfan Baig
Bachelor of Science in Civil Engineering
University of Engineering & Technology, 1999

Master of Science in Civil and Environmental Engineering
Massachusetts Institute of Technology, 2003

Submitted to the Department of Civil and Environmental Engineering
in partial fulfillment of the requirements
for the degree of
Doctor of Science in the field of Structures and Materials
at the
MASSACHUSETTS INSTITUTE OF TECHNOLOGY
February 2006

Author .....
Department of Civil and Environmental Engineering
January 10, 2006

Certified by .....
Klaus-Jürgen Bathe
Professor of Mechanical Engineering
Thesis Supervisor

Certified by .....
Eduardo Kausel
Professor of Civil and Environmental Engineering
Chairperson, Doctoral Thesis Committee

Accepted by .....
Andrew J. Whittle
Chairman, Department Committee on Graduate Students

A Consistent Segment Procedure for Solution of 2D Contact Problems with Large Displacements

by

Mirza Muhammad Ali Irfan Baig

Submitted to the Department of Civil and Environmental Engineering
on January 10, 2006, in partial fulfillment of the
requirements for the degree of
Doctor of Science in the field of Structures and Materials

Abstract

Solution of contact problems in solid mechanics using the finite element method is a challenging and non-trivial task. Stable and efficient contact algorithms are required for effective solution of general problems. In this thesis, a general algorithm is presented for the analysis of contacting bodies undergoing large displacements. A sub-segment approach is adopted, which allows the algorithm to pass the contact patch test. Passing the patch test is a fundamental requirement for optimal convergence of the finite element solution. The algorithm is a Lagrange-multiplier based one, with the contact tractions as the additional variables to be solved for. Interpolation orders for which the resulting mixed formulation remains stable and optimal are used to interpolate the contact traction variables. The inequality constraints arising in contact conditions are regularized using the constraint function method.

Implicit time integration schemes are attractive for dynamic analysis of structures and solids when the response lies in the lowest few modes. But the schemes then have to be unconditionally stable to be able to utilize reasonably large time step sizes. Widely used schemes that are unconditionally stable in linear analysis, do not remain so in nonlinear analysis. A simple composite direct time integration scheme is presented which remains stable for long duration analyses involving large displacements. The nature of the method also makes it attractive for use in dynamic analysis involving contact. The numerical schemes presented are validated using example problems.

Thesis Supervisor: Klaus-Jürgen Bathe
Title: Professor of Mechanical Engineering

Chairperson, Doctoral Thesis Committee: Eduardo Kausel
Title: Professor of Civil and Environmental Engineering

Acknowledgments

My unbounded thanks to God, who gave me the strength and will, to go through the very rewarding experience of a graduate program.

I would like to express my deep gratitude to my thesis supervisor Prof. Klaus-Jürgen Bathe for the last three years that I have spent as a member of his research group. His tutelage has been of immense value to me in my endeavors to understand computational mechanics in general, and the finite element method in particular. I am proud to have learnt a lot from him, and hope that his quest for advancing the state of the art in computational mechanics has left its mark on me. My sincerest thanks go to my doctoral committee chairperson Prof. Eduardo Kausel; he has always been available for advice and mentoring whenever I walked into his office. Also many thanks to my thesis committee member Prof. Jerry Connor who has always given very kind and valuable advice during my stay at MIT.

I also want to say my thanks to my friends and colleagues in the finite element research group, for their friendship and support. I must thank Phill-Seung Lee for his valuable advice and support in my research. He was the first friend I made at MIT, and remains so more than ever. Moreover, Jean-Francois Hiller, Jung-Wuk Hong, Bahareh Banijamali, Commander Jacques Olivier, Seongwa Park, Omri Pedzatur and Sebastian Meißner, all made the atmosphere of the lab most enjoyable and pleasant. In particular, the time I spent with Thomas Grätsch, discussing and learning the mathematical theory of finite elements and understanding different aspects more clearly, was amongst the most enjoyable I had. Many discussions with Prof. Francisco Montans, about different implementation aspects of the finite element method helped me greatly in my work. Prof. Uwe Ruppel's always deep, thought evoking comments about our work, and science in general were also very interesting and valuable.

Over the years that we have spent in Cambridge/Boston, we have come across numerous people who have, at one time or another, helped me and extended their unwavering support to me, and my family. Especially I want to thank Dr. Iqbal Ahmed and Imrana Iqbal, for the friendship and love they extended to us.

All these years, my parents-in-law have been a great source of encouragement for me. I am deeply grateful to them for the love they have given me and the support and understanding they have extended during this period.

My parents have always given me tremendous support. Were it not for them, I could never have made it to MIT. It was my father who persuaded me come to MIT, always telling me to believe in myself, wanting me to never settle for anything but the best. I am glad I did not let him down.

Finally I must say that I certainly could not have succeeded in this endeavor were it not for the love, patience and understanding of my wife Faiza and son Junaid. They have both waited and endured endless hours, days, without my giving them any time that was more than their due. Especially Junaid, who even though only a toddler, always understood when "daddy" was busy, and never complained about lack of attention. Little Aleena with her coming in this world, brightened up things immensely. I am truly blessed to have such a family. Thank you !

Contents

1 Introduction **14**

1.1 Thesis Outline 16

2 Contact Kinematics **18**

2.1 Motivation 18

2.2 Continuum Mechanics Equations 19

2.3 The Constraint Equations 23

2.4 Linearization of the Contact Integral 26

2.4.1 Linearization of Normal Contact 27

2.4.2 Linearization of Tangential Contact 30

2.5 Linearization of the Constraint Equations 33

3 A Consistent Segment Algorithm (CSA) **35**

3.1 Motivation 35

3.2 Finite Element Discretization 36

3.3 Consistent Segment Algorithm 38

3.4 Choice of Contactor and Target Surfaces 43

3.5 Numerical Solutions 45

3.5.1 The Patch Test 45

3.5.2 The Punch Problem 53

3.5.3 Hertzian Contact 57

3.5.4 Sheet in a Converging Channel 61

4 Direct Time Integration: Nonlinear Dynamics **66**

4.1 Motivation 66

4.2 A Composite Trapezoidal-Backward-Difference Procedure 70

4.3 Generalization of the Composite Scheme 72

4.4 Accuracy of Analysis 73

4.5 Numerical Examples 75

4.5.1 Rotating Plate 75

4.5.2 Compound Pendulum 77

4.5.3 Cantilever Beam 83

4.6 Conclusions 90

5 Dynamic Contact **95**

5.1 Motivation 95

5.2 Two Impacting Bars 96

5.3 Shaking Table 98

6 A 3D Model Friction Problem and its Solution **113**

6.1 Motivation 113

6.2 Frictional Sliding on a Plane 114

6.3 Numerical Algorithm 116

6.4 Linearization of Governing Equations 118

6.5 Numerical Results 120

6.5.1 Accuracy of Solution 124

6.5.2 Convergence of Newton-Raphson Iterations 127

6.5.3 Variable Normal Force N 130

6.6 Conclusions 131

7 Conclusions **133**

A Energy and Momentum Conservation **136**

List of Figures

2-1 Two bodies in contact. 20

2-2 Contact kinematics of contact pair. 22

2-3 Contact conditions. 23

2-4 Constraint function for normal contact. 25

2-5 Constraint function for tangential contact. 26

3-1 End nodes of target segment projected on contactor segment to create sub-segments. 39

3-2 Choice of contactor and target surfaces; (a) top surface contactor, (b) bottom surface contactor. 44

3-3 The patch test. 46

3-4 The patch test; oscillatory vertical displacement field obtained using the node-to-segment scheme. 47

3-5 The patch test; vertical stress field obtained using the node-to-segment scheme. 47

3-6 The patch test; a uniformly linearly varying vertical displacement field obtained using the consistent segment algorithm. 48

3-7 The patch test; constant vertical stress field obtained using the consistent segment algorithm. 48

3-8 The patch test; incorrect displacement field using node-to-segment scheme; top block contactor. 49

3-9 The patch test; vertical stress field obtained using the node-to-segment scheme; top block contactor. 49

3-10 The patch test; displacement field using consistent segment scheme; top block contactor. 50
3-11 The patch test; vertical stress field obtained using the consistent segment scheme; top block contactor. 50
3-12 The patch test; displacement field using node-to-segment scheme; top block contactor, 9-node elements. 51
3-13 The patch test; vertical stress field obtained using the node-to-segment scheme; top block contactor, 9-node elements. 51
3-14 The patch test; displacement field using consistent segment scheme; top block contactor, 9-node elements. 52
3-15 The patch test; vertical stress field obtained using the node-to-segment scheme; top block contactor, 9-node elements. 52
3-16 The elastic punch problem. 54
3-17 The elastic punch; horizontal stress field, using top and lower body as contactor. 55
3-18 The elastic punch; vertical stress field, using top and lower body as contactor. 55
3-19 The elastic punch problem; contact pressure distribution. 56
3-20 Hertzian contact problem. 57
3-21 Hertzian contact problem; horizontal stress field, 4-node elements. . . 58
3-22 Hertzian contact problem; vertical stress field, 4-node elements. . . . 58
3-23 Hertzian contact problem; horizontal stress field, 9-node elements. . . 59
3-24 Hertzian contact problem; vertical stress field, 9-node elements. . . . 59
3-25 Hertzian contact problem; contact pressure distribution. 60
3-26 Sheet in a converging channel. 61
3-27 Normal traction using 4-node elements; $\mu = 0.0$. 62
3-28 Normal traction using 9-node elements; $\mu = 0.0$. 62
3-29 Tractions at times $t = 4$ and 8 s.; 4-node elements; $\mu = 0.3$. 63
3-30 Tractions at times $t = 9$, 10 and 16 s.; 4-node elements; $\mu = 0.3$. . . . 63
3-31 Tractions at times $t = 4$ and 8 s.; 9-node elements; $\mu = 0.3$. 64

3-32 Tractions at times $t = 9$, 10 and 16 s.; 9-node elements; $\mu = 0.3$. . . . 64
3-33 Comparison between CSA and NTS; $t = 9$ s.; 9-node elements; $\mu = 0.3$. 65
3-34 Comparison between CSA and NTS; $t = 10$ s.; 9-node elements; $\mu = 0.3$. 65

4-1 Convergence curve for the composite scheme. 73
4-2 Percentage period elongation and amplitude decay for the trapezoidal rule, the Wilson method, the two sub-step composite scheme ($\gamma = 0.5$), and the original composite algorithm. 74
4-3 The rotating plate problem. 76
4-4 The rotating plate problem; results using the trapezoidal rule; $\Delta t = 0.02\,s$. 78
4-5 The rotating plate problem; results using the composite scheme; $\Delta t = 0.4\,s$. 79
4-6 The rotating plate problem; results using the Wilson θ-method; $\Delta t = 0.02\,s$. 80
4-7 The rotating plate problem; results using the three sub-step composite scheme; $\Delta t = 0.4\,s$. 81
4-8 The compound pendulum in its initial configuration. 82
4-9 The compound pendulum; results using the trapezoidal rule; $\Delta t = 0.005\,s$. 84
4-10 The compound pendulum; results using the composite scheme; $\Delta t = 0.01\,s$. 85
4-11 The compound pendulum; results using the composite scheme; $\Delta t = 0.02\,s$. 86
4-12 The compound pendulum; results using the composite scheme; $\Delta t = 0.04\,s$. 87
4-13 The compound pendulum; results using the Wilson θ-method; $\Delta t = 0.005\,s$. 88
4-14 The compound pendulum; results using the Wilson θ-method; $\Delta t = 0.02\,s$. 89

4-15 Cantilever beam modeled using 9-node elements 90
4-16 Cantilever beam; results using the trapezoidal rule; $\Delta t = 0.002\,s$. . . . 91
4-17 Cantilever beam; results using the composite scheme; $\Delta t = 0.004\,s$. . 92
4-18 Cantilever beam; results using the Wilson θ-method; $\Delta t = 0.002\,s$. . . 93

5-1 Two impacting bars. 96
5-2 The displacements of contacting faces; trapezoidal rule, $\Delta t = 0.00004$ s. 97
5-3 The velocities of contacting faces; trapezoidal rule, $\Delta t = 0.00004$ s. . 98
5-4 The displacements of contacting faces; composite scheme, $\gamma = 0.5$, $\Delta t = 0.00008$ s. 99
5-5 The velocities of contacting faces; composite scheme, $\gamma = 0.5$, $\Delta t = 0.00008$ s. 99
5-6 The total energy of the two bars obtained using the trapezoidal rule. 100
5-7 The total energy of the two bars obtained using the composite scheme. 100
5-8 The shaking table problem. 101
5-9 The velocity response of the table and the block; $p = 0$. 102
5-10 The displacements of the table and the block; $p = 0$. 103
5-11 The acceleration response of the block; $p = 0$. 103
5-12 The normal contact distributions (for all time steps), 4-node elements; $p = 0$. 104
5-13 The frictional contact distributions (for all time steps), 4-node elements; $p = 0$. 104
5-14 The normal contact distributions (for all time steps), 9-node elements; $p = 0$. 105
5-15 The frictional contact distributions (for all time steps), 9-node elements; $p = 0$. 105
5-16 The velocity response of the table and the block; $p = 50000$. 106
5-17 The acceleration response of the block; $p = 50000$. 106
5-18 The normal contact distributions (for all time steps), 4-node elements; $p = 50000$. 107

5-19 The frictional contact distributions (for all time steps), 4-node elements; $p = 50000$. 107
5-20 The normal contact distributions (for all time steps), 9-node elements; $p = 50000$. 108
5-21 The frictional contact distributions (for all time steps), 9-node elements; $p = 50000$. 108
5-22 The velocity response of the table and the block; $p = 35000$. 109
5-23 The velocity response of the table and the block; $p = 35000$. 110
5-24 The acceleration response of the block; $p = 35000$. 110
5-25 The normal contact distributions (for all time steps), 4-node elements; $p = 35000$. 111
5-26 The frictional contact distributions (for all time steps), 4-node elements; $p = 35000$. 111
5-27 The normal contact distributions (for all time steps), 9-node elements; $p = 35000$. 112
5-28 The frictional contact distributions (for all time steps), 9-node elements; $p = 35000$. 112

6-1 Frictional sliding of a point mass. 115
6-2 Time functions governing the variation of applied loads. 115
6-3 Coulomb friction condition. 116
6-4 Regularization of Coulomb friction by constraint function. 118
6-5 The surface generated by the constraint function in Eq. (6.8). The thick line corresponds to $w_t = 0$. 119
6-6 The derivative of w_t w.r.t. $\dot{u}$, $\frac{\partial w_t}{\partial \dot{u}}$; for $w_t = 0$. 121
6-7 The derivative of w_t w.r.t. τ, $\frac{\partial w_t}{\partial \tau}$; for $w_t = 0$. 121
6-8 The trajectory of point A, under the action of applied loads; $\Delta t = 1$, $\epsilon_t = 10^{-5}$, $N = 1$. 122
6-9 Plot of incremental applied load vectors; $\Delta t = 1$. 123
6-10 Plot of incremental friction force vectors; $\Delta t = 1$, $\epsilon_t = 10^{-5}$, $N = 1$. . 123

6-11 Plot of incremental internal spring force vectors; $\Delta t = 1$, $\epsilon_t = 10^{-5}$, $N = 1$. 124
6-12 Plots of incremental load, spring force and friction force vectors at each time step; the three incremental force vectors are in equilibrium. . . . 125
6-13 Comparison of the trajectory of point A, for different values of time step size Δt; $\epsilon_t = 10^{-5}$; (for total duration of $2\,s$). 126
6-14 Comparison of the trajectory of point A, obtained using $\Delta t = 1$ and $\Delta t = 0.1$; (for total duration of $8\,s$). 126
6-15 Plot of incremental friction force vectors; $\Delta t = 0.1$, $\epsilon_\tau = 10^{-5}$, $N = 1$. The circle shows the limiting value for the frictional force magnitude; at no time is this threshold violated. Points lying within the circle indicate a stick condition. 127
6-16 Comparison of trajectory of point A, for different values of ϵ_t; time step size $\Delta t = 0.1$, $N = 1$. 129
6-17 Variation of normal force; $N = 1 + 0.8\sin(20x)\cos(20y)$. 130
6-18 Comparison of trajectories obtained; $\epsilon_t = 10^{-3}$, $\Delta t = 0.1$. 131

List of Tables

6.1 Convergence norms for some time steps; $\Delta t = 1$, $\epsilon_t = 10^{-5}$, $N = 1$ . . 128

6.2 The 'radial return algorithm' for the solution of the model problem . 132

Chapter 1

Introduction

Frequently in engineering analysis, there arise situations where in order to have an accurate solution of the problem at hand, actual contact conditions between structural or solid elements have to be considered. Contact problems, by their very nature are highly nonlinear, since not only the contact tractions are unknown, but also the surface area of the contacting bodies over which these act is also not known a priori. Among the many practical applications of contact analysis are soil-structure interactions, bio-mechanical engineering, metal forming processes, and crash analyses. For many applications it may be sufficient to consider frictionless contact, but in other instances the consideration of friction may be of utmost importance.

Numerical solution of contact problems is a difficult task, and efficient and robust techniques need to be utilized for reliable solution of general problems. Much research effort has been directed towards developing such schemes since early developments in the finite element method. Generally the techniques that are used to satisfy the contact conditions are the Lagrange multiplier method and the penalty method.

In the Lagrange multiplier method the contact conditions are satisfied by the introduction of auxiliary variables, i.e. the Lagrange multipliers, which turn out physically to be the contact traction variables at the contacting surfaces. The contact conditions are satisfied exactly, but the degrees of freedom now increase by the number of unknown contact traction variables, leading to greater computational effort. Bathe and Chaudhary [8, 14] presented an effective scheme based on this approach. The

Lagrange multiplier method transforms the problem formulation into a mixed method, and care needs to be taken regarding the optimality and stability of the method, i.e. the *inf-sup* condition has to be satisfied, see Brezzi and Fortin [13] for a detailed account regarding mixed methods in general, and Bathe and Brezzi [7] for contact problems in particular. Also for a comprehensive treatment of the Lagrange multiplier method and other optimization techniques see Bertsekas [12].

Penalty methods weakly enforce the contact conditions by introduction of a parameter of large value into the governing equations of equilibrium for the contacting bodies. This penalty parameter acts like a large spring stiffness, see Bathe [3] and Zienkiewicz and Taylor [43]. The main attraction of the penalty method is that the total number of degrees of freedom remains unchanged. The contact conditions are enforced with increased accuracy as the penalty parameter goes to infinity. However there is a potential for ill-conditioning of the coefficient matrix as this limit is approached. The approach has been used extensively, e.g. Oden [33]. Among recent works, the formulation based on mortar methods by Yang *et. al.* [42] utilizes penalty approach to satisfy contact constraints.

Augmented Lagrange methods combine both the Lagrange and penalty methods to regularize the contact conditions, see Kikuchi and Oden [25]. The approach has also been used for large deformation contact problems including friction, see for example Laursen and Simo [31]. Perturbed Lagrangian methods add a quadratic function of the Lagrange multipliers to the Lagrange multiplier term, see e.g. Simo *et al.* [37]. For a comprehensive survey of various techniques and algorithms for enforcing contact conditoins, see Wriggers [41] and the references therein.

In this thesis, a Lagrange multiplier based approach is adopted. A segment approach first proposed by El-Abbasi and Bathe [18], is extended for solution of large displacement, kinematically nonlinear problems. The contact tractions are interpolated to the same order as that of the underlying continuum finite elements, leading to optimal convergence and stability, see El-Abbasi and Bathe [18] and Bathe and Brezzi [7]. The constraint function method first proposed by Eterovic and Bathe [21] is used to convert inequalities in the contact conditions into equality constraints.

This enables the algorithm to detect contact conditions while still away from contact event, allowing the use of larger time steps, see Eterovic [19].

1.1 Thesis Outline

In Chapter 2, the basic continuum mechanics equations including the contact tractions are presented. The physical constraints that are imposed by the presence of contact are given, including frictional effects. The constraint functions that are used to enforce contact conditions are presented. The constraint functions convert the inequality constraints arising from contact conditions into equality constraints, and also regularize the non-smooth contact conditions at the same time. The contact integral that appears in the equation of principle of virtual work is linearized for subsequent application of Newton-Raphson method for the iterative solution. Detailed expressions for linearization of all the terms that appear in the contact integral is presented. The constraint equations which are obtained by multiplying the constraint functions by suitable weight functions are also linearized with respect to the unknown solution variables.

In Chapter 3, the scheme for projecting target segments onto contactor segments is given, along with appropriate finite element approximations for the contact surface and the contact traction variables. Expressions for finite element matrices obtained are also given. The chapter is concluded with numerical examples that show the performance of the algorithm.

Chapter 4 summarizes the difficulties usually encountered in the solution of nonlinear dynamic problems using an implicit direct integration method. A simple but effective composite time integration approach is presented that produces stable solutions of nonlinear dynamic problems involving large displacements for long time durations. The scheme performs well in instances where other widely used implicit direct integration methods exhibit instability. Numerical examples are solved to demonstrate the stability of the integration scheme.

In Chapter 5 numerical examples involving dynamic contact problems are solved

using the contact solution algorithm given in Chapter 3, with the composite time integration scheme of Chapter 4. The stability characteristics of the time integrator also stabilize the solution at the instant of contact events, and it is observed that no special post processing of the response at contacting nodes is required. Large sliding response with friction, showing transition from stick to slip conditions, and vice versa, is also observed to be resolved accurately.

In Chapter 6 a model 3D friction sliding problem and its solution are considered. The constraint function method is used to enforce the Coulomb friction model. The problem is solved for different time step sizes, constraint function parameter values, and normal loads. Difficulties in Newton-Raphson convergence are observed and the use of line search in each iteration is suggested as a remedy to the problem.

Finally in Chapter 7 conclusions are given and possible future work regarding the contact solution algorithm is suggested.

Chapter 2

Contact Kinematics

2.1 Motivation

We seek to state the continuum mechanics formulation for the problem of elastic bodies coming into contact. More specifically, we will consider the case of two bodies coming into mutual contact, but extension to multiple contacting bodies is straightforward and only involves the application of the formulations stated by considering each contacting pair successively.

The goal of the present work is to have a general formulation for bodies undergoing large displacements (and possibly large strains). The nonlinearity due to contact phenomena is due to the fact that the contact tractions at the interface are obviously not known a priori, but also because the actual contact area is unknown. The contact area can be dependent on the contact tractions and on the external applied forces driving the bodies to come into contact. Also large sliding can take place at the contact interface resulting in large changes in relative positions of points lying on contacting surfaces. It is of great importance that the kinematics of all the varying quantities at the contact interface be considered and included in the formulation, to capture the correct behavior. For a more general treatment, see Wriggers [41]. In the following sections we state the contact kinematics with reference to 2-D contact between two bodies, and enforce the contact constraints by means of the constraint function method, Eterovic and Bathe [21]. Also, to solve the nonlinear problem,

one has to use an iterative procedure for the solution of resulting equations. Full Newton-Raphson method will be employed, which converges quadratically to the exact solution, provided the required conditions of smoothness and continuity are satisfied, see Bathe [3] and Bertsekas [12] for details. For this reason, it is necessary that all kinematic variables be linearized exactly, so that consistent tangent stiffness matrices can be obtained and the quadratic convergence property can be utilized.

2.2 Continuum Mechanics Equations

In this section the general continuum mechanics equations for bodies coming into contact are presented. Although, in general more than two bodies can come into mutual contact, in the following we consider the case of only two bodies. All the discussion is also directly applicable for multi-body contact, with kinematics of each contact surface pair treated in the same manner as given in this chapter.

We consider two bodies Ω^i, $i = I, J$, which are in contact at time t. For each body, S_u is the surface over which Dirichlet boundary conditions are specified, and S_f the surface with Neumann boundary conditions. We denote by S^I the surface area of body I that can come into contact with body J, and S^J the surface of body J that can potentially be in contact with S^J. Together S^I and S^J make a contact surface pair. Let ${}^tS_c$ be the actual contact area common to both S^I and S^J at the time of consideration. Following the approach in Bathe[3] the principle of virtual work for the two bodies is:

$$\text{Find} \quad {}^t\mathbf{u} \in \mathcal{V} \quad \text{where} \quad \mathcal{V} \quad \text{is defined as}$$

$$\sum_i \left\{ \int_{{}^0V} {}^t_0\mathbf{S} \cdot \delta {}^t_0\boldsymbol{\epsilon} \, d^0V \right\} = \sum_i \left\{ \int_{{}^tV} {}^t\mathbf{f}^B \cdot \delta\mathbf{u} \, d^tV + \int_{{}^tS_f} {}^t\mathbf{f}^S \cdot \delta\mathbf{u}^S \, d^tS \right\} + \underbrace{\int_{{}^tS_c} {}^t\mathbf{f}^{JI} \cdot (\delta\mathbf{u}^J - \delta\mathbf{u}^I) \, d^tS}_{\text{the contact integral}} \tag{2.1}$$

$$\forall \, \delta\mathbf{u} \in \mathcal{V} \quad \text{where } \mathcal{V} \text{ is defined as}$$

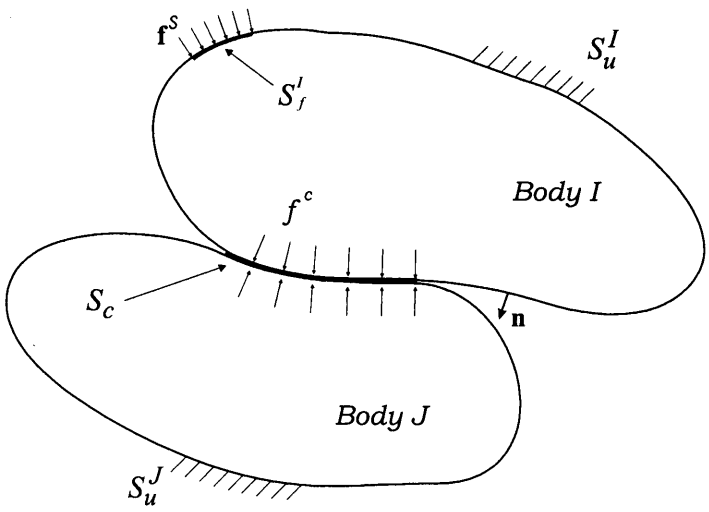

Figure 2-1: Two bodies in contact.

$$\mathcal{V} = \{\mathbf{v} | \mathbf{v} \in H^1(\Omega), \mathbf{v}|_{S_u} = 0, (\mathbf{v}^J - \mathbf{v}^I) \cdot \mathbf{n} + g_0 \geq 0\}$$

where $\mathbf{n}$ is a normal unit vector to be defined, and g_0 is a possible initial gap. The left hand side of the above equation represents the total internal virtual work, expressed in terms of second Piola-Kirchhoff stresses and the Green-Lagrange strains calculated at time t. The first integral on the right hand side is the total external virtual work done by the body forces and any externally applied surface tractions. The second integral on the right hand side is the contribution from the contact tractions which act on both the bodies over the surface ${}^tS_c$ in equal and opposite directions. ${}^t\mathbf{f}^{JI}$ is the vector of contact surface tractions acting on body J due to body I. Over the surface of contact we have from the principle of equal and opposite reactions ${}^t\mathbf{f}^{IJ} = -{}^t\mathbf{f}^{JI}$. This results in the compact form of the contact integral in the above equation. In the following discussion we are only concerned with the evaluation of the contact integral since this is the key step in the evaluation of contact tractions and displacements of the contacting bodies. We designate surface S^I as the *contactor* and surface S^J as the *target*. Also ${}^t\mathbf{f}^{JI}$ is replaced by ${}^t\mathbf{f}^c$ in the following discussion. In a continuum setting, it makes no difference now, whether the contact integral is evaluated over the target surface or the contactor surface since the actual area of contact ${}^tS_c$ at time t is the same no matter which surface is chosen. For a discretized problem, of course

there is a bias introduced depending on which surface is chosen for integration. In this work, the contactor surface S^I is chosen as the surface over which the contact integral will be evaluated.

Let $\mathbf{s}$ be the tangent vector at a point on S^I. Then the unit normal $\mathbf{n}$ is defined over S^I such that $\mathbf{n}$ and $\mathbf{s}$ form a right hand basis

$$\mathbf{n} = \mathbf{s} \times \mathbf{e} \tag{2.2}$$

where $\mathbf{e}$ is the unit out of plane vector. Now the vector of contact tractions acting on S^J can be decomposed as

$$^t\mathbf{f}^c = \lambda \mathbf{n} + t\mathbf{s} \tag{2.3}$$

We refer to a point by its position vector in the following discussion, see Figure 2-2. In order to define the signed distance from a point $\mathbf{x}^I$ on contactor surface S^I to the target surface S^J, we solve the following expression for $\mathbf{x}^J$

$$(\mathbf{x}^J - \mathbf{x}^I) \cdot \mathbf{s} = 0 \tag{2.4}$$

then

$$g\mathbf{n} = (\mathbf{x}^J - \mathbf{x}^I) \tag{2.5}$$

The signed distance or *gap function* is now given by

$$g = (\mathbf{x}^J - \mathbf{x}^I) \cdot \mathbf{n} \tag{2.6}$$

We parameterize the contactor surface by a local variable r and evaluate the variation of the gap function as follows

$$\delta g = (\delta \mathbf{x}^J - \delta \mathbf{x}^I - \mathbf{x}^I_{,r} \delta r) \cdot \mathbf{n} + (\mathbf{x}^J - \mathbf{x}^I) \cdot \delta \mathbf{n} \tag{2.7}$$

where $m_{,\alpha}$ denotes $\frac{\partial m}{\partial \alpha}$. From the above two equations

$$\delta g = (\delta \mathbf{x}^J - \delta \mathbf{x}^I - \mathbf{x}^I_{,r} \delta r) \cdot \mathbf{n} + g\mathbf{n} \cdot \delta \mathbf{n} \tag{2.8}$$

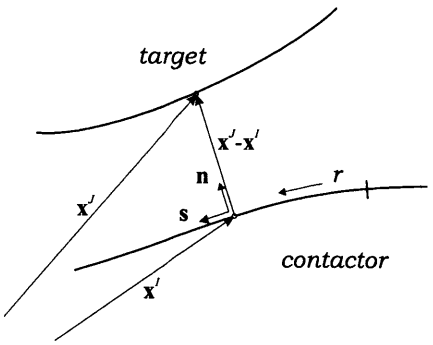

Figure 2-2: Contact kinematics of contact pair.

$$\delta g = (\delta \mathbf{x}^J - \delta \mathbf{x}^I) \cdot \mathbf{n} \tag{2.9}$$

The above expression results due to the fact that $\delta \mathbf{n} \perp \mathbf{n}$ and $\mathbf{x}^I_{,r} \perp \mathbf{n}$. Note that $\mathbf{x}^I_{,r}$ is a tangent vector and we use $\mathbf{a}_r = \mathbf{x}^I_{,r}$. To obtain the unit tangent vector the following relation is used,

$$\mathbf{s} = \frac{\mathbf{a}_r}{\|\mathbf{a}_r\|} \tag{2.10}$$

Substituting the expression for vector of contact tractions from equation (2.3) into the contact integral on the RHS of(2.1) and noting that $\delta \mathbf{x}^i = \delta \mathbf{u}^i$, we can write

$$\int_{S^I} {}^t\mathbf{f}^{JI} \cdot (\delta \mathbf{u}^J - \delta \mathbf{u}^I)\, dS = \int_{S^I} \lambda \delta g \; dS + \int_{S^I} t(\delta \mathbf{u}^J - \delta \mathbf{u}^I) \cdot \mathbf{s} \; dS \tag{2.11}$$

With the expression for contact integral in hand, we now proceed to state the contact conditions at the interface surface. For normal contact, the essential condition to be satisfied is the condition of zero inter-penetration of the contacting bodies. Also the contact tractions are such that there is zero adhesion between the bodies. These conditions can be written as a set of Kuhn-Tucker equations

$$\begin{aligned} g &\geqslant 0 \\ \lambda &\geqslant 0 \\ g\lambda &= 0 \end{aligned} \tag{2.12}$$

According to these complementary equations, the contact traction can only be compressive, and only non-zero when the gap g is zero.

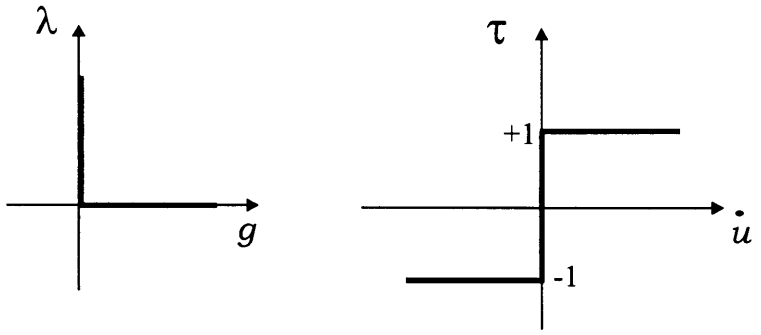

Figure 2-3: Contact conditions.

To take into account the frictional contact conditions, Coulomb's law of friction is assumed to hold point-wise, with μ being the coefficient of friction. Define the non-dimensional variable τ as

$$\tau = \frac{t}{\mu\lambda} \tag{2.13}$$

and the magnitude of the relative tangential velocity corresponding to the unit tangent vector $\mathbf{s}$ at $\mathbf{x}^I$ as

$$\dot{u} = (\dot{\mathbf{u}}^I - \dot{\mathbf{u}}^J) \cdot \mathbf{s} \tag{2.14}$$

Coulomb's law of friction can then be stated in terms of the following conditions

$$\begin{aligned} &|\tau| \leqslant 1 \\ &|\tau| < 1 \quad \Rightarrow \quad \dot{u} = 0 \\ &|\tau| = 1 \quad \Rightarrow \quad \text{sign}(\dot{u}) = \text{sign}(\tau) \end{aligned} \tag{2.15}$$

The solution of the equation of virtual work (2.1) subject to the above normal and tangential contact constraints results in the solution of the contact problem

2.3 The Constraint Equations

We choose to enforce the contact conditions given in equations (2.12) and (2.15) on the principle of virtual work given in equation (2.1) by means of Lagrange multipliers,

which are really the normal contact pressure λ for normal contact and the non-dimensional variable τ for the frictional contact. The constraint function method given in Eterovic and Bathe[21] regularizes the contact constraints and at the same time reduces the inequalities in these constraints to a set of equality constraints which can be solved for using the standard Lagrange multiplier approach. The method is also very attractive since the constraint functions provide information to the algorithm about the changes in contact conditions while still far from convergence. Therefore relatively larger time steps can be used, as compared to the conventional active set strategies used for inequality constraints.

Let w_n be a differentiable function of g and λ, such that the solution of $w_n(g, \lambda) = 0$ satisfies the normal contact conditions in (2.12). Similarly, let w_τ be a function of $\dot{u}$ and τ such that the solution of $w_\tau(\dot{u}, \tau)$ satisfies the tangential contact conditions in (2.15). This reduces the inequality contact constraints, to the following constraint equations

$$w_n(g, \lambda) = 0 \tag{2.16}$$

$$w_\tau(\dot{u}, \tau) = 0 \tag{2.17}$$

Let ϵ_n and ϵ_τ be small, real and positive numbers, and

$$\lambda(g) = \frac{\epsilon_n}{g} \tag{2.18}$$

$$\tau(\dot{u}) = \frac{2}{\pi} \arctan\left(\frac{\dot{u}}{\epsilon_\tau}\right) \tag{2.19}$$

The function w_n is now obtained by generating a surface by passing a line with direction $(1, 1, 1)$ corresponding to (g, λ, w_n) along the curve $\lambda(g)$. Similarly w_τ is obtained, in an implicit form, by passing a line with direction $(1, -1, 1)$ corresponding

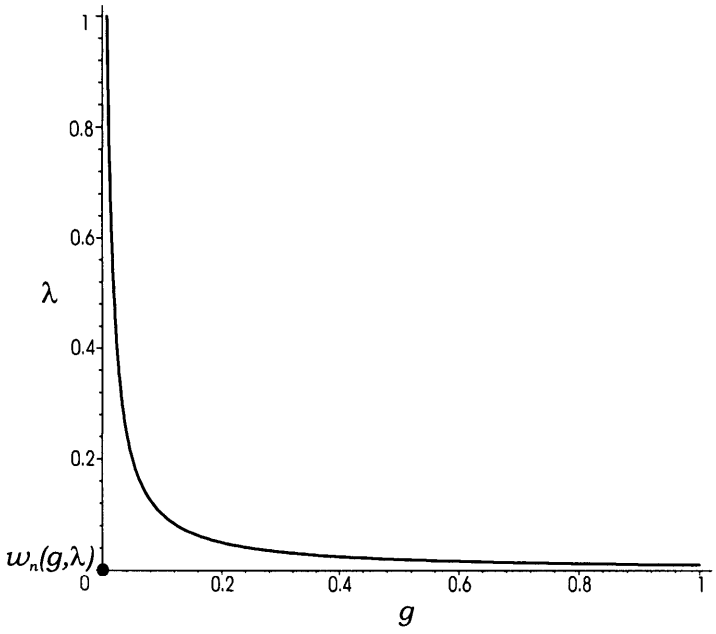

Figure 2-4: Constraint function for normal contact.

to $(\dot{u}, \tau, w_\tau)$ along the curve $\tau(\dot{u})$

$$w_n(g,\lambda) = \frac{g+\lambda}{2} - \sqrt{\left(\frac{g-\lambda}{2}\right)^2 + \epsilon_n} \tag{2.20}$$

$$\tau + w_\tau = \frac{2}{\pi} \arctan\left(\frac{\dot{u} - w_\tau}{\epsilon_\tau}\right) \tag{2.21}$$

Multiplying equations (2.16) and (2.17) and integrating over the whole surface S^1, we obtain the constraint equation

$$\int_{S^I} [\delta\lambda \; w_n(g,\lambda) + \delta\tau \; w_\tau(\dot{u},\tau)] dS^I = 0 \tag{2.22}$$

Now the principle of virtual work can be solved for the two-body contact problem subject to the above constraint equation which provides the information about the contact conditions at the interface. The unknowns in this set of equations are the displacements of the bodies and the unknown contact forces expressed in terms of λ and τ.

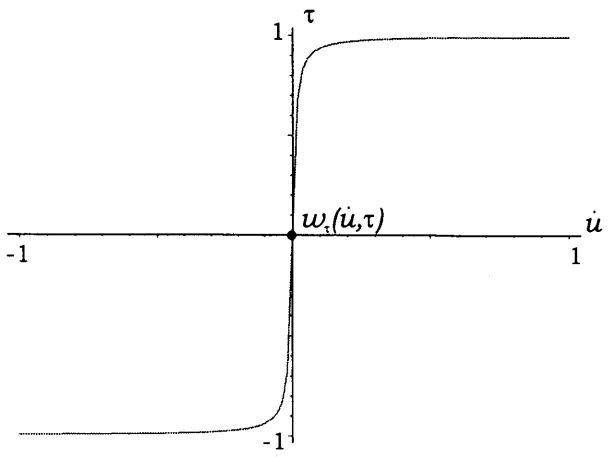

Figure 2-5: Constraint function for tangential contact.

2.4 Linearization of the Contact Integral

The principle of virtual work given in (2.1) and the contact constraint equation (2.22) are nonlinear in displacements and contact tractions. The term representing the internal virtual work in terms of second Piola-Kirchhoff stresses and Green-Lagrange strains can be linearized in the usual way, see for example Bathe [3]. Even if the problem is kinematically linear, the presence of the contact terms still makes the equation nonlinear. For finite element solution of nonlinear problems in computational mechanics, the Newton-Raphson method, which is quadratically convergent, is widely used. But to take full advantage of the quadratic convergence of the method, the nonlinear equations have to be consistently linearized. In the following discussion we focus on the linearization of the normal and tangential contact terms in the contact integral in (2.11) individually to simplify the presentation, and follow a approach similar to that used in Wriggers [41].

2.4.1 Linearization of Normal Contact

The normal contact term in (2.11) at time $t + \Delta t$ can be written using a Taylor expansion about the state at time t, with second order and higher terms dropped, as

$$\int_{S^I} {}^{t+\Delta t}\lambda\delta g \; dS = \int_{S^I} \{{}^t\lambda\delta g \; + \; \frac{\partial({}^t\lambda\delta g)}{\partial({}^t\lambda)}\Delta\lambda \; + \; \frac{\partial({}^t\lambda\delta g)}{\partial(\delta g)}\Delta\delta g\} \; dS \tag{2.23}$$

$$\int_{S^I} {}^{t+\Delta t}\lambda\delta g \; dS = \int_{S^I} \{{}^t\lambda\delta g \; + \; \delta g\Delta\lambda \; + \; {}^t\lambda\Delta\delta g\} \; dS \tag{2.24}$$

where $\Delta\lambda$ is the increment in the normal contact traction and $\Delta\delta g$ is the increment in the variation of the gap function. To evaluate the term $\Delta\delta g$ in terms of incremental displacements $\Delta\mathbf{u}$, we need to go back to the definition of the gap function in (2.5). We cannot compute $\Delta\delta g$ directly from (2.9) since the terms which turned out to be zero in evaluation of δg can still contribute to $\Delta\delta g$. Therefore we start by taking variation of each term in (2.5) using the fact that local variable r parameterizes the contact surface so that $\mathbf{x}^I = \mathbf{x}^I(r)$, and $\delta\mathbf{x}^I = \delta\mathbf{u}^I$, $\delta\mathbf{x}^J = \delta\mathbf{u}^J$

$$\delta\mathbf{u}^J - \delta\mathbf{u}^I - \mathbf{x}^I_{,r}\delta r = \delta g\mathbf{n} + g\delta\mathbf{n} \tag{2.25}$$

If the above equation is multiplied by $\mathbf{n}$ we will get the expression for δg same as (2.9). We employ the idea of directional derivatives directly to above equation and later simplify for $\Delta\delta g$. By taking increments of each term in (2.25), and noting that $\Delta\mathbf{x}^i = \Delta\mathbf{u}^i$ we have

$$-[\delta\mathbf{u}^I_{,r}\Delta r + \Delta\mathbf{u}^I_{,r}\delta r + \mathbf{x}^I_{,rr}\Delta r\delta r + \mathbf{x}^I_{,r}\Delta\delta r] = \Delta\delta g\mathbf{n} + \delta g\Delta\mathbf{n} + \Delta g\delta\mathbf{n} + g\Delta\delta\mathbf{n} \tag{2.26}$$

Taking the dot product of each term in the above equation by $\mathbf{n}$, the expression for $\Delta\delta g$ is obtained

$$\Delta\delta g = -[\delta\mathbf{u}^I_{,r}\Delta r + \Delta\mathbf{u}^I_{,r}\delta r + \mathbf{x}^I_{,rr}\Delta r\delta r]\cdot\mathbf{n} - g\Delta\delta\mathbf{n}\cdot\mathbf{n} \tag{2.27}$$

In this expression for $\Delta\delta g$ the quantities δr,Δr and $\Delta\delta\mathbf{n}$ are still unknown. We first establish an expression for δr as follows. From the fact that $(\mathbf{x}^J - \mathbf{x}^I) \perp \mathbf{a}_r$, where $\mathbf{a}_r = \mathbf{x}^I_{,r}$ is the tangent vector at $\mathbf{x}^I$ we have

$$(\mathbf{x}^J - \mathbf{x}^I) \cdot \mathbf{a}_r = 0 \tag{2.28}$$

Taking the variation on each term in this expression we obtain

$$\delta r = \frac{1}{(l^2 - g\mathbf{n} \cdot \mathbf{x}^I_{,rr})}[(\delta\mathbf{u}^J - \delta\mathbf{u}^I) \cdot \mathbf{x}^I_{,r} + g\mathbf{n} \cdot \delta\mathbf{u}^I_{,r}] \tag{2.29}$$

where

$$l^2 = \|\mathbf{x}^I_{,r}\|^2 \tag{2.30}$$

The structure of the term Δr is the same as above except that variations are replaced by increments,

$$\Delta r = \frac{1}{(l^2 - g\mathbf{n} \cdot \mathbf{x}^I_{,rr})}[(\Delta\mathbf{u}^J - \Delta\mathbf{u}^I) \cdot \mathbf{x}^I_{,r} + g\mathbf{n} \cdot \Delta\mathbf{u}^I_{,r}] \tag{2.31}$$

The term $\Delta\delta\mathbf{n} \cdot \mathbf{n}$ can be evaluated using the fact that $\delta\mathbf{n} \perp \mathbf{n}$,

$$\delta\mathbf{n} \cdot \mathbf{n} = 0 \tag{2.32}$$

$$\Delta(\delta\mathbf{n} \cdot \mathbf{n}) = 0 \tag{2.33}$$

and hence

$$\Delta\delta\mathbf{n} \cdot \mathbf{n} = -\delta\mathbf{n} \cdot \Delta\mathbf{n} \tag{2.34}$$

In order to computer the variation and increment in the normal vector $\mathbf{n}$, use is made of the orthogonality of $\mathbf{n}$ with the tangent vector $\mathbf{a}_r = \mathbf{x}^I_{,r}$

$$\mathbf{n} \cdot \mathbf{a}_r = 0 \tag{2.35}$$

$$\delta\mathbf{n} \cdot \mathbf{a}_r = -\mathbf{n} \cdot \delta\mathbf{a}_r \tag{2.36}$$

$$(\delta\mathbf{n} \cdot \mathbf{a}_r)\mathbf{a}_r = -(\mathbf{n} \cdot \delta\mathbf{a}_r)\mathbf{a}_r \tag{2.37}$$

$$(\delta\mathbf{n} \cdot \mathbf{s})\mathbf{s} = \frac{-1}{l^2}(\mathbf{n} \cdot \delta\mathbf{a}_r)\mathbf{a}_r \tag{2.38}$$

The relation $\mathbf{n} \perp \delta\mathbf{n}$ implies $\delta\mathbf{n} \parallel \mathbf{s}$ which simplifies the above expression to

$$\delta\mathbf{n} = \frac{-1}{l^2}(\mathbf{n} \cdot \delta\mathbf{a}_r)\mathbf{a}_r \tag{2.39}$$

The increment of unit normal $\mathbf{n}$ is computed similarly and has the same structure, increments replacing variations

$$\Delta\mathbf{n} = \frac{-1}{l^2}(\mathbf{n} \cdot \Delta\mathbf{a}_r)\mathbf{a}_r \tag{2.40}$$

In the above expressions for variations and increments for normal vector $\mathbf{n}$

$$\delta\mathbf{a}_r = \delta\mathbf{u}^I_{,r} + \mathbf{x}^I_{,rr}\delta r \quad \text{and} \quad \Delta\mathbf{a}_r = \Delta\mathbf{u}^I_{,r} + \mathbf{x}^I_{,rr}\Delta r \tag{2.41}$$

Substituting expressions from (2.34), (2.39), (2.40) and (2.41) into equation (2.27), the general expression for $\Delta\delta g$ is obtained as follows

$$\begin{aligned}\Delta\delta g = &- [\delta\mathbf{u}^I_{,r}\Delta r + \Delta\mathbf{u}^I_{,r}\delta r + \mathbf{x}^I_{,rr}\Delta r\delta r] \cdot \mathbf{n} \\ &+ \frac{g}{l^2}(\delta\mathbf{u}^I_{,r} + \mathbf{x}^I_{,rr}\delta r) \cdot \mathbf{n} \otimes \mathbf{n}(\Delta\mathbf{u}^I_{,r} + \mathbf{x}^I_{,rr}\Delta r)\end{aligned} \tag{2.42}$$

With the above expression the linearization for the normal contact term in (2.24) is complete.

2.4.2 Linearization of Tangential Contact

In order to treat the tangential contact term in (2.11), consider first the following expression which follows directly from the orthogonality of $\mathbf{x}^J - \mathbf{x}^I = g\mathbf{n}$ to the tangent vector;

$$(\mathbf{x}^J - \mathbf{x}^I) \cdot \mathbf{a}_r = 0 \tag{2.43}$$

Taking variation of each term

$$(\delta\mathbf{u}^J - \delta\mathbf{u}^I - \mathbf{x}^I_{,r}\delta r) \cdot \mathbf{a}_r + (\mathbf{x}^J - \mathbf{x}^I) \cdot \delta\mathbf{a}_r = 0 \tag{2.44}$$

$$l\delta r = (\delta\mathbf{u}^J - \delta\mathbf{u}^I) \cdot \mathbf{s} \tag{2.45}$$

where we used the fact that for tangential contact to be active, the term $\mathbf{x}^J - \mathbf{x}^I = 0$.

The tangential contact term at time $t + \Delta t$ can be written in terms of a Taylor expansion about time t as follows, keeping in mind that $t = \mu\lambda\tau$

$$\begin{aligned}\int_{S^I} {}^{t+\Delta t}[(\delta\mathbf{u}^J - \delta\mathbf{u}^I) \cdot \mathbf{s}\ t]\ dS = \int_{S^I} \Big\{ & {}^t[(\delta\mathbf{u}^J - \delta\mathbf{u}^I) \cdot \mathbf{s}\ t] \\ & + {}^t t\ \Delta[(\delta\mathbf{u}^J - \delta\mathbf{u}^I) \cdot \mathbf{s}] \\ & + {}^t(\delta\mathbf{u}^J - \delta\mathbf{u}^I) \cdot {}^t\mathbf{s}\ \mu\, {}^t\tau\Delta\lambda \\ & + {}^t(\delta\mathbf{u}^J - \delta\mathbf{u}^I) \cdot {}^t\mathbf{s}\ \mu\, {}^t\lambda\Delta\tau \Big\}\ dS\end{aligned} \tag{2.46}$$

The first term on RHS is easy to compute since all the terms depend on the known configuration and the current contact tractions which are assumed to be known. The third and fourth terms on RHS are also trivial to compute once the problem has been discretized and suitable interpolation for contact variables is chosen. It is the second term which needs to be evaluated carefully to obtain a consistent tangent stiffness. Considering equation (2.45) and taking increments

$$\Delta(l\delta r) = \Delta[(\delta\mathbf{u}^J - \delta\mathbf{u}^I) \cdot \mathbf{s}] \tag{2.47}$$

$$l\Delta\delta r + \Delta l\delta r = \Delta[(\delta\mathbf{u}^J - \delta\mathbf{u}^I) \cdot \mathbf{s}] \tag{2.48}$$

Comparing the above equation with (2.46), it is clear that once expressions for $\Delta\delta r$ and $\Delta l\delta r$ are evaluated, the linearization of the tangential contact term is complete. In order to find $\Delta\delta r$, consider once again equation (2.26)

$$-[\delta\mathbf{u}^I_{,r}\Delta r + \Delta\mathbf{u}^I_{,r}\delta r + \mathbf{x}^I_{,rr}\Delta r\delta r + \mathbf{x}^I_{,r}\Delta\delta r] = \Delta\delta g\mathbf{n} + \delta g\Delta\mathbf{n} + \Delta g\delta\mathbf{n} + g\Delta\delta\mathbf{n} \quad (2.49)$$

Taking the dot product of each term in this equation with the tangent vector $\mathbf{a}_r$ and rearranging the terms, the following expression is obtained,

$$\begin{aligned} -l^2\Delta\delta r = {} & (\delta g\Delta\mathbf{n} + \Delta g\delta\mathbf{n} + g\Delta\delta\mathbf{n})\cdot\mathbf{a}_r \\ & + (\delta\mathbf{u}^I_{,r}\Delta r + \Delta\mathbf{u}^I_{,r}\delta r + \mathbf{x}^I_{,rr}\Delta r\delta r)\cdot\mathbf{a}_r \end{aligned} \quad (2.50)$$

In order to simplify the third term on the RHS of the above equation consider the orthogonality condition

$$\mathbf{n}\cdot\mathbf{a}_r = 0 \quad (2.51)$$

$$\delta(\mathbf{n}\cdot\mathbf{a}_r) = \delta\mathbf{n}\cdot\mathbf{a}_r + \mathbf{n}\cdot\delta\mathbf{a}_r = 0 \quad (2.52)$$

$$\Delta\delta(\mathbf{n}\cdot\mathbf{a}_r) = \Delta\delta\mathbf{n}\cdot\mathbf{a}_r + \delta\mathbf{n}\cdot\Delta\mathbf{a}_r + \Delta\mathbf{n}\cdot\delta\mathbf{a}_r + \mathbf{n}\cdot\Delta\delta\mathbf{a}_r = 0 \quad (2.53)$$

$$\Delta\delta\mathbf{n}\cdot\mathbf{a}_r = -(\delta\mathbf{n}\cdot\Delta\mathbf{a}_r + \Delta\mathbf{n}\cdot\delta\mathbf{a}_r + \mathbf{n}\cdot\Delta\delta\mathbf{a}_r) \quad (2.54)$$

where

$$\begin{aligned} \Delta\delta\mathbf{a}_r &= \Delta[\delta\mathbf{u}^I_{,r} + \mathbf{x}^I_{,rr}\delta r] \\ &= \delta\mathbf{u}^I_{,rr}\Delta r + \Delta\mathbf{u}^I_{,rr}\delta r + \mathbf{x}^I_{,rrr}\Delta r\delta r + \mathbf{x}^I_{,rr}\Delta\delta r \end{aligned} \quad (2.55)$$

The first three terms on the RHS of (2.50) can now be written as the following

expression making use of the relation for $\Delta\delta\mathbf{n}\cdot\mathbf{a}_r$ from above equations,

$$
\begin{aligned}
&(\delta g\Delta\mathbf{n}+\Delta g\delta\mathbf{n}+g\Delta\delta\mathbf{n})\cdot\mathbf{a}_r\\
&=(\delta g\Delta\mathbf{n}+\Delta g\delta\mathbf{n})\cdot\mathbf{a}_r-g(\delta\mathbf{n}\cdot\Delta\mathbf{a}_r+\Delta\mathbf{n}\cdot\delta\mathbf{a}_r)-g\mathbf{n}\cdot\Delta\delta\mathbf{a}_r\\
&=\delta g\Delta\mathbf{n}\cdot\mathbf{a}_r+\Delta g\delta\mathbf{n}\cdot\mathbf{a}_r-g\delta\mathbf{n}\cdot\Delta\mathbf{a}_r-g\Delta\mathbf{n}\cdot\delta\mathbf{a}_r-g\mathbf{n}\cdot\Delta\delta\mathbf{a}_r\\
&=-\delta g\mathbf{n}\cdot\Delta\mathbf{a}_r-\Delta g\mathbf{n}\cdot\delta\mathbf{a}_r-g\delta\mathbf{n}\cdot\Delta\mathbf{a}_r-g\Delta\mathbf{n}\cdot\delta\mathbf{a}_r-g\mathbf{n}\cdot\Delta\delta\mathbf{a}_r\\
&=-[\delta(g\mathbf{n})\cdot\Delta\mathbf{a}_r+\Delta(g\mathbf{n})\cdot\delta\mathbf{a}_r]-g\mathbf{n}\cdot\Delta\delta\mathbf{a}_r\\
&=-[\delta(\mathbf{x}^J-\mathbf{x}^I)\cdot\Delta\mathbf{a}_r+\Delta(\mathbf{x}^J-\mathbf{x}^I)\cdot\delta\mathbf{a}_r]-g\mathbf{n}\cdot\Delta\delta\mathbf{a}_r\\
&=-(\delta\mathbf{u}^J-\delta\mathbf{u}^I)\cdot\Delta\mathbf{a}_r-(\Delta\mathbf{u}^J-\Delta\mathbf{u}^I)\cdot\delta\mathbf{a}_r+\mathbf{x}^I_{,r}\delta r\cdot\Delta\mathbf{a}_r+\mathbf{x}^I_{,r}\Delta r\cdot\delta\mathbf{a}_r-g\mathbf{n}\cdot\Delta\delta\mathbf{a}_r
\end{aligned}
\tag{2.56}
$$

With the above equation substituted in equation (2.50), and some rearrangement of like terms, the following expression for $\Delta\delta r$ is obtained

$$
\begin{aligned}
\Delta\delta r=&\Big[(\delta\mathbf{u}^J-\delta\mathbf{u}^I)\cdot\Delta\mathbf{a}_r+(\Delta\mathbf{u}^J-\Delta\mathbf{u}^I)\cdot\delta\mathbf{a}_r\\
&-\mathbf{a}_r\cdot(\delta r\Delta\mathbf{u}^I_{,r}+\delta\mathbf{u}^I_{,r}\Delta r)\\
&-(\mathbf{a}_r\cdot\mathbf{x}^I_{,rr}-g\mathbf{n}\cdot\mathbf{x}^I_{,rrr})\delta r\Delta r\\
&+g\mathbf{n}\cdot(\delta\mathbf{u}^I_{,rr}\Delta r+\delta r\Delta\mathbf{u}^I_{,rr})\\
&-\delta r\mathbf{a}_r\cdot(\Delta\mathbf{u}^I_{,r}+\mathbf{x}^I_{,rr}\Delta r)-(\delta\mathbf{u}^I_{,r}+\mathbf{x}^I_{,rr}\delta r)\cdot\mathbf{a}_r\Delta r\Big]\cdot\\
&\frac{1}{(l^2-g\mathbf{n}\cdot\mathbf{x}^I_{,rr})}
\end{aligned}
\tag{2.57}
$$

In this expression δr and Δr have to be substituted by expressions in equations (2.29) and (2.31). This results in an equation which, although very complicated, is completely linear in terms of the increments in displacements, $\Delta\mathbf{u}$. It is interesting to note that the above expression is symmetric with respect to $\delta\mathbf{u}$ and $\Delta\mathbf{u}$, and hence results in a symmetric contribution to the tangent stiffness matrix.

To evaluate the expression for $\Delta l\delta r$, recall that

$$
l^2=\mathbf{a}_r\cdot\mathbf{a}_r \tag{2.58}
$$

Taking increments on both sides,

$$\Delta l = \frac{1}{l}(\mathbf{a}_r \cdot \Delta \mathbf{a}_r) \tag{2.59}$$

the required expression is obtained

$$\Delta l \delta r = \frac{\delta r}{l}(\mathbf{a}_r \cdot \Delta \mathbf{a}_r) \tag{2.60}$$

It is instructive to note that this expression is non-symmetric in the variations and increments of the unknown displacements of the contacting nodes, and will result in a non-symmetric contribution to the tangent stiffness matrix.

2.5 Linearization of the Constraint Equations

The constraint equations given in the last section can be linearized similarly to obtain expressions which are linear in incremental displacements and incremental contact tractions. Writing the constraint equation (2.22) at time $t+\Delta t$ as a Taylor expansion about time t with only first order terms, we obtain

$$\begin{aligned}\int_{S^I} \Big[& \delta\lambda \{ {}^t w_n + \frac{\partial w_n}{\partial g}\Delta g + \frac{\partial w_n}{\partial \lambda}\Delta\lambda \} \\ & + \delta\tau \{ {}^t w_\tau + \frac{\partial w_\tau}{\partial \dot{u}}\Delta\dot{u} + \frac{\partial w_\tau}{\partial \tau}\Delta\tau \} \Big] dS^I = 0\end{aligned} \tag{2.61}$$

In this linearized equation all the terms can be computed with relative ease. Δg is computed similar to δg as in (2.9),

$$\Delta g = (\Delta \mathbf{u}^J - \Delta \mathbf{u}^I) \cdot \mathbf{n} \tag{2.62}$$

The new term in the linearization of the constraint equation is the increment in the relative velocity $\Delta\dot{u}$ which needs to expressed in terms of incremental displacements $\Delta\mathbf{x}$. For this a numerical approximation to velocities need to be made: here we make

use of a backward difference approximation,

$$\dot{\mathbf{u}} = \frac{{}^{t+\Delta t}\mathbf{x} - {}^{t}\mathbf{x}}{\Delta t} \tag{2.63}$$

With this approximation made for velocities, the increment in relative velocity is computed easily in terms of incremental displacements as

$$\begin{aligned} \Delta\dot{u} &= \Delta[(\dot{\mathbf{u}}^I - \dot{\mathbf{u}}^J) \cdot \mathbf{s}] \\ &= \frac{-1}{\Delta t}[\Delta\mathbf{u}^J - \Delta\mathbf{u}^I - \mathbf{x}^I_{,r}\Delta r] \cdot \mathbf{s} - (\dot{\mathbf{x}}^J - \dot{\mathbf{x}}^I) \cdot \Delta\mathbf{s} \end{aligned} \tag{2.64}$$

where

$$\Delta\mathbf{s} = \frac{1}{l}[\Delta\mathbf{u}^I_{,r} + \mathbf{x}^I_{,rr}\Delta r] - \frac{1}{l^2}\,\mathbf{a}_r\Delta l \tag{2.65}$$

and Δr as given in equation (2.31).

Chapter 3

A Consistent Segment Algorithm (CSA)

3.1 Motivation

Having stated the continuum mechanics equations in the previous chapter, the next step in the numerical solution of contact problems is to discretize the continuum and the contact surface variables. Finite element discretization is almost universally employed for solution of problems in solid mechanics, and it is not the goal of this thesis to present a detailed account of the method. Refer to Bathe [3], Strang and Fix [38] or Ciarlet [16] for a detailed treatment of the topic.

Numerical solution of contact problems, however, is a different story. There are various approaches that have been employed to date. These approaches can be broadly categorized in three classes : node to node, node to segment, and segment to segment approaches. A segment algorithm which is stable and consistent with the finite element discretization of the continuum, was proposed and implemented for small displacement analysis in El-Abbasi and Bathe[18]. In this chapter we present the algorithm for general, large displacement analysis of contacting bodies. The Lagrange multiplier approach is employed, using the constraint function method.

3.2 Finite Element Discretization

Once a finite element discretization for the continuum is chosen, the discretization that follows for the contact surfaces is kept to be consistent with that of the continuum. This is one of the key ingredients of the proposed contact algorithm, and with careful treatment, enables a consistent transfer of contact traction to each of the contacting surfaces irrespective of the choice of contactor and target surfaces.

The geometry of the contactor surface, discretized by p-node segments is interpolated as

$$\mathbf{x}^I = \sum_{i=1}^{p} h_{c_i} \mathbf{x}_i^I \tag{3.1}$$

where h_{c_i} and $\mathbf{x}_i^I$ are the interpolation function and the position vector for the node i, and $h_{c_i} = h_{c_i}(r)$, $r \in [-1, +1]$ being the local variable parameterizing a given contactor segment. The incremental displacements of points on the contactor surface are interpolated to the same order (isoparametric discretization), using the same shape functions,

$$\Delta\mathbf{u}^I = \sum_{i=1}^{p} h_{c_i} \Delta\mathbf{u}_i^I \tag{3.2}$$

Similarly for, target surface, discretized by q-node segments,

$$\mathbf{x}^J = \sum_{j=1}^{q} h_{t_j} \mathbf{x}_j^J \tag{3.3}$$

$$\Delta\mathbf{u}^J = \sum_{j=1}^{q} h_{t_j} \Delta\mathbf{u}_j^J \tag{3.4}$$

where $h_{t_j} = h_{t_j}(r^*)$, r^* being the local variable parameterizing the target surface.

Let $\Delta\hat{\mathbf{u}}$ be the vector of length $2(p+q)$ containing incremental node displacements for both contactor segment and target segment nodes,

$$\Delta\hat{\mathbf{u}}^T = \left[\begin{array}{cccccc:cccccc} \Delta u_x^1 & \Delta u_y^1 & \dots & \Delta u_x^p & \Delta u_y^p & \vdots & \Delta u_x^1 & \Delta u_y^1 & \dots & \Delta u_x^q & \Delta u_y^q \end{array} \right] \tag{3.5}$$

where the first $2p$ entries correspond to the contactor segment nodes, and the last $2q$

entries to target segment nodes. Similarly for variations of nodal positions,

$$\delta\hat{\mathbf{u}}^T = \left[\begin{array}{cccccc|cccccc} \delta u_x^1 & \delta u_y^1 & \dots & \delta u_x^p & \delta u_y^p & \vdots & \delta u_x^1 & \delta u_y^1 & \dots & \delta u_x^q & \delta u_y^q \end{array} \right] \tag{3.6}$$

We can now express $\Delta\mathbf{u}^J - \Delta\mathbf{u}^I$ in terms of interpolation functions as

$$\Delta\mathbf{u}^J - \Delta\mathbf{u}^I = \mathbf{H}\,\Delta\hat{\mathbf{u}} \tag{3.7}$$

where

$$\mathbf{H} = \left[\begin{array}{cccccc|cccccc} -h_{c_1} & 0 & \dots & -h_{c_p} & 0 & \vdots & h_{t_1} & 0 & \dots & h_{t_q} & 0 \\ 0 & -h_{c_1} & \dots & 0 & -h_{c_p} & \vdots & 0 & h_{t_1} & \dots & 0 & h_{t_q} \end{array} \right] \tag{3.8}$$

Similarly $\Delta\mathbf{u}_{,r}$ can be written in terms of the vector of incremental nodal displacements, and interpolation matrix $\mathbf{H}$ of size $(2 \times 2(p+q))$ as,

$$\Delta\mathbf{u}_{,r}^I = \mathbf{H}_{,r}\,\Delta\hat{\mathbf{u}} \tag{3.9}$$

with

$$\mathbf{H}_{,r} = \left[\begin{array}{cccccc|ccc} h_{c_1,r} & 0 & \dots & h_{c_p,r} & 0 & \vdots & 0 & \dots & 0 \\ 0 & h_{c_1,r} & \dots & 0 & h_{c_p,r} & \vdots & 0 & \dots & 0 \end{array} \right] \tag{3.10}$$

The last $2q$ columns of the matrix $\mathbf{H}_{,r}$ are zero since these correspond to the target segment nodes, the interpolation functions h_{t_j} of which are *not* functions of the local variable r which parameterizes the contactor surface S^I. Similarly, $\Delta\mathbf{u}_{,rr}^I = \mathbf{H}_{,rr}\,\Delta\hat{\mathbf{u}}$, which is required in the formulation for 3-node contactor segments, where $\mathbf{H}_{,rr}$ is a matrix holding second derivatives of contactor surface interpolation functions.

The variations in displacements are chosen from the same finite dimensional subspace of admissible functions, giving the following equations

$$\delta\mathbf{u}^J - \delta\mathbf{u}^I = \mathbf{H}\,\delta\hat{\mathbf{u}} \tag{3.11}$$

and

$$\delta \mathbf{u}^I_{,r} = \mathbf{H}_{,r}\, \delta \hat{\mathbf{u}} \tag{3.12}$$

The contact tractions have to be discretized along the contactor surface as well. As shown in El-Abbasi and Bathe [18] and Bathe and Brezzi [7] We choose the same interpolation order for approximating the contact tractions between nodal values, is the interpolation order chosen for the spatial discretization of the contactor surface. For a given contactor segment with p nodes, the normal contact pressure and tangential contact traction can be written as

$$\lambda = \mathbf{H}_c\, \boldsymbol{\lambda} \tag{3.13}$$

$$\tau = \mathbf{H}_c\, \boldsymbol{\tau} \tag{3.14}$$

where the $1 \times p$ matrix $\mathbf{H}_c$ contains the p interpolation functions h_{c_i}, and $\boldsymbol{\lambda}$ and $\boldsymbol{\tau}$ $p \times 1$ vectors containing the traction values at contactor segment nodes,

$$\mathbf{H}_c = \begin{bmatrix} h_{c_1} & \cdots & h_{c_p} \end{bmatrix} \tag{3.15}$$

$$\boldsymbol{\lambda} = \begin{bmatrix} \lambda_1 & \cdots & \lambda_p \end{bmatrix}; \quad \boldsymbol{\tau} = \begin{bmatrix} \tau_1 & \cdots & \tau_p \end{bmatrix} \tag{3.16}$$

3.3 Consistent Segment Algorithm

With the finite element approximations stated in the previous section, we are in a position to write down the finite element equations of the whole system, in which the incremental nodal displacements of the contacting bodies, and the incremental contact tractions at the contactor nodes are the unknowns to be solved for. The finite element equations are obtained in a standard way by using the finite element approximations in the linearized equations obtained in Chapter 2. The unknowns are the incremental nodal displacements and contact traction variables. This requires the evaluation of integrals over the contactor segment.

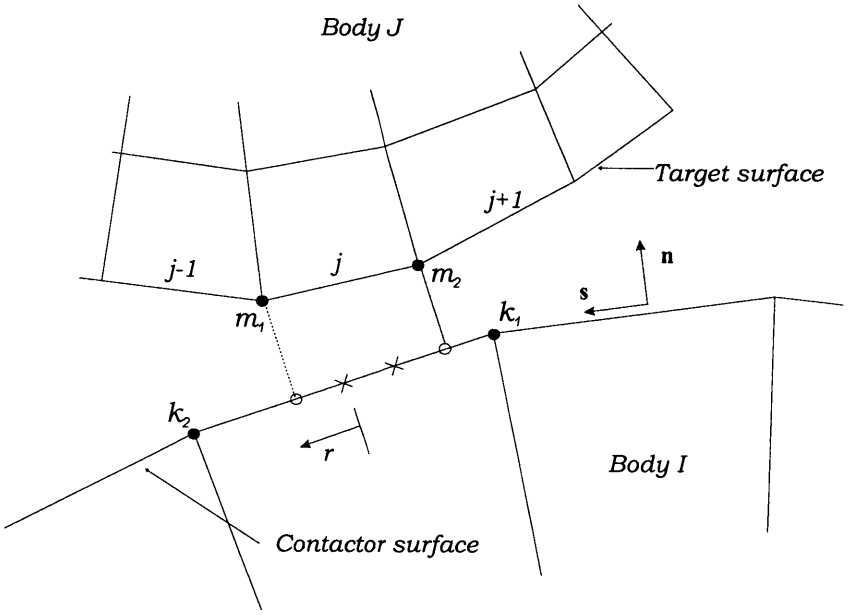

Figure 3-1: End nodes of target segment projected on contactor segment to create sub-segments.

For non-matching contact interfaces, the target and contactor nodes do not match, and the expressions arising in the linearization of the contact integral, Eq. 2.11 are not continuous. It is evident from Figure 3-1, which shows the case of linear elements, that the gap g though continuous will not have a continuous derivative. This poses a problem in the evaluation of integrals. The consistent segment algorithm circumvents this obstacle by further subdividing a contactor segment, into sub-segments, over which the gap and its derivative, both are smooth. Figure 3-1 shows a case of linear contactor and target segments. The nodes m_1 and m_2 of the target segment j project onto the contactor segment with end nodes k_1 and k_2. This creates sub-segments on the contactor segment (in this case three), and all the integrals arising in the calculation of the finite element equations can now be evaluated sub-segment wise, and summed. Note that while evaluating the two sub-segments at each end of the contactor segment, the corresponding target segments are $j+1$ and $j-1$.

The finite element approximations given earlier when used in evaluation of the linearized contact integral obtained in Chapter 2, gives rise to the following finite

element equations for incremental displacements and contact traction variables.

$$\begin{bmatrix} {}^t\mathbf{K}_{uu} + {}^t\mathbf{K}_{uu_c} & {}^t\mathbf{K}_{uc} \\ {}^t\mathbf{K}_{cu} & {}^t\mathbf{K}_{cc} \end{bmatrix} \begin{bmatrix} \Delta\hat{\mathbf{u}} \\ \Delta\hat{\boldsymbol{\lambda}} \end{bmatrix} = \begin{bmatrix} {}^{t+\Delta t}\mathbf{R} - {}^t\mathbf{F} + {}^t\mathbf{R}^c \\ {}^t\mathbf{F}^c \end{bmatrix} \tag{3.17}$$

The first row in this matrix representation is obtained from the principle of virtual work after nonlinear terms have been linearized, and the second equation (row) corresponds to the linearized constraint equation which imposes the contact conditions on the system. The terms in these equations are evaluated using the most recent configuration, obtained during a Newton-Raphson iteration while solving for unknown variables at time $t + \Delta t$. $\Delta\hat{\mathbf{u}}$ and $\Delta\hat{\boldsymbol{\lambda}}$ are the vectors of incremental displacements and contact traction variables. Therefore the above equation actually corresponds to the first iteration to obtain solution at time $t + \Delta t$

${}^{t+\Delta t}\mathbf{R}$ is the vector of externally applied forces at time $t + \Delta t$. ${}^t\mathbf{F}$ is the vector of internal forces calculated using the most recent displacement configuration. ${}^t\mathbf{R}^c$ is the vector storing the nodal forces due to contact tractions. The stiffness matrix contribution ${}^t\mathbf{K}_{uu}$ is the gradient $\frac{\partial {}^t\mathbf{F}}{\partial \mathbf{u}}$. The rest of the matrices and and vectors are obtained using the finite element interpolations given above in the linearized equations of Chapter 2. In the following we give the relations to compute these matrices for the case of 2-node contactor and target segments. In this case all the second derivatives and higher, with respect to the local parameter turn out to be zero within each contactor segment. Let there be total N contactor segments, with each segment having n subsegments once all the target segment end nodes have been projected on the contactor surface. The number n may be different for each contactor segment. Also in all subsequent integrals, we assume unit magnitude thickness.

The vector of nodal forces obtained from contact tractions is then,

$${}^t\mathbf{R}^c = \sum_N \sum_n \int \mathbf{H}^T(\lambda\mathbf{n} + \mu\lambda\tau\mathbf{s})\, det\, \mathbf{J}^{S_c} dr \tag{3.18}$$

The vector ${}^t\mathbf{F}^c$ can be written as

$$ {}^t\mathbf{F}^c = \begin{bmatrix} \mathbf{w}_n \\ \mathbf{w}_t \end{bmatrix} \tag{3.19} $$

where

$$ \mathbf{w}_n = \sum_N \sum_n \int \mathbf{H}_c^T \, w_n \, det\, \mathbf{J}^{S_c} dr \tag{3.20} $$

$$ \mathbf{w}_t = \sum_N \sum_n \int \mathbf{H}_c^T \, w_t \, det\, \mathbf{J}^{S_c} dr \tag{3.21} $$

We can similarly write expressions for ${}^t\mathbf{K}_{uu_c}$, ${}^t\mathbf{K}_{uc}$, ${}^t\mathbf{K}_{cu}$ and ${}^t\mathbf{K}_{cc}$ by using the finite element interpolations in the linearized terms of the contact integral;

$$ \begin{aligned} {}^t\mathbf{K}_{uu_c} = \sum_N \sum_n \int \frac{\lambda}{l^2} (\mathbf{H}_{,r}^T \mathbf{n} \mathbf{x}_{,r}^T \mathbf{H} + \mathbf{H}^T \mathbf{x}_{,r} \mathbf{n}^T \mathbf{H}_{,r} + g \mathbf{H}_{,r}^T \mathbf{n} \mathbf{n}^T \mathbf{H}_{,r}) \, det\, \mathbf{J}^{S_c} dr \\ - \sum_N \sum_n \int \frac{\mu\tau\lambda}{l^2} (\mathbf{H}^T \mathbf{H}_{,r} + \mathbf{H}_{,r}^T \mathbf{H} - \frac{2}{l^2} (\mathbf{H}^T \mathbf{x}_{,r} \mathbf{x}_{,r}^T \mathbf{H}_{,r} \\ + \mathbf{H}_{,r}^T \mathbf{x}_{,r} \mathbf{x}_{,r}^T \mathbf{H} + g \mathbf{H}_{,r}^T \mathbf{n} \mathbf{x}_{,r}^T \mathbf{H}_{,r} + g \mathbf{H}_{,r}^T \mathbf{x}_{,r} \mathbf{n}^T \mathbf{H}_{,r}) \\ + \frac{1}{l^3} (\mathbf{H}^T \mathbf{x}_{,r} + g \mathbf{H}_{,r}^T \mathbf{n}) \mathbf{x}_{,r}^T \mathbf{H}_{,r}) \, det\, \mathbf{J}^{S_c} dr \end{aligned} \tag{3.22} $$

Also

$$ {}^t\mathbf{K}_{uc} = \begin{bmatrix} {}^t\mathbf{K}_{uc}^{\lambda} & {}^t\mathbf{K}_{uc}^{\tau} \end{bmatrix} \tag{3.23} $$

with

$$ {}^t\mathbf{K}_{uc}^{\lambda} = -\sum_N \sum_n \int \mathbf{H}^T (\mathbf{n} + \mu\tau\mathbf{s}) \mathbf{H}_c \, det\, \mathbf{J}^{S_c} dr \tag{3.24} $$

$$ {}^t\mathbf{K}_{uc}^{\tau} = -\sum_N \sum_n \int \mu\lambda \mathbf{H}^T \mathbf{s} \mathbf{H}_c \, det\, \mathbf{J}^{S_c} dr \tag{3.25} $$

The matrix ${}^t\mathbf{K}_{cu}$ is

$$ {}^t\mathbf{K}_{cu} = \begin{bmatrix} {}^t\mathbf{K}_{cu}^{\lambda} \\ {}^t\mathbf{K}_{cu}^{\tau} \end{bmatrix} \tag{3.26} $$

where

$$ {}^{t}\mathbf{K}_{cu}^{\lambda} = -\sum_{N}\sum_{n}\int \frac{\partial w_n}{\partial g}\mathbf{H}_c^T\mathbf{n}^T\mathbf{H}\, det\, \mathbf{J}^{S_c} dr \tag{3.27} $$

$$ \begin{aligned} {}^{t}\mathbf{K}_{cu}^{\tau} = -\sum_{N}\sum_{n}\int \frac{\partial w_t}{\partial \dot{u}}\{&\frac{-1}{\Delta t}\mathbf{H}_c^T\mathbf{s}^T\mathbf{H} + \frac{1}{l\Delta t}\mathbf{H}_c^T(\mathbf{x}_{,r}^T\mathbf{H} + g\mathbf{n}\mathbf{H}_{,r}) \\ &+\mathbf{H}_c^T\mathbf{v}_{rel}^T(\frac{1}{l}\mathbf{H}_{,r} - \frac{1}{l^3}\mathbf{x}_{,r}\mathbf{x}_{,r}^T\mathbf{H}_{,r})\}\, det\, \mathbf{J}^{S_c} dr \end{aligned} \tag{3.28} $$

where $\mathbf{v} = \dot{\mathbf{u}}^I - \dot{\mathbf{u}}^J$ The block diagonal matrix ${}^{t}\mathbf{K}_{cc}$ is

$$ {}^{t}\mathbf{K}_{cc} = \begin{bmatrix} {}^{t}\mathbf{K}_{cc}^{\lambda} & \mathbf{0} \\ \mathbf{0} & {}^{t}\mathbf{K}_{cc}^{\tau} \end{bmatrix} \tag{3.29} $$

where the block diagonals are

$$ {}^{t}\mathbf{K}_{cc}^{\lambda} = -\sum_{N}\sum_{n}\int \frac{\partial w_n}{\partial \lambda}\mathbf{H}_c^T\mathbf{H}_c\, det\, \mathbf{J}^{S_c} dr \tag{3.30} $$

$$ {}^{t}\mathbf{K}_{cc}^{\tau} = -\sum_{N}\sum_{n}\int \frac{\partial w_t}{\partial \tau}\mathbf{H}_c^T\mathbf{H}_c\, det\, \mathbf{J}^{S_c} dr \tag{3.31} $$

All the integrals, in practice can be evaluated using Gauss integration, with Gauss points chosen *inside each sub-segment.* This ensures accurate integration on the piecewise smooth intervals within a contactor segment. This system of finite element equations is non-symmetric due to the coupling matrices ${}^{t}\mathbf{K}_{uc}$ and ${}^{t}\mathbf{K}_{cu}$. The main contribution to this non-symmetry comes from the friction terms. In the absence of friction, one can obtain a symmetric system by dividing the second row of the finite element equation 3.17 by $\frac{\partial w_n}{\partial g}$, but this may result in a very large numerical values in corresponding matrix entries. The reason for this is due to the fact, for a contact surface pair, with valid projection, but relatively large gap values, the derivative $\frac{\partial w_n}{\partial g}$ is close to zero. Division by such a small number may create problems in a general large deformation contact analysis. Since there is non-symmetry present anyway due to friction, it is preferable to keep the equations in the form given above.

3.4 Choice of Contactor and Target Surfaces

Typically, the choice of contactor and target surfaces for a given contact surface pair introduces a numerical bias. In node-to-segment algorithms (single pass), the no-penetration condition is satisfied at the contactor nodes. Therefore better and more accurate results, should be expected when the contactor surface is more finely meshed as compared to the target surface. An illustration of this is made in the numerical examples to follow. In the consistent segment algorithm however, the contact conditions are enforced on the sub-segments formed on the contactor surface by projecting end nodes of target segments. The contact tractions are transferred to the two surfaces in a manner consistent with the order of the underlying continuum finite elements and the contact traction interpolation. Two scenarios can be envisaged in this regard, as shown in Figure 3-2. In the first case, the top surface, which does not extend beyond the lower surface, is chosen as the contactor. A possible normal contact stress distribution is shown. Equal and opposite contact tractions get transferred to the lower surface, which is of course the target. The other situation arises, when the lower surface is chosen as the contactor. In this case, it is possible that the nodes belonging to those contactor segments with no active sub-segments, may end up with normal contact stress values which are non-zero. This can be a result of the fact that continuous contact stresses are assumed withing a contactor segment. These non-zero contact stress values at nodes, which are not in contact actually, are handled easily in the consistent segment framework: while evaluating the contact tractions on the bodies, *the algorithm loops over the active subsegments only*; therefore the shaded part of the contact stress distribution which should have no physical relevance is chopped off automatically (shaded area), resulting in application of equal and opposite contact tractions on the contact surfaces.

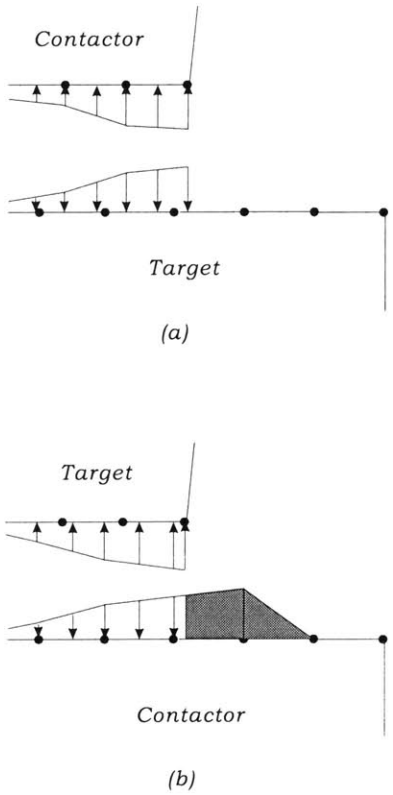

Figure 3-2: Choice of contactor and target surfaces; (a) top surface contactor, (b) bottom surface contactor.

3.5 Numerical Solutions

In this section we present numerical solutions obtained using the consistent segment algorithm presented above. The results produced by the solution algorithm showcase the performance of the algorithm as compared to the more traditionally employed node-to-segment algorithms.

3.5.1 The Patch Test

The patch test is a widely accepted numerical benchmark test for evaluating behavior of nonconforming finite element formulations. In such finite elements, although the requirements of exact inter-element continuity may be violated, for convergence to be guaranteed a given assemblage of elements should be able to represent constant stress states when subjected to appropriate boundary conditions and external loads, see Irons and Razzaque [24] and Bathe [3] . The contact patch test is an extension of the idea, to test if correct stress states can be transferred exactly across the contact interface of a given pair of elastic contacting bodies, discretized by finite elements which otherwise pass the conventional patch test, and subjected to appropriate boundary conditions.

The contact patch test geometry is the same as employed in El-Abbasi and Bathe [18], and is given in Figure 3-3. However, in the present work, the consistent segment formulation is coupled with the constraint function method, and in general makes no prior assumption on the active contact areas. Two identical blocks are vertically stacked with the top block subjected to a uniform pressure distribution of unit magnitude. The geometry of the blocks and the fact that Poisson's ratio $\nu = 0.0$, dictate that the only non zero stress state is the vertical compressive stress of unit magnitude. The contacting surface of the top block, meshed with fewer elements than the lower blocks, is chosen as the contactor.

Figures 3-4 and 3-5 show the results obtained using the node-to-segment (NTS) algorithm (Eterovic [19]) employing 4-node elements along with 2-node linear contact segment on the contactor surface. The plots for vertical displacement fields show

oscillations near the contact interface, with displacement continuity imposed at locations where contactor nodes meet the target surface. This non-uniformity in the displacement field translates into a polluted stress field in the lower block, and hence the patch test is not passed. The consistent segment formulation on the other hand successfully resolves the expected linear vertical displacement field exactly, and correspondingly an exactly constant stress field in both the bodies, as can be seen in Figures 3-6 and 3-7.

Next, the top block is discretized using only one element across the width. With the top block as the contactor, the node-to-segment algorithm completely fails to pick up the correct solution. All the nodes on the target surface are free to penetrate the top block, except at the ends, see Figures 3-8 and 3-9. The consistent segment algorithm when employed with either of the blocks as the contactor, successfully produces the correct solution, see Figures 3-10 and 3-11

Finally 9-node elements for blocks with corresponding 3-node parabolic contact segments on the contact surfaces are used for the same problem but a coarser mesh. The top body is again chosen as the contactor. Figures 3-12 and 3-13 show the results obtained using NTS algorithm. No penetration condition is imposed at the location of contactor nodes, including the middle nodes of the contactor segments. The target nodes are free to penetrate, resulting in a non-uniformly varying displacement field and hence a non-constant stress distribution. The consistent segment algorithm on the other hand produces the exact result both for displacement and stress distribution, Figures 3-14 and 3-15.

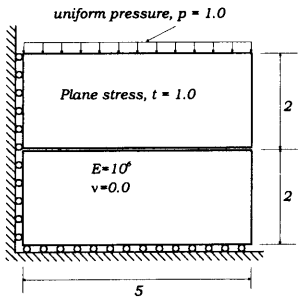

Figure 3-3: The patch test.

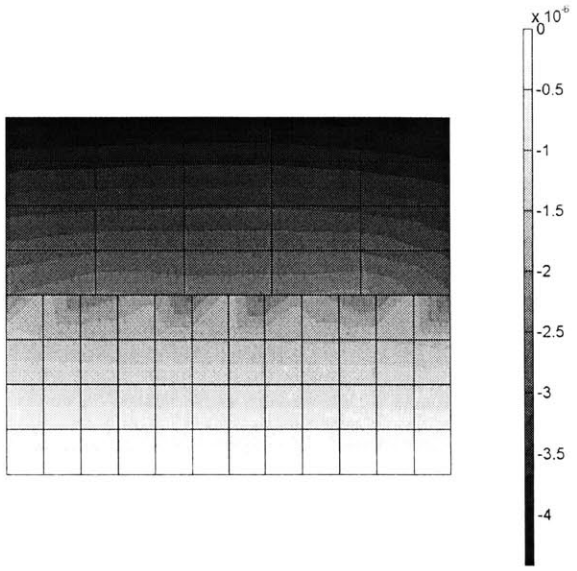

Figure 3-4: The patch test; oscillatory vertical displacement field obtained using the node-to-segment scheme.

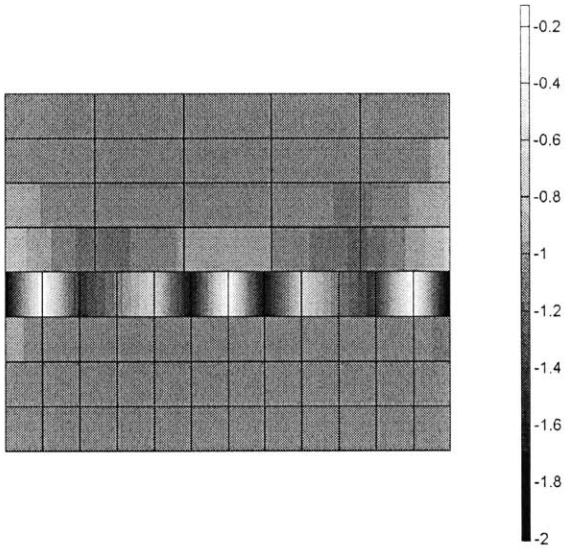

Figure 3-5: The patch test; vertical stress field obtained using the node-to-segment scheme.

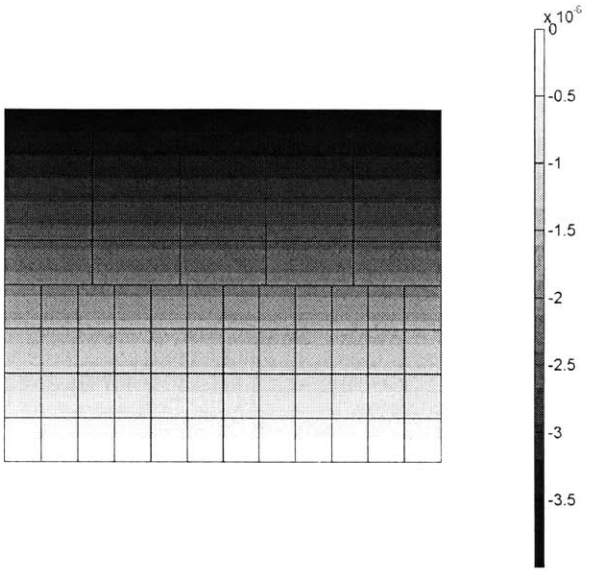

Figure 3-6: The patch test; a uniformly linearly varying vertical displacement field obtained using the consistent segment algorithm.

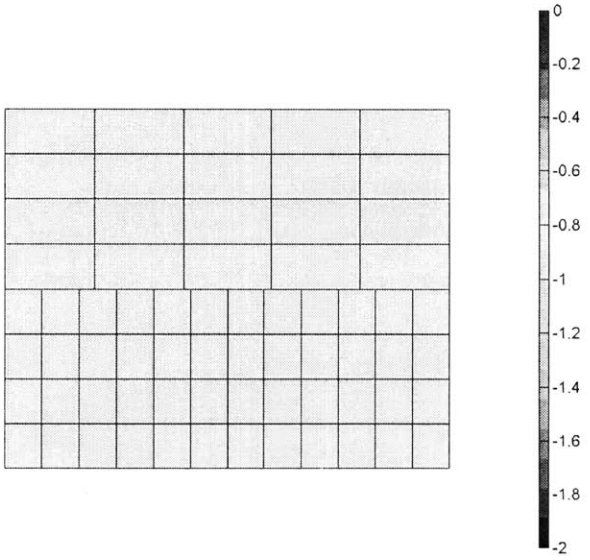

Figure 3-7: The patch test; constant vertical stress field obtained using the consistent segment algorithm.

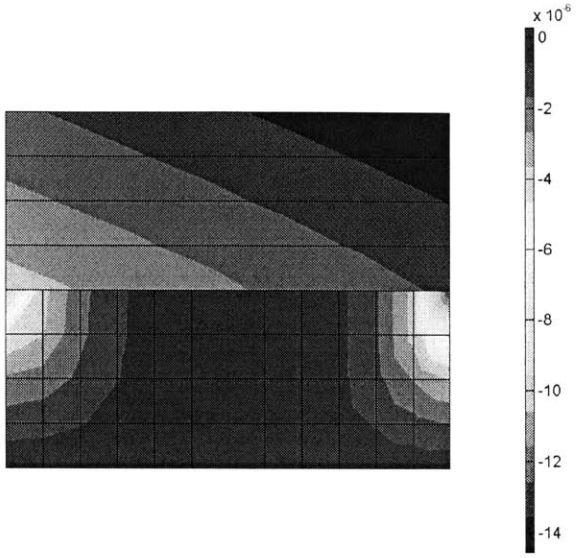

Figure 3-8: The patch test; incorrect displacement field using node-to-segment scheme; top block contactor.

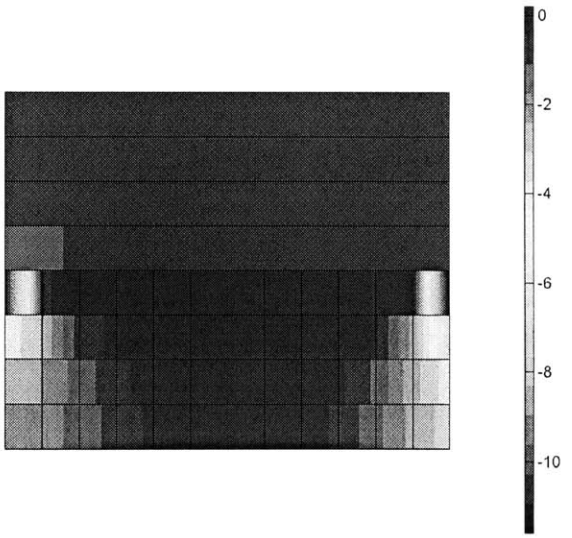

Figure 3-9: The patch test; vertical stress field obtained using the node-to-segment scheme; top block contactor.

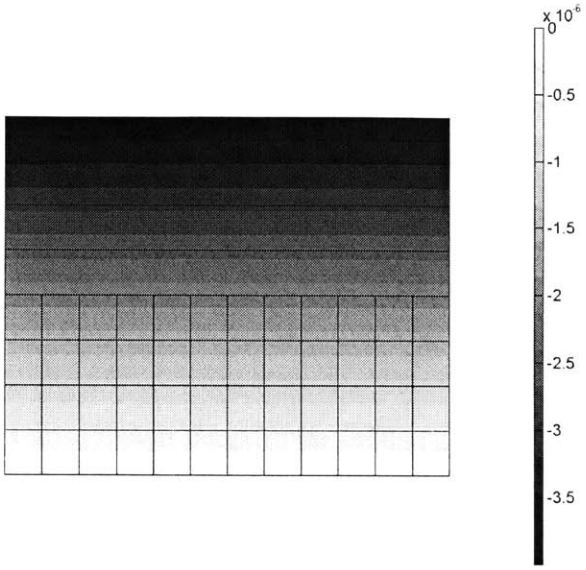

Figure 3-10: The patch test; displacement field using consistent segment scheme; top block contactor.

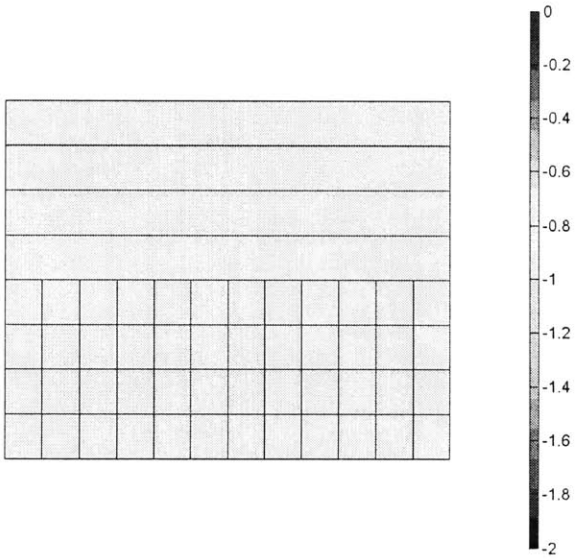

Figure 3-11: The patch test; vertical stress field obtained using the consistent segment scheme; top block contactor.

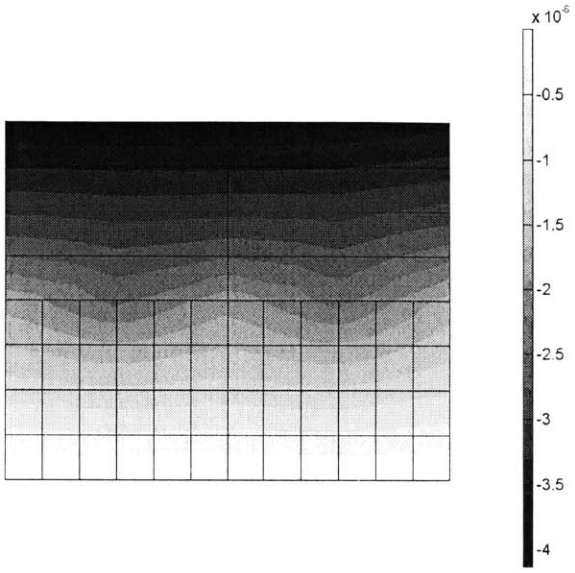

Figure 3-12: The patch test; displacement field using node-to-segment scheme; top block contactor, 9-node elements.

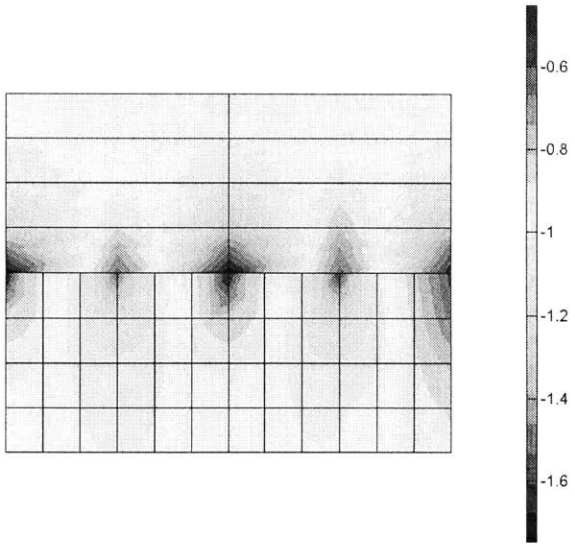

Figure 3-13: The patch test; vertical stress field obtained using the node-to-segment scheme; top block contactor, 9-node elements.

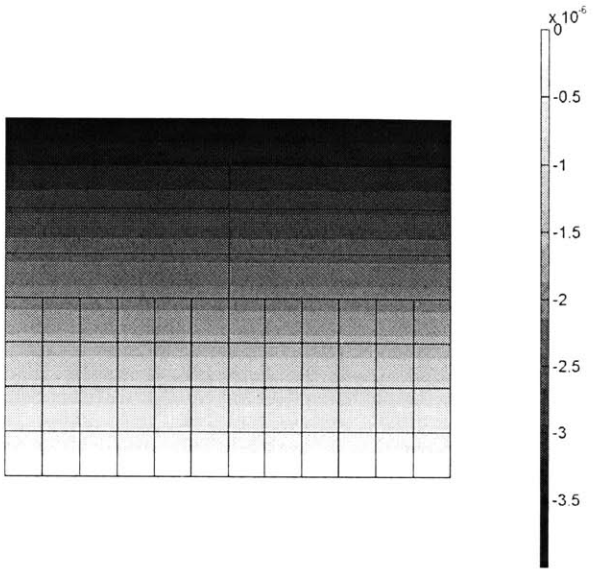

Figure 3-14: The patch test; displacement field using consistent segment scheme; top block contactor, 9-node elements.

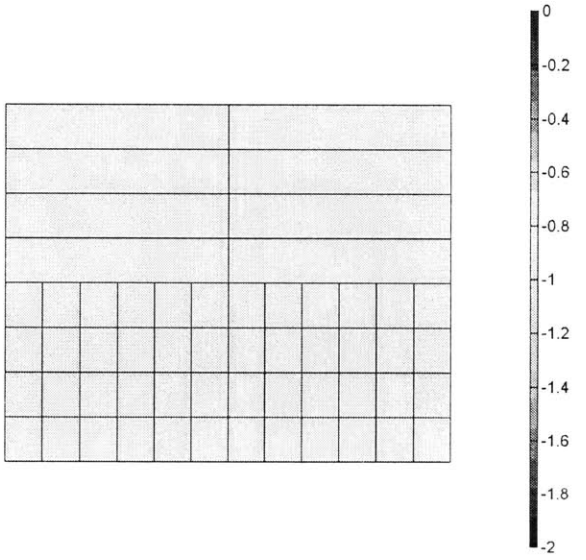

Figure 3-15: The patch test; vertical stress field obtained using the node-to-segment scheme; top block contactor, 9-node elements.

3.5.2 The Punch Problem

The problem consists of an elastic punch pressing against a larger elastic body with the same material properties, under the action of applied pressure. The geometry and the material properties are given in Figure 3-16. Small displacements and small strains are assumed.

The objective is to demonstrate the relative insensitivity of the response obtained using the consistent segment algorithm, with respect to the choice of contactor and target surfaces when non-matching surfaces are used for the bodies. Both blocks are discretized using 3×3 9-node element meshes; thus there are 3-node parabolic contact segments on both bodies, but of different sizes.

The problem is first solved using the top body as the contactor, and then the bottom body as the contactor. The stress distributions for the two cases are shown in Figure 3-17 and Figure 3-18, and it is seen that virtually the same solutions are obtained. However when using the lower body as the contactor, it is important to integrate only over the sub-segments which are formed by the projection of target segments onto the contactor segments.

Next, the problem is solved using the consistent segment algorithm with both blocks discretized by 8×8 9-node element meshes, with the top body as contactor. The problem is also solved using a very fine 40×40 mesh for top block and 100×40 mesh for lower block (such that the meshes are *matching* at the interface) using the NTS algorithm. The contact stress distribution obtained using both algorithms is plotted in Figure 3-19.

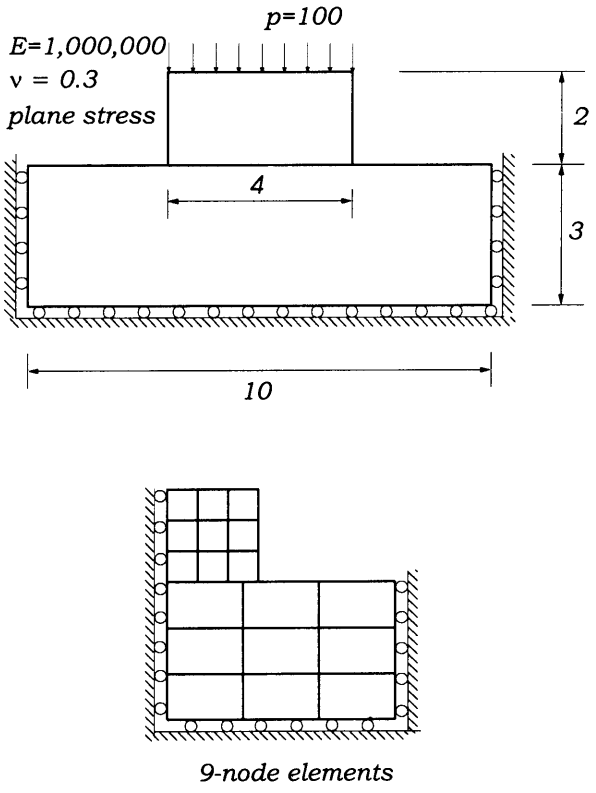

Figure 3-16: The elastic punch problem.

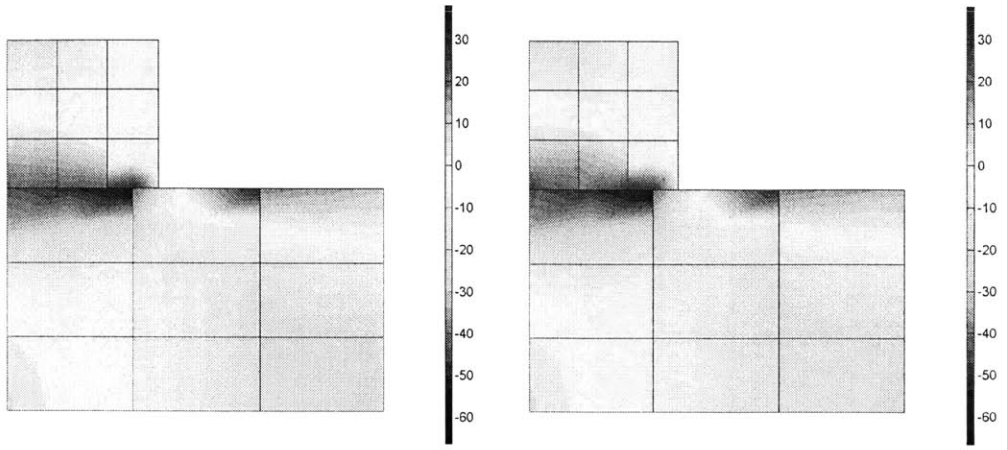

Figure 3-17: The elastic punch; horizontal stress field, using top and lower body as contactor.

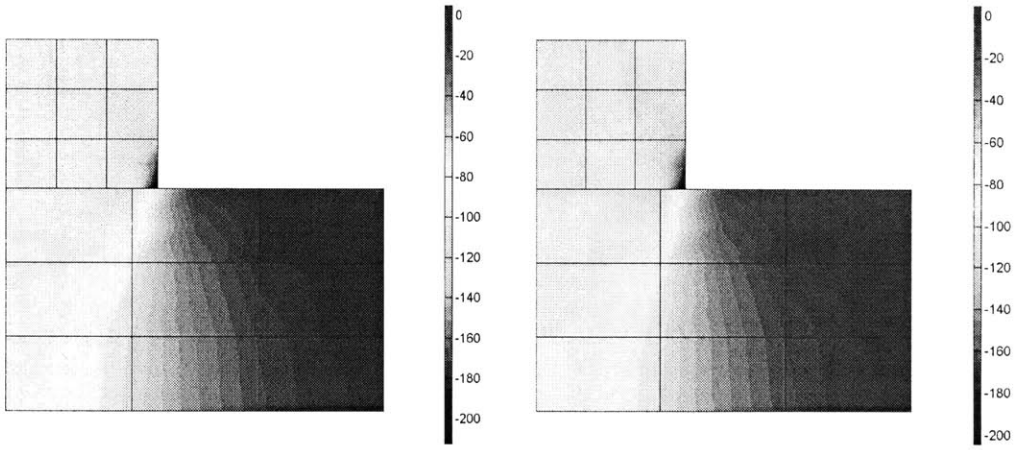

Figure 3-18: The elastic punch; vertical stress field, using top and lower body as contactor.

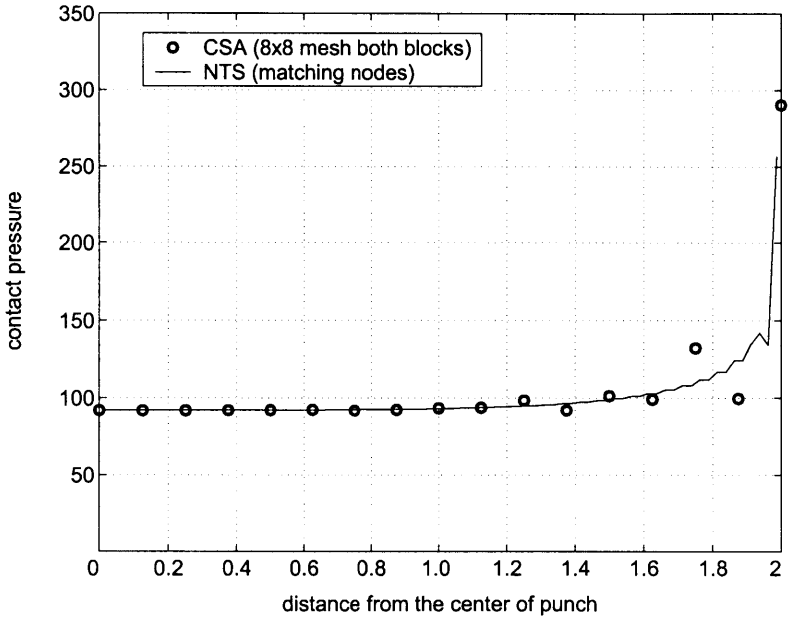

Figure 3-19: The elastic punch problem; contact pressure distribution.

3.5.3 Hertzian Contact

Next we consider the deformation of a long elastic cylinder pressed between two rigid surfaces. Linear elastic material behavior is considered with the material properties given in Figure 3-20 along with the problem geometry. The prescribed displacement. Hertz solution to this problem is taken as the reference solution, see [39].

Both 4 and 9-node elements are employed to solve this problem. Figures 3-21 and 3-22 show the distribution of the stresses in the quarter cylinder considered, using 4-node elements/2-node contact segments. The results obtained using the 9-node elements/3-node contact segments are given in Figures 3-23 and 3-24 are given. A coarser mesh is used to keep the number of degrees of freedom the same as in the previous case. The contact tractions computed for both 4-node and 9-node element analyses are plotted along with the Hertz solution in Figure 3-25.

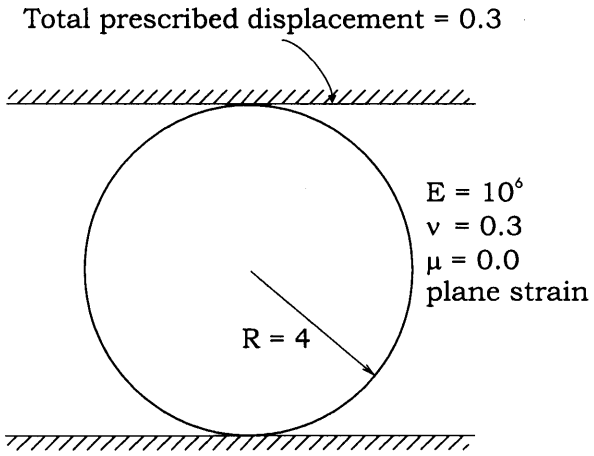

Figure 3-20: Hertzian contact problem.

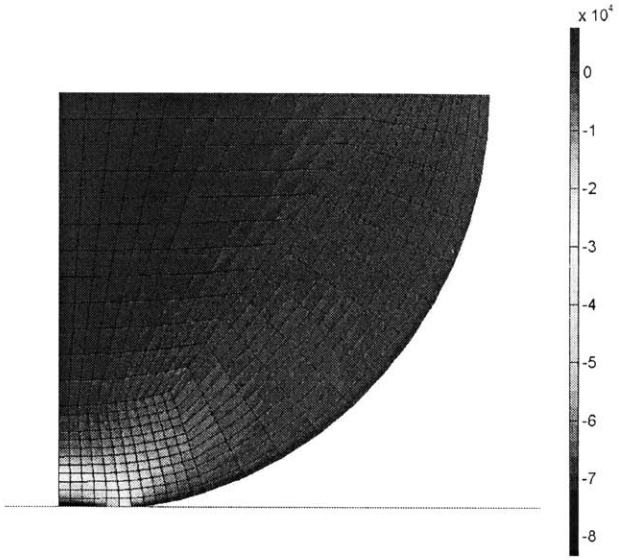

Figure 3-21: Hertzian contact problem; horizontal stress field, 4-node elements.

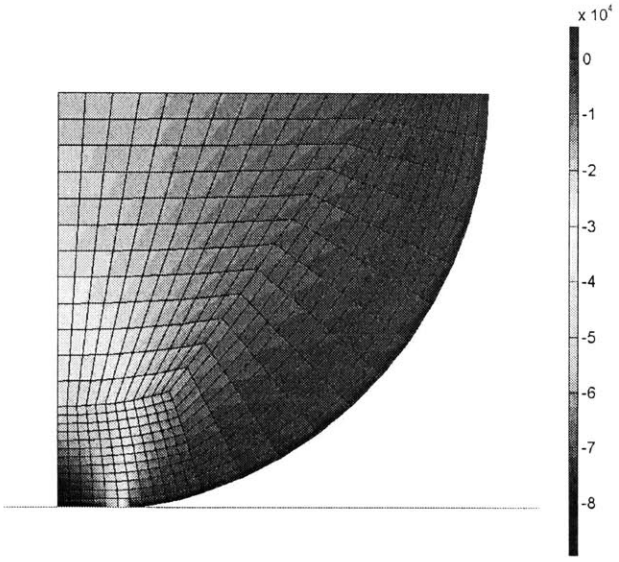

Figure 3-22: Hertzian contact problem; vertical stress field, 4-node elements.

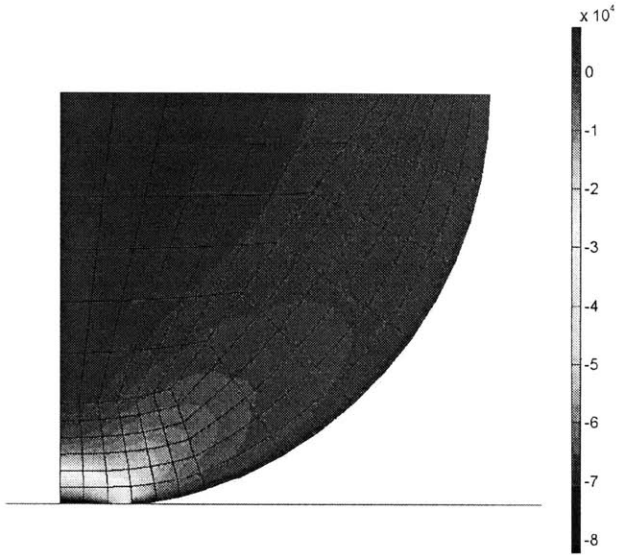

Figure 3-23: Hertzian contact problem; horizontal stress field, 9-node elements.

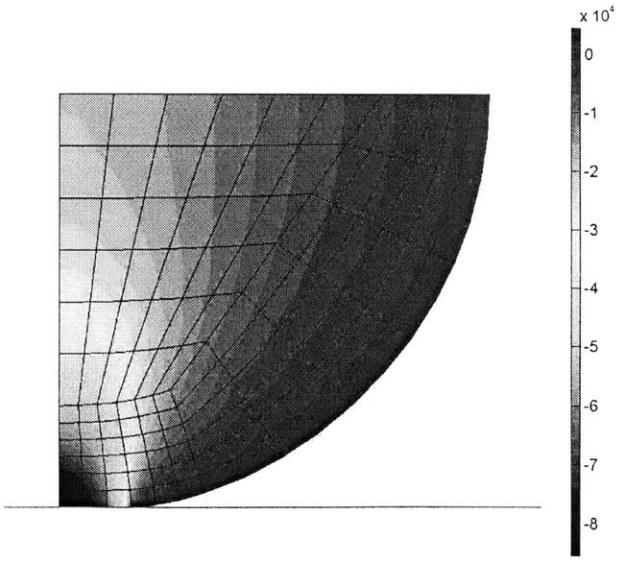

Figure 3-24: Hertzian contact problem; vertical stress field, 9-node elements.

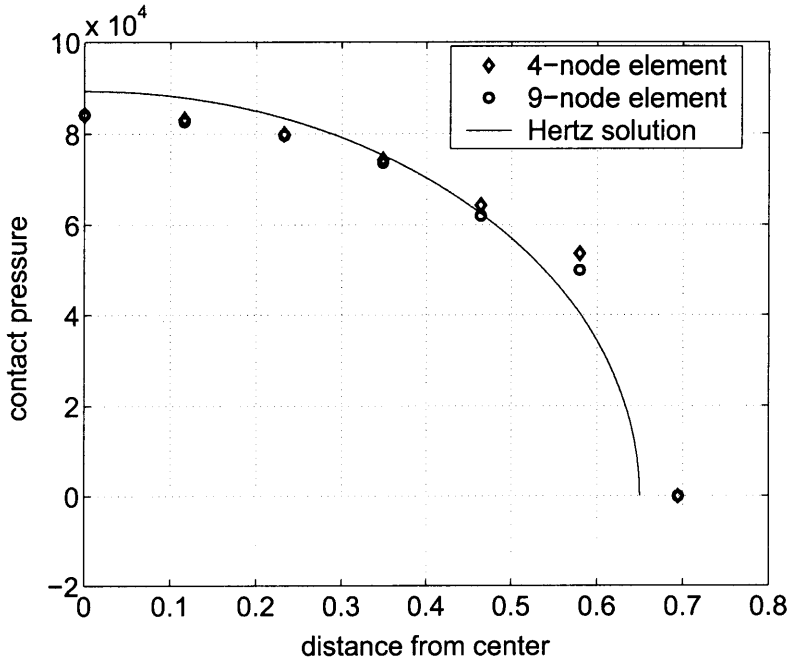

Figure 3-25: Hertzian contact problem; contact pressure distribution.

3.5.4 Sheet in a Converging Channel

To test the performance of the consistent segment algorithm in situations involving frictional contact, the problem of a sheet moving in a converging channel is solved. Linear elastic material model is used for the sheet, in plane stress conditions. The elastic properties are given in Figure 3-26. The converging channel is modeled using rigid surfaces. Due to the symmetry of the problem on the upper half of the sheet is considered, with appropriate boundary conditions applied at the line of symmetry. The problem is first solved assuming frictionless contact, i.e. $\mu = 0.0$. Both 4-node and 9-node elements are employed. For this frictionless case, the normal contact tractions are plotted in Figures 3-27 and 3-28. Exact replication of stress states is achieved when the sheet is pushed back from time $t = 8$ s. onwards.

Next the problem is solved with friction taken into account. Figures 3-29 to 3-32 show the contact tractions obtained at various solution times, for both 4-node and 9-node elements. These tractions are smooth even during the reversal of the frictional tractions. Figures 3-33 and 3-34 show a comparison of results obtained using the consistent segment algorithm and the node-to-segment approach.

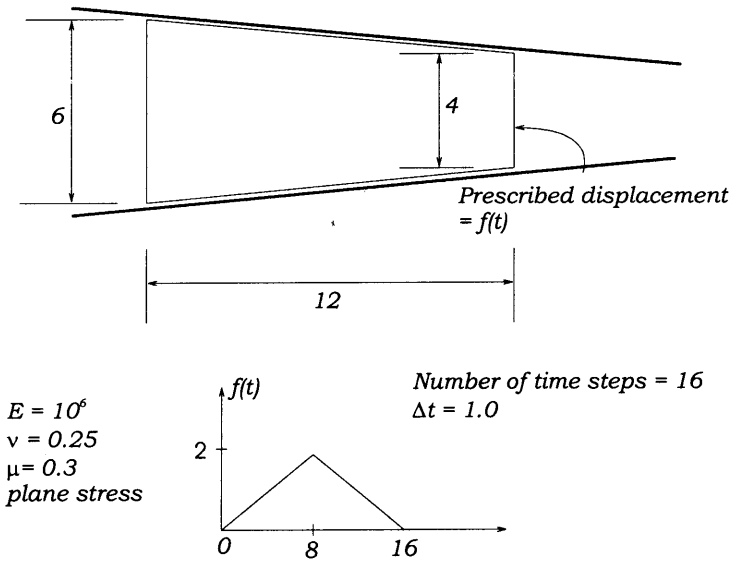

Figure 3-26: Sheet in a converging channel.

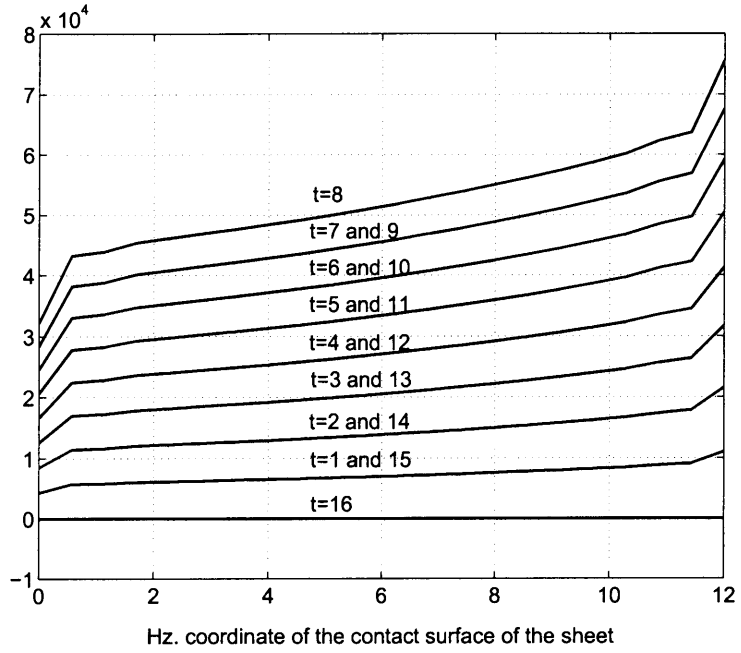

Figure 3-27: Normal traction using 4-node elements; $\mu = 0.0$.

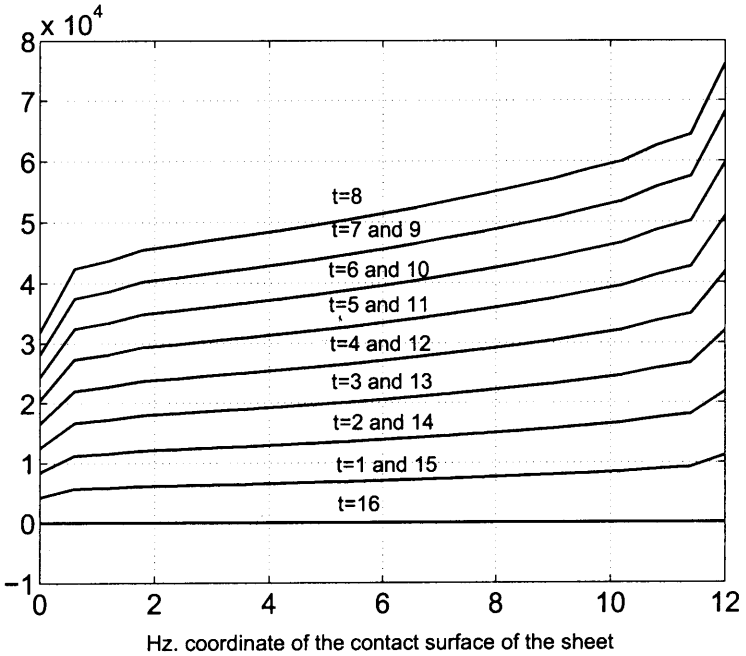

Figure 3-28: Normal traction using 9-node elements; $\mu = 0.0$.

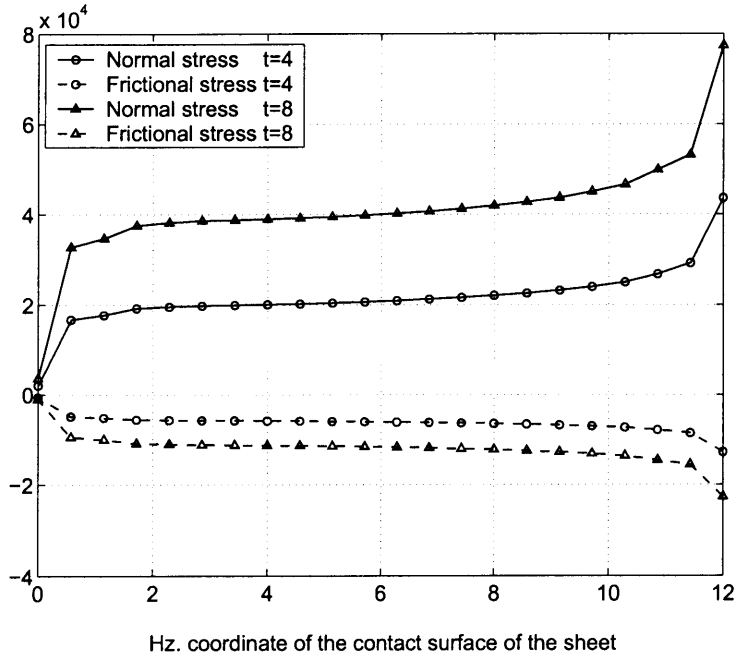

Figure 3-29: Tractions at times $t = 4$ and 8 s.; 4-node elements; $\mu = 0.3$.

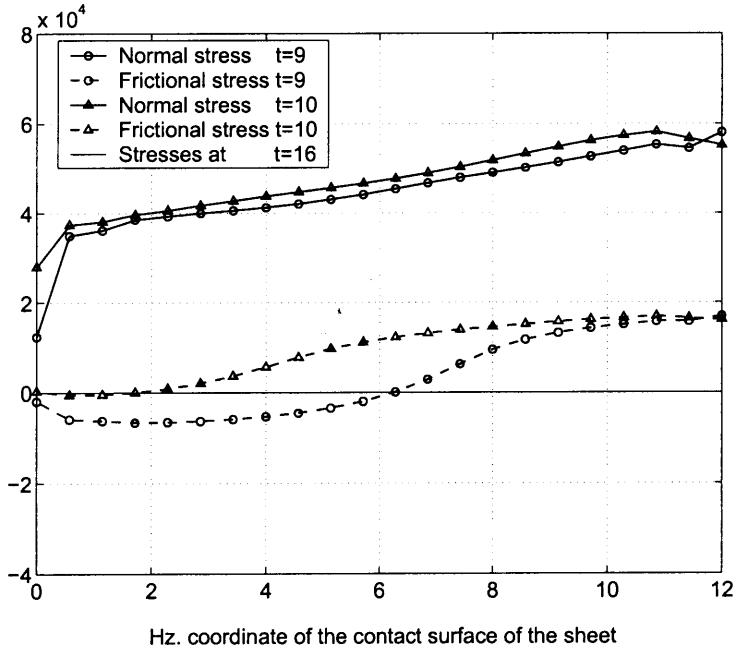

Figure 3-30: Tractions at times $t = 9$, 10 and 16 s.; 4-node elements; $\mu = 0.3$.

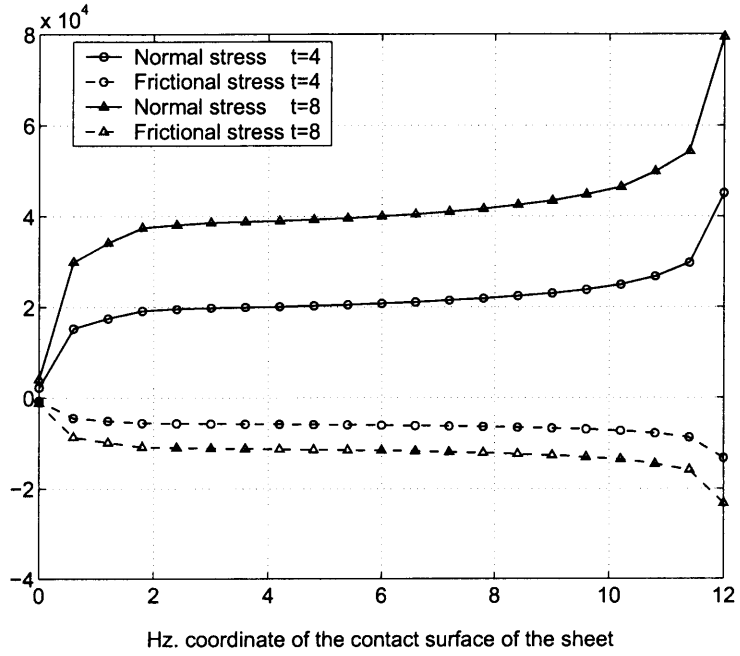

Figure 3-31: Tractions at times $t = 4$ and 8 s.; 9-node elements; $\mu = 0.3$.

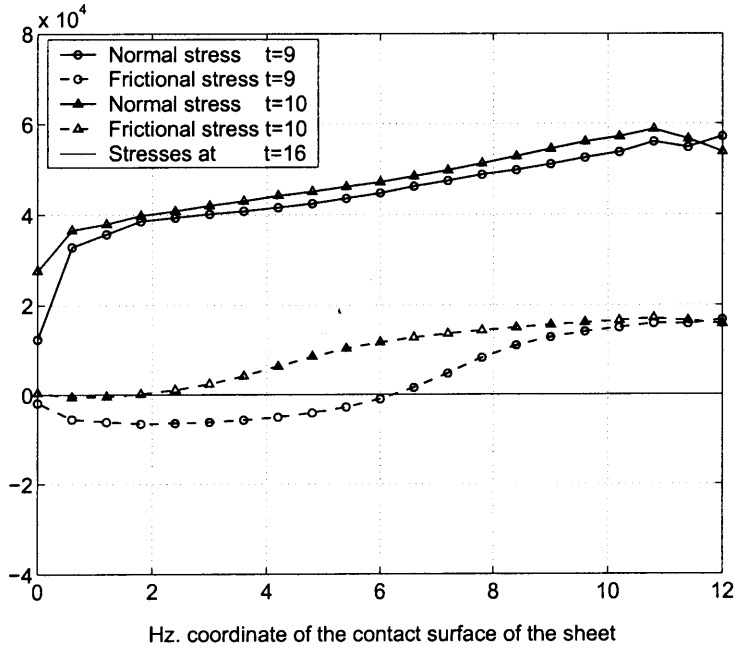

Figure 3-32: Tractions at times $t = 9$, 10 and 16 s.; 9-node elements; $\mu = 0.3$.

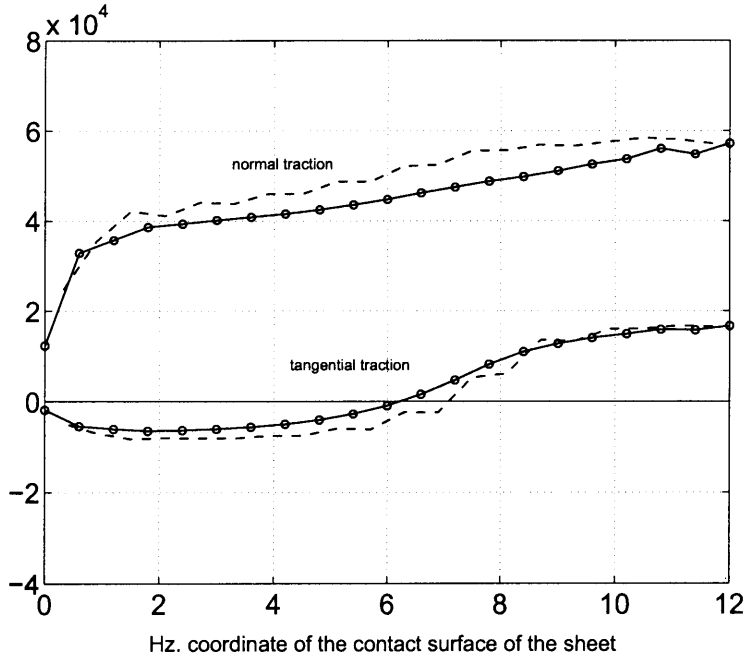

Figure 3-33: Comparison between CSA and NTS; $t = 9$ s.; 9-node elements; $\mu = 0.3$.

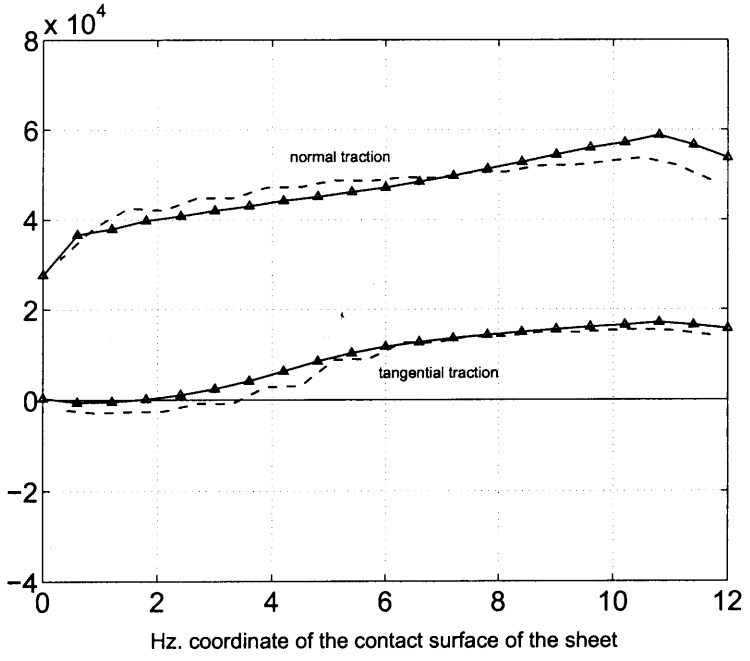

Figure 3-34: Comparison between CSA and NTS; $t = 10$ s.; 9-node elements; $\mu = 0.3$.

Chapter 4

Direct Time Integration: Nonlinear Dynamics

Transient analysis of nonlinear problems in structural and solid mechanics is mainly carried out using direct time integration of the equations of motion. For reliable solutions, an efficient and stable integration algorithm is desirable. Methods that are unconditionally stable in linear analyses appear to be a natural choice for use in nonlinear analyses, but unfortunately may not remain stable for a given time step size. A composite time integration scheme is proposed and tested by solving numerical examples, and found to be effective where the trapezoidal rule fails to produce a stable solution. These examples are indicative of the merits of the composite scheme.

4.1 Motivation

Transient analysis of nonlinear problems in solid and structural mechanics requires effective and robust algorithms to obtain accurate and stable solutions. The semi-discrete equations of equilibrium that are obtained after spatial discretization of the domain of interest can be written in the matrix form

$$\mathbf{M}\ddot{\mathbf{U}} + \mathbf{C}\dot{\mathbf{U}} = \mathbf{R} - \mathbf{F}, \tag{4.1}$$

The first term on the left hand side represents the inertial effects with $\mathbf{M}$ being the mass matrix and $\ddot{\mathbf{U}}$ the acceleration vector. The second term represents velocity dependent viscous damping with $\mathbf{C}$ and $\dot{\mathbf{U}}$ being the damping matrix and velocity vector, respectively. $\mathbf{R}$ is the vector of external loads, and $\mathbf{F}$ the vector of internal nodal forces obtained by integrating stresses over the whole domain, and can be a nonlinear function of displacements, the nonlinearities being either geometric or material, or both.

Direct time integration is a widely used solution technique for solving (4.1), in which equilibrium is satisfied at discrete time points Δt apart. The solution is stepped forward in time by assuming variations of displacements, velocities and accelerations within the time interval Δt. These assumptions on the variation of the response can directly affect the accuracy and stability of the solution algorithm.

Direct integration techniques can be either explicit or implicit. Explicit integration techniques enforce eq. (4.1) at the current time t, and, based on an approximation of the time derivatives, obtain the solution at time $t + \Delta t$. This computation can be relatively inexpensive to carry out for each time step since no solution of linear equations is involved (assuming $\mathbf{M}$, and $\mathbf{C}$ if present, to be a diagonal matrix). Explicit techniques, like the central difference method, however, impose a restriction on the largest time step size that can be employed without losing the stability of the algorithm, and are therefore only conditionally stable. This restriction results in a time step size that can be several orders of magnitude smaller than the step size which would be adequate to accurately resolve the response. However, if the solution contains a significant contribution from high frequency modes, then the time step size required to resolve this high frequency component of the response accurately may well be of the same order as the critical time step size. In such cases, explicit methods can be employed effectively to obtain the solution at a reasonable computational cost.

Implicit methods use Eq. (4.1) at a time for which the solution is not known, to obtain the response at time $t + \Delta t$. The need for the solution of a coupled system of equations makes implicit methods considerably more expensive, computationally, per time step. Hence unconditionally stable implicit schemes are desirable since then

the time step size is chosen to satisfy accuracy requirements alone. The use of larger time steps means, of course, that much less steps are used than with an explicit, conditionally stable procedure.

Implicit integration schemes like the Newmark family of integrators and the Wilson method, Wilson *et al.* [40], are unconditionally stable in linear analyses (with appropriately chosen integration parameters), and are also employed for nonlinear analyses. In performing a nonlinear analysis using an implicit method, it can be of great importance that equilibrium iterations be carried out at each time step, see Bathe [3] and Bathe *et al.* [9], because the solution is highly path dependent and any errors introduced at a particular time may affect the solution at later times. Unfortunately, even with iterations carried out to very tight convergence tolerances, the much desired unconditional stability of these integrators may be lost in the nonlinear regime. A typical example is the trapezoidal rule which is known to conserve the total energy exactly for linear problems, but fails to maintain stability in some nonlinear analyses for reasonable time step sizes. The solution can exhibit a deterioration in the response quality over time with an eventual blow up in energy and momenta.

Much research effort has been directed toward the goal of achieving unconditional stability in nonlinear dynamic analysis of solids and structures. Kuhl and Crisfield [27] have presented a comprehensive survey of the various algorithms that have been formulated in an attempt to achieve stability in numerical solutions of nonlinear problems in structural and solid mechanics. Hughes *et al.* [23] proposed a formulation that is based on the trapezoidal rule, with the constraint of energy conservation enforced by means of Lagrange multipliers which are unknowns in addition to the displacements. However the method still may fail to produce a solution at about the same instant in time as when the underlying time integration scheme fails, Kuhl and Crisfield [27]. The stability of the method can be improved by using a dissipative integration algorithm along with enforcing the energy constraint. But the use of a dissipative integrator with the constraint of energy conservation may result in transfer of the energy contained in damped out higher modes, to lower modes resulting in their amplification and non-conservation of momenta, Kuhl and Crisfield [27]. Kuhl and

Ramm [28] introduced the Constraint Energy Momentum algorithm in the context of nonlinear dynamic analysis of shells. The algorithm was motivated by the formulation proposed in Hughes *et al.* [23], and included the constraints of conservation of linear and angular momenta in addition to the constraint of energy conservation. The algorithm uses the Bossak-α method, which can be obtained as a special case of the Generalized-α method of Chung and Hulbert [15].

Simo and Tarnow [36] showed that the "energy momentum methods" conserve the energy and momenta exactly for conservative problems. However as noted in Kuhl and Ramm [28], the method may fail for reasonable time step sizes in instances where high frequency modes are excited appreciably, indicating the value of some numerical dissipation built into the solution algorithm to damp out the high frequencies that do not contribute significantly to the response and which might be resolved inaccurately with the time step size used. Also, these methods result in non-symmetric tangent stiffness matrices, requiring considerably more computational effort in a full Newton-Raphson iteration. As indicated by Laursen and Meng [30], for general nonlinear material models the energy momentum methods require solution of a scalar variable either at the integration points or over each element in an averaged sense. The effects of the scalar variable have to be accounted for in calculation of the gradient of the vector of internal forces to achieve quadratic convergence in the Newton-Raphson iterations. A modified energy momentum method, Kuhl and Crisfield [27], is shown to be numerically stable and energy decaying, but is not second order accurate.

In this chapter we state the formulation of a single step composite scheme already presented in Baig and Bathe [1], and using this method we solve three test problems. The results are compared with those obtained using the trapezoidal rule to further evaluate the performance of the proposed solution algorithm. The method is attractive since it only operates on the global vectors and uses the usual symmetric matrices, retaining good stability characteristics and second-order accuracy.

4.2 A Composite Trapezoidal-Backward-Difference Procedure

In general, time integration algorithms formulated using backward difference expressions have some amount of numerical damping built into them. The Houbolt method is such an example which uses a four point backward difference approximation, but introduces too much dissipation even in lower modes Bathe [3].

A composite, single step, second order accurate integration scheme for solving first order equations arising in the simulation of silicon devices and circuits was presented by Bank *et al.* [2]. This composite scheme is available in the ADINA program for fluid flow structural interaction problems. The first order fluid flow equations and second-order structural equations are solved fully coupled in time using this procedure, Bathe [4] and Bathe and Zhang [11]. Some initial experience with the algorithm in the context of solid and structural mechanics has been presented in [1]. In this section we briefly present the formulation of the algorithm, and in the next section give the solutions of some test problems to compare the scheme with the usual trapezoidal rule integration. For details on the notation used, see Bathe [3].

Assume that the solution is completely known at time t, and based on that, the solution at time $t+\Delta t$ is to be computed. Let $t+\gamma\Delta t$ be an instant in time between times t and $t+\Delta t$, i.e. $\gamma \in (0,1)$. Then using the trapezoidal rule over the time interval $\gamma\Delta t$, we have the following assumptions on velocity and displacement

$$ {}^{t+\gamma\Delta t}\dot{\mathbf{U}} = {}^{t}\dot{\mathbf{U}} + \frac{{}^{t}\ddot{\mathbf{U}} + {}^{t+\gamma\Delta t}\ddot{\mathbf{U}}}{2}\gamma\Delta t \tag{4.2} $$

and

$$ {}^{t+\gamma\Delta t}\mathbf{U} = {}^{t}\mathbf{U} + \frac{{}^{t}\dot{\mathbf{U}} + {}^{t+\gamma\Delta t}\dot{\mathbf{U}}}{2}\gamma\Delta t \tag{4.3} $$

or after simplification,

$$ {}^{t+\gamma\Delta t}\mathbf{U} = {}^{t}\mathbf{U} + {}^{t}\dot{\mathbf{U}}\gamma\Delta t + ({}^{t}\ddot{\mathbf{U}} + {}^{t+\gamma\Delta t}\ddot{\mathbf{U}})(\frac{\gamma\Delta t}{2})^2 \tag{4.4} $$

Solving for ${}^{t+\gamma\Delta t}\ddot{\mathbf{U}}$ and ${}^{t+\gamma\Delta t}\dot{\mathbf{U}}$ from above equations

$$ {}^{t+\gamma\Delta t}\ddot{\mathbf{U}} = ({}^{t+\gamma\Delta t}\mathbf{U} - {}^{t}\mathbf{U} - {}^{t}\dot{\mathbf{U}}\gamma\Delta t)\frac{4}{\gamma^2\Delta t^2} - {}^{t}\ddot{\mathbf{U}} \tag{4.5} $$

$$ {}^{t+\gamma\Delta t}\dot{\mathbf{U}} = ({}^{t+\gamma\Delta t}\mathbf{U} - {}^{t}\mathbf{U})\frac{2}{\gamma\Delta t} - {}^{t}\dot{\mathbf{U}} \tag{4.6} $$

The equilibrium equation (4.1) at time $t + \gamma\Delta t$ can be written as

$$ \mathbf{M}\,{}^{t+\gamma\Delta t}\ddot{\mathbf{U}} + \mathbf{C}\,{}^{t+\gamma\Delta t}\dot{\mathbf{U}} = {}^{t+\gamma\Delta t}\mathbf{R} - {}^{t+\gamma\Delta t}\mathbf{F} \tag{4.7} $$

Substituting for ${}^{t+\gamma\Delta t}\ddot{\mathbf{U}}$ and ${}^{t+\gamma\Delta t}\dot{\mathbf{U}}$ in the above equation, and linearizing the equation about the most recent configuration, the following expression is obtained (see [3]),

$$ \begin{aligned} ({}^{t+\gamma\Delta t}\mathbf{K}^{(i-1)} + \mathbf{M}\frac{4}{\gamma^2\Delta t^2} + \mathbf{C}\frac{2}{\gamma\Delta t})\boldsymbol{\Delta}\mathbf{U}^{(i)} &= {}^{t+\gamma\Delta t}\mathbf{R} - {}^{t+\gamma\Delta t}\mathbf{F}^{(i-1)} \\ &- \mathbf{M}\left(\frac{4}{\gamma^2\Delta t^2}({}^{t+\gamma\Delta t}\mathbf{U}^{(i-1)} - {}^{t}\mathbf{U}) - \frac{4}{\gamma\Delta t}{}^{t}\dot{\mathbf{U}} - {}^{t}\ddot{\mathbf{U}}\right) \\ &- \mathbf{C}\left(\frac{2}{\gamma\Delta t}({}^{t+\gamma\Delta t}\mathbf{U}^{(i-1)} - {}^{t}\mathbf{U}) - {}^{t}\dot{\mathbf{U}}\right) \end{aligned} \tag{4.8} $$

Once the displacements have been computed, the velocities and accelerations are obtained from the relations given above.

Let the derivative of a function at time $t + \Delta t$ be written in terms of the function values at times t, $t + \gamma\Delta t$ and $t + \Delta t$ as

$$ {}^{t+\Delta t}\dot{f} = c_1\,{}^{t}f + c_2\,{}^{t+\gamma\Delta t}f + c_3\,{}^{t+\Delta t}f \tag{4.9} $$

where

$$ c_1 = \frac{(1-\gamma)}{\Delta t\gamma} \tag{4.10} $$

$$ c_2 = \frac{-1}{(1-\gamma)\gamma\Delta t} \tag{4.11} $$

$$ c_3 = \frac{(2-\gamma)}{(1-\gamma)\Delta t} \tag{4.12} $$

For more details on finite difference formulas for numerical solution of differential equations, see [17]. Writing velocities in terms of displacements and accelerations in terms of velocities, we have

$$^{t+\Delta t}\dot{\mathbf{U}} = c_1\, ^{t}\mathbf{U} + c_2\, ^{t+\gamma\Delta t}\mathbf{U} + c_3\, ^{t+\Delta t}\mathbf{U} \tag{4.13}$$

$$^{t+\Delta t}\ddot{\mathbf{U}} = c_1\, ^{t}\dot{\mathbf{U}} + c_2\, ^{t+\gamma\Delta t}\dot{\mathbf{U}} + c_3\, ^{t+\Delta t}\dot{\mathbf{U}} \tag{4.14}$$

Now writing eq. (4.1) at time $t + \Delta t$ and making use of the above expressions gives

$$\mathbf{M}\, ^{t+\Delta t}\ddot{\mathbf{U}} + \mathbf{C}\, ^{t+\Delta t}\dot{\mathbf{U}} = \, ^{t+\Delta t}\mathbf{R} - \, ^{t+\Delta t}\mathbf{F} \tag{4.15}$$

which on linearizing results in

$$\begin{aligned}
&(c_3c_3\mathbf{M} + c_3\mathbf{C} + \, ^{t+\Delta t}\mathbf{K}^{(i-1)})\boldsymbol{\Delta}\mathbf{U}^{(i)} = \, ^{t+\Delta t}\mathbf{R} - \, ^{t+\Delta t}\mathbf{F}^{(i-1)} \\
&- \mathbf{M}(c_1\, ^{t}\dot{\mathbf{U}} + c_2\, ^{t+\gamma\Delta t}\dot{\mathbf{U}} + c_3c_1\, ^{t}\mathbf{U} + c_3c_2\, ^{t+\gamma\Delta t}\mathbf{U} + c_3c_3\, ^{t+\Delta t}\mathbf{U}^{(i-1)}) \\
&- \mathbf{C}(c_1\, ^{t}\mathbf{U} + c_2\, ^{t+\gamma\Delta t}\mathbf{U} + c_3\, ^{t+\Delta t}\mathbf{U}^{(i-1)})
\end{aligned} \tag{4.16}$$

The solution for $^{t+\Delta t}\mathbf{U}$ and the calculation of the velocities and accelerations from the backward difference approximations in eqs. (4.13) and (4.14) gives the complete response at time $t + \Delta t$.

4.3 Generalization of the Composite Scheme

The idea of using sub-steps in a given time step, and using backward differences to stabilize the results obtained using the trapezoidal rule, can be generalized. For n sub-steps, the trapezoidal rule can be applied $(n-1)$ times, and then obtaining the solution at the end of the time step by an $(n+1)$-point backward difference scheme. For example, if $n = 3$, the sub-steps being equal in size, solution at times $t + \Delta t/3$ and $t + 2\Delta t/3$ can be obtained by two successive applications of the trapezoidal rule. The solution at time $t + \Delta t$ can then be obtained by using the Houbolt method, using solution already obtained at times t, $t + \Delta t/3$ and $t + 2\Delta t/3$, see Bathe [3]. We call

this scheme TR2H for brevity's sake.

However, it may be so that a member of this family of integrators may not remain stable for nonlinear problems in general, and any such scheme must be tested thoroughly before its use can be recommended.

4.4 Accuracy of Analysis

The composite algorithm is numerically tested for accuracy characteristics. Following the approach in Bathe [3], Wilson *et al.* [40] and Bathe and Wilson [10], percentage period elongation and percentage amplitude decay are evaluated. The evaluations are carried out for a simple spring mass system without any physical damping, and with unit initial displacement and zero initial velocity. The curves obtained are given in Figure 4-2, along with the curves for the trapezoidal rule and the Wilson method. The composite scheme performs very well for a fairly large range of $\Delta t/T$, where T is the time period of the spring mass system.

The figures also show the curves calculated for the TR2H scheme, which exhibits considerably more error than the two sub-step composite scheme. This increased numerical dissipation is contributed from the Houbolt method, which is embedded in the scheme and which has considerably more numerical damping than Wilson methd, see [3]. In the following section we present a numerical solution using the TR2H method, and demonstrate that the two sub-step composite scheme is far more accurate.

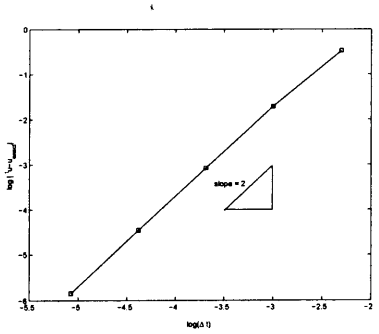

Figure 4-1: Convergence curve for the composite scheme.

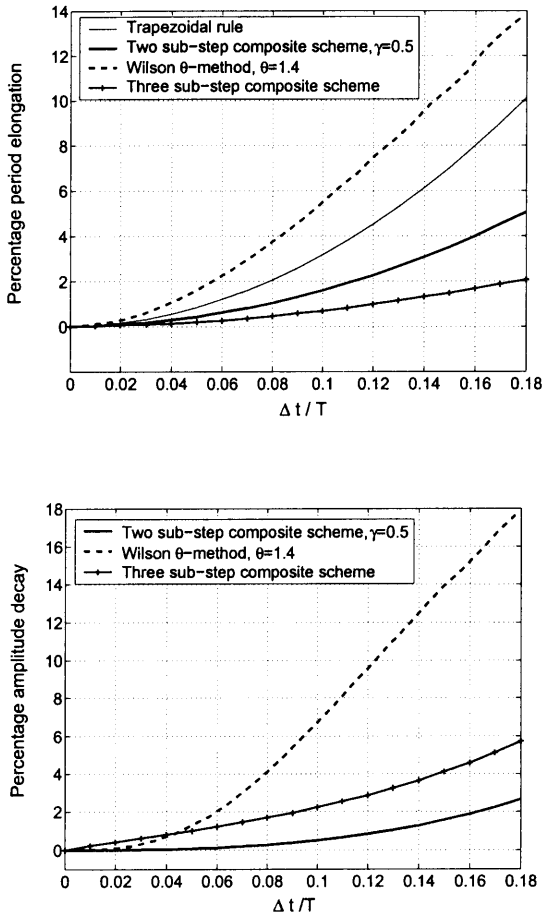

Figure 4-2: Percentage period elongation and amplitude decay for the trapezoidal rule, the Wilson method, the two sub-step composite scheme ($\gamma = 0.5$), and the original composite algorithm.

4.5 Numerical Examples

In this section we present numerical results for three test problems, obtained using both the proposed composite algorithm (with $\gamma = 0.5$) and the trapezoidal rule. Since the composite scheme retains stability due to the numerical damping introduced by the 3-point backward difference method, we also test the Wilson θ-method (which is known to introduce numerical damping as well, see Figure 4-2) in the solution of the problems, with $\theta = 1.4$. The test problems involve large displacements and rotations and the solutions illustrate the instabilities encountered using the trapezoidal rule. We use linear elastic constitutive relations, therefore the nonlinearities in these problems are only due to large deformations.

4.5.1 Rotating Plate

A plate in plane stress conditions, modeled with 4-node elements, is subjected to the loading shown in Figure 4-3. The load is applied normal to the plate boundary for $10\,s$ to give the plate a reasonable angular velocity and is then taken off to have a conservative system from that instant onwards.

The problem is first solved using the trapezoidal rule with $\Delta t = 0.02\,s$. The velocity and acceleration in the z-direction of point A on the plate are plotted along with the angular momentum in Figure 4-4. The response is mainly in the rigid body rotational mode. The period of rigid body rotation is about $12.5\,s$ and therefore the time step chosen should be sufficiently small to capture the response very accurately. However, after about three revolutions of the plate, numerical errors start to accumulate significantly, resulting eventually into very large displacements. Consequently the angular momentum is not conserved, and a point is reached at which the solution can not proceed any further.

The same problem is next solved using the proposed composite formula with $\Delta t = 0.4\,s$ (that is, twenty times the time step used with the trapezoidal rule but of course about twice the computational effort per time step). Figure 4-5 shows that the quality of response remains excellent. In fact, there is a negligible decay in

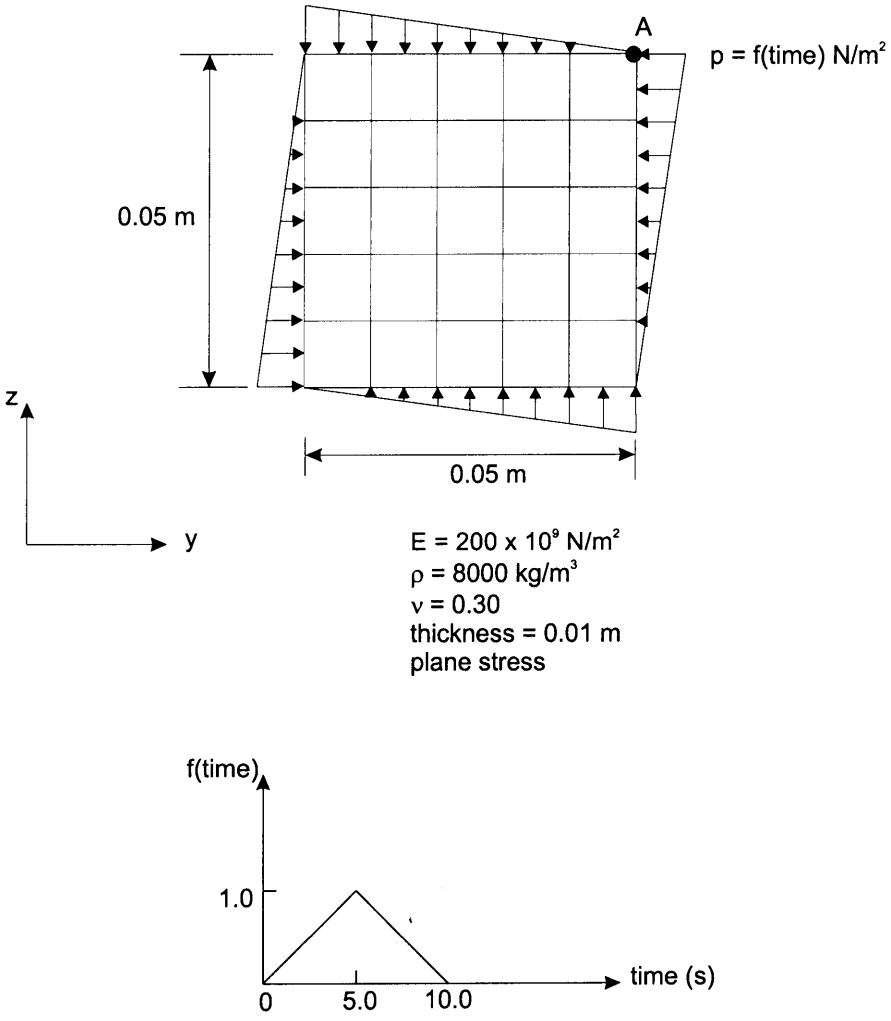

Figure 4-3: The rotating plate problem.

the angular momentum of the plate. This decay is less than 0.06% per revolution for the time step chosen. This solution illustrates the superior and more robust performance of the composite procedure in this long time duration problem. It is also of interest to test the performance of the Wilson θ-method. Using $\Delta t = 0.02\,s$, an accurate solution is also obtained, see Figure 4-6. However, the use of a time step size $\Delta t = 0.1\,s$ resulted in a non-positive definite effective stiffness matrix after only a few time steps, probably because the solution at the discrete time $t + \Delta t$ does not satisfy the dynamic equilibrium accurately (the Newton-Raphson iterations are used to satisfy dynamic equilibrium at time $t + \theta\Delta t$, see [3, 40]), and yet this solution is used for the start of the next time step solution.

For comparison purposes, we also present the solution obtained using the three sub-step composite scheme of Section 3 with $\Delta t = 0.4\,s$, see Figure 4-7. The integration remains stable but has considerably more numerical damping (and of course, for a given step size the computational effort is larger than when using the two sub-step composite algorithm).

4.5.2 Compound Pendulum

Figure 4-8 shows the compound pendulum considered. The bar is initially at rest and released to swing under the action of the constant gravitational field with a period of about $1.25\,s$.

Forty 4-node elements are used to model the pendulum, with 20 elements along the length and 2 in the thickness direction.

The problem is first solved using the trapezoidal rule with a time step $\Delta t = 0.005\,s$. This time step size should be small enough to capture the evolution of response accurately. Figure 4-9 shows the calculated velocity and acceleration in the z-direction at the tip of the bar, along with the kinetic energy of the system. The trapezoidal rule performs well for a certain length of time after which the predicted velocity and acceleration response deteriorates noticeably, eventually resulting in very large velocity and acceleration.

The problem is next solved using the composite scheme with $\Delta t = 0.01\,s$, which

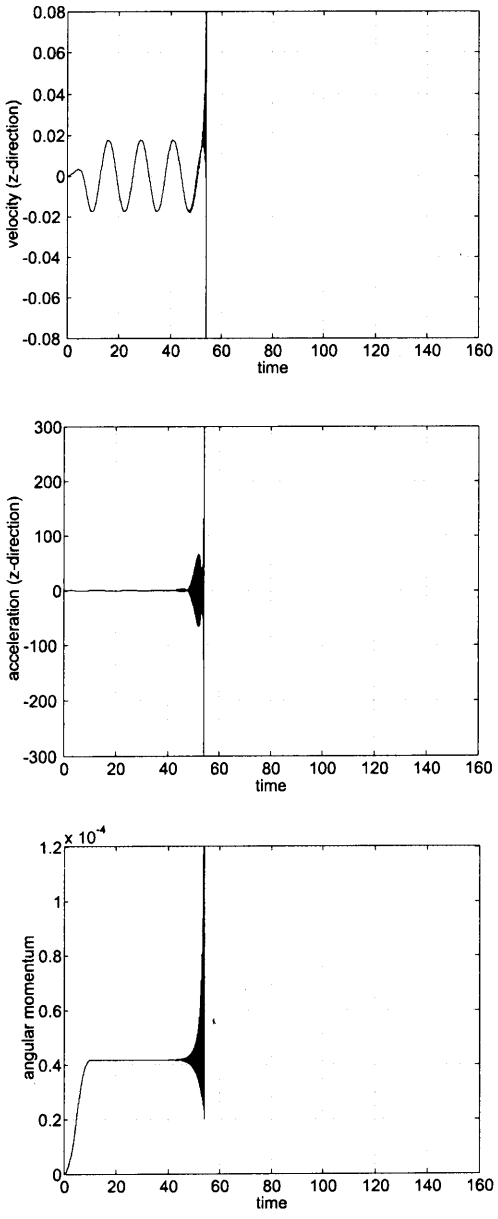

Figure 4-4: The rotating plate problem; results using the trapezoidal rule; $\Delta t = 0.02\,s$.

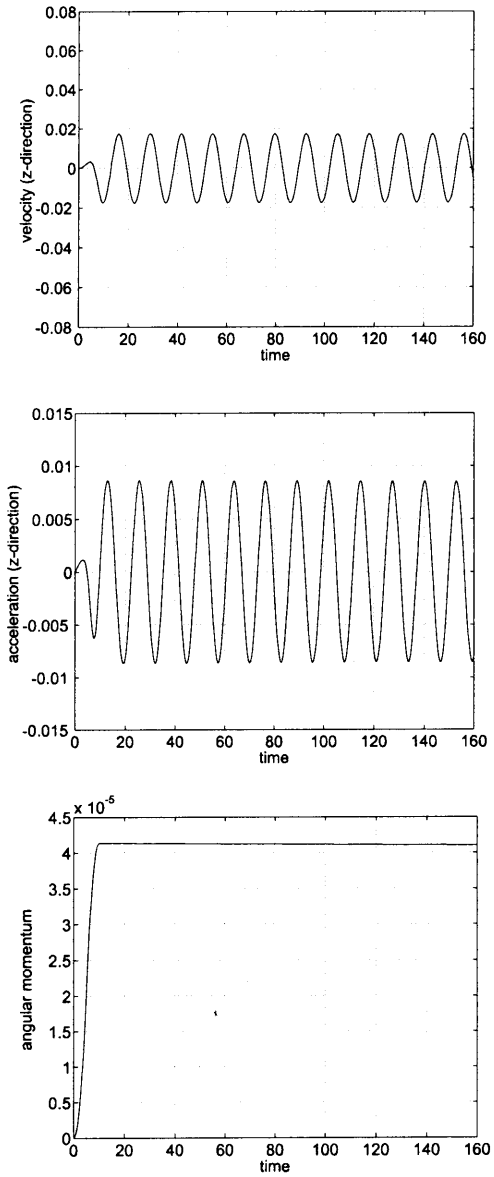

Figure 4-5: The rotating plate problem; results using the composite scheme; $\Delta t = 0.4\,s$.

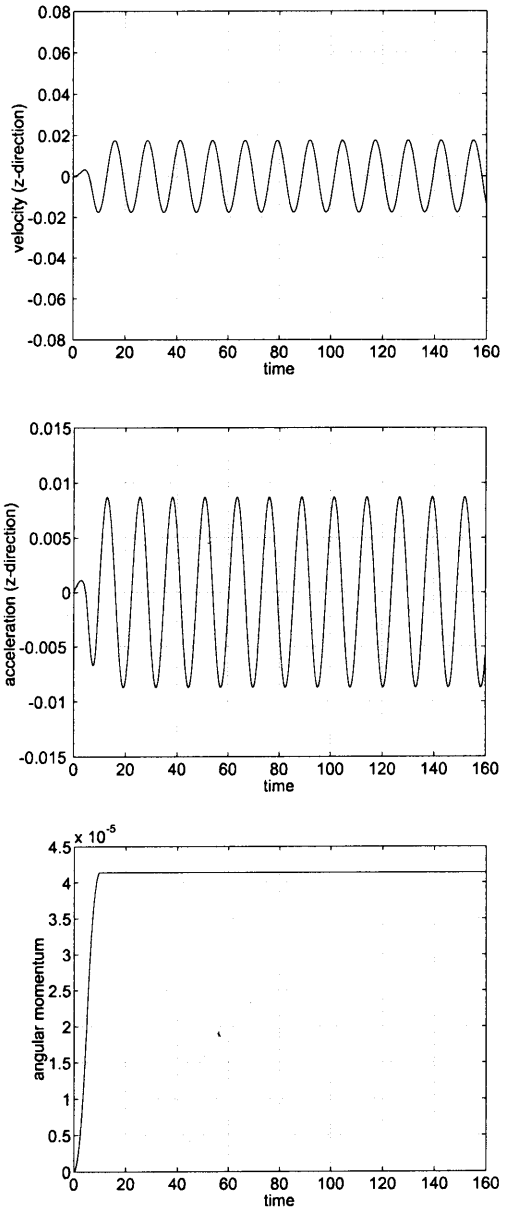

Figure 4-6: The rotating plate problem; results using the Wilson θ-method; $\Delta t = 0.02\,s$.

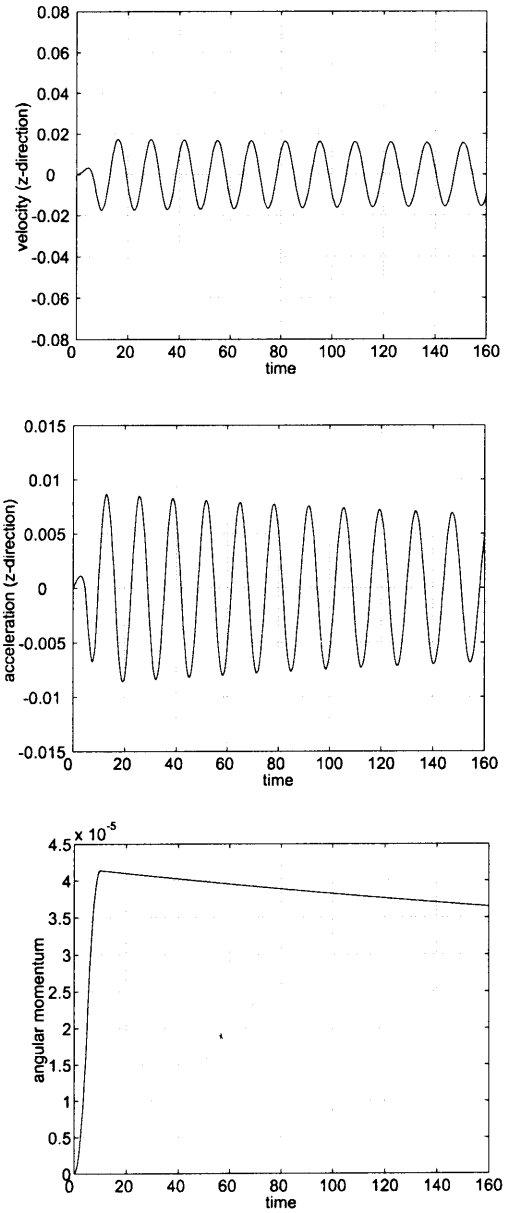

Figure 4-7: The rotating plate problem; results using the three sub-step composite scheme; $\Delta t = 0.4\,s$.

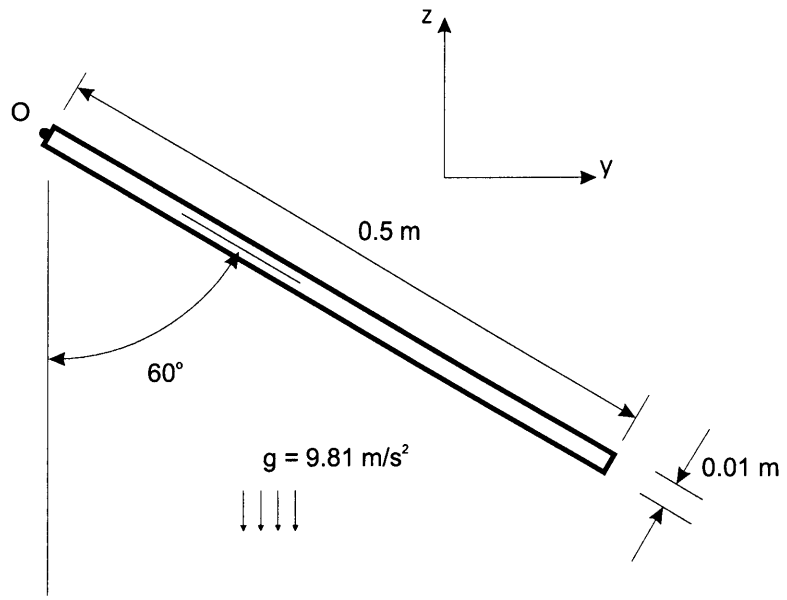

$E = 200 \times 10^9$ N/m^2
$\nu = 0.3$
$\rho = 8000$ kg/m^3
thickness = 0.01 m
Plane stress

Figure 4-8: The compound pendulum in its initial configuration.

requires about the same solution effort as using the trapezoidal rule with $\Delta t = 0.005\,s$. The composite scheme performs well, giving a good velocity and acceleration response, as seen in Figure 4-10 which also shows the evolution of kinetic energy of the bar. Although the response for only the first $20\,s$ is shown, the problem was actually run for a total time of $150\,s$, and the solution was observed to stay stable and accurate. Also, in our experience, the algorithm remains stable if a larger time step is used, introducing, however, greater numerical damping resulting in reduced accuracy of the solution. This loss of accuracy due to the increase in numerical damping is illustrated in Figure 4-11, which shows the results obtained using the composite scheme with $\Delta t = 0.02\,s$, and more so in Figure 4-12 which shows the results obtained using the composite scheme with $\Delta t = 0.04\,s$.

Next we solve the problem using the Wilson θ-method with $\Delta t = 0.005\,s$. Figure 4-13 shows the solution obtained which is very accurate. Figure 4-14 shows the solution calculated using the Wilson θ-method with $\Delta t = 0.02\,s$ and this figure shows that the solution accuracy is similar to when using the composite scheme with $\Delta t = 0.04\,s$. Since the composite scheme uses two solutions per time step, the solution effort is about the same in these two cases. However, the use of a larger time step, e.g. $\Delta t = 0.03\,s$, with the Wilson θ-method resulted in a non-positive definite effective stiffness matrix after only a few steps (an instability we also encountered in the previous example).

4.5.3 Cantilever Beam

The response solved for in the two previous test problems involved large rigid body motions over long time intervals. Here we consider the cantilever beam shown in Figure 4-15, modeled with a 400×1 mesh of 9-node elements and subjected to pressure loading. The beam is supported to prevent rigid body motion but undergoes large displacements.

Figures 4-16 to 4-18 show the calculated response of the beam at its tip using the trapezoidal rule, the composite scheme and the Wilson θ-method. As in the solution of the previous problems considered, the solution provided by the trapezoidal rule

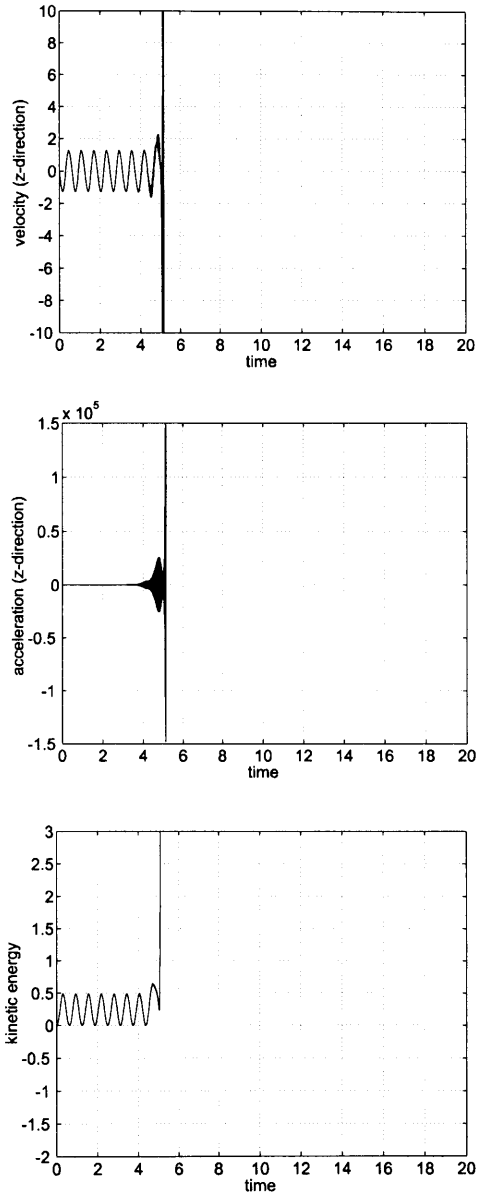

Figure 4-9: The compound pendulum; results using the trapezoidal rule; $\Delta t = 0.005\,s$.

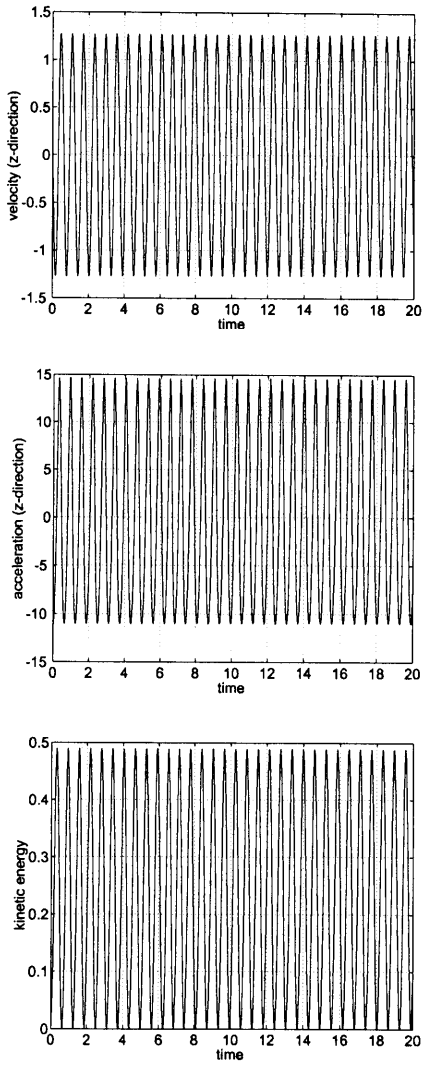

Figure 4-10: The compound pendulum; results using the composite scheme; $\Delta t = 0.01\ s$.

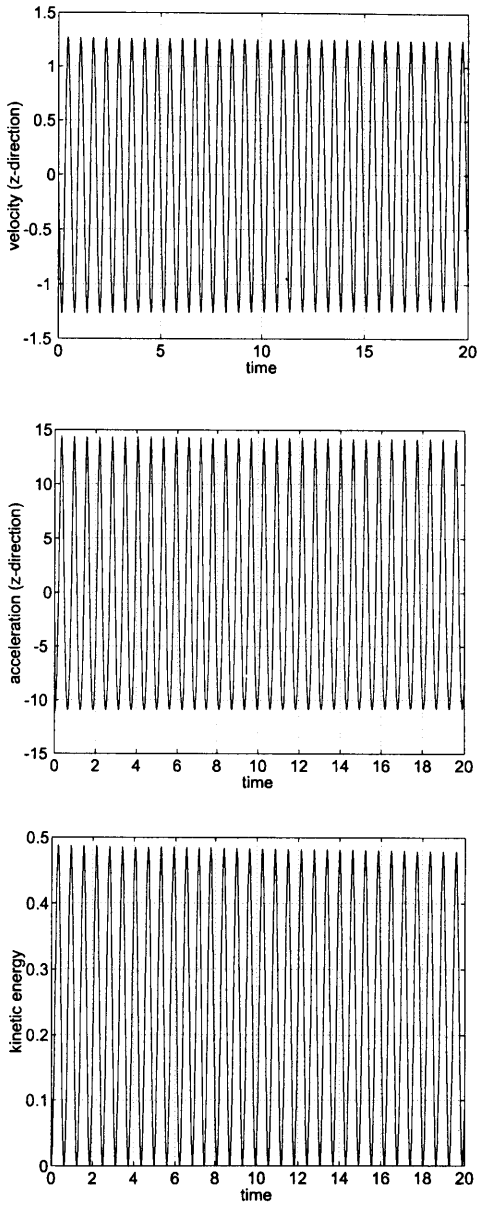

Figure 4-11: The compound pendulum; results using the composite scheme; $\Delta t = 0.02\,s$.

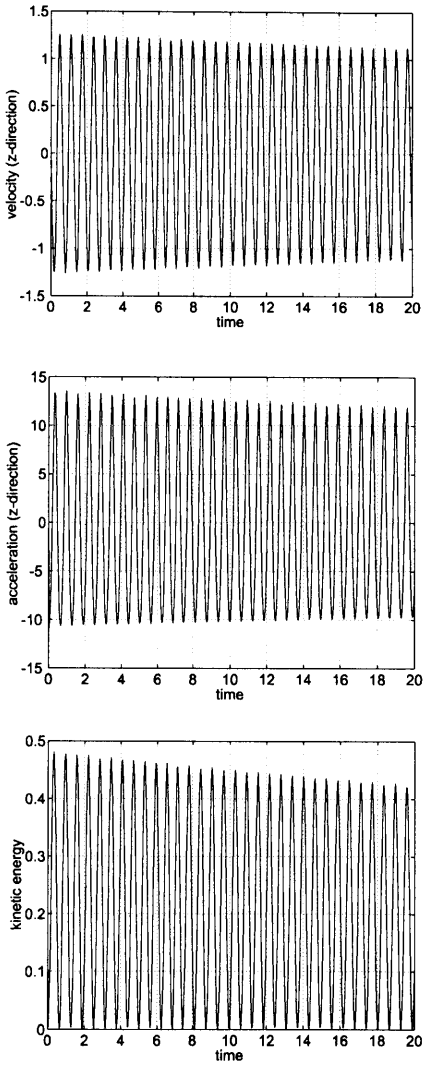

Figure 4-12: The compound pendulum; results using the composite scheme; $\Delta t = 0.04\,s$.

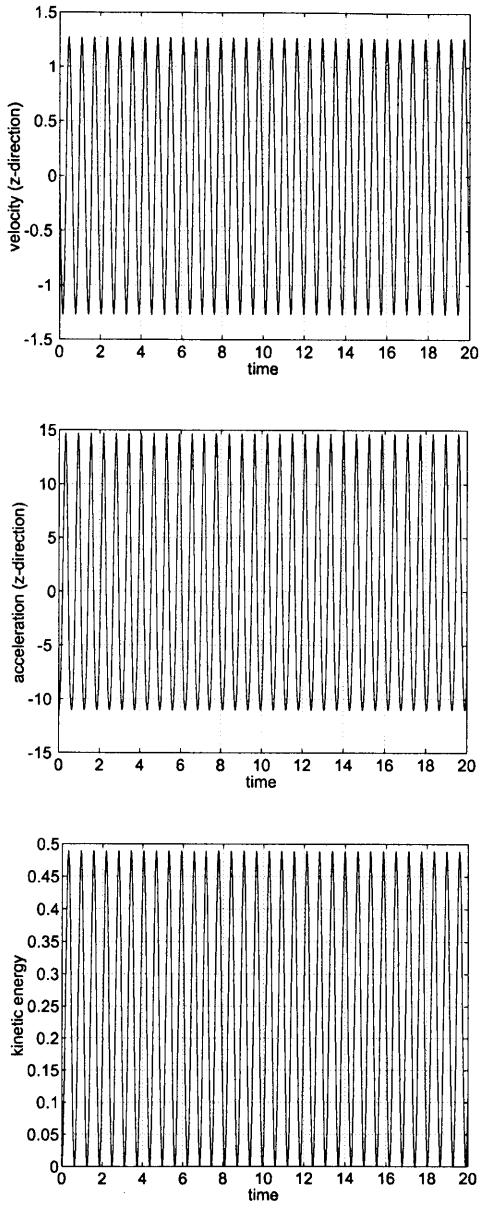

Figure 4-13: The compound pendulum; results using the Wilson θ-method; $\Delta t = 0.005\,s$.

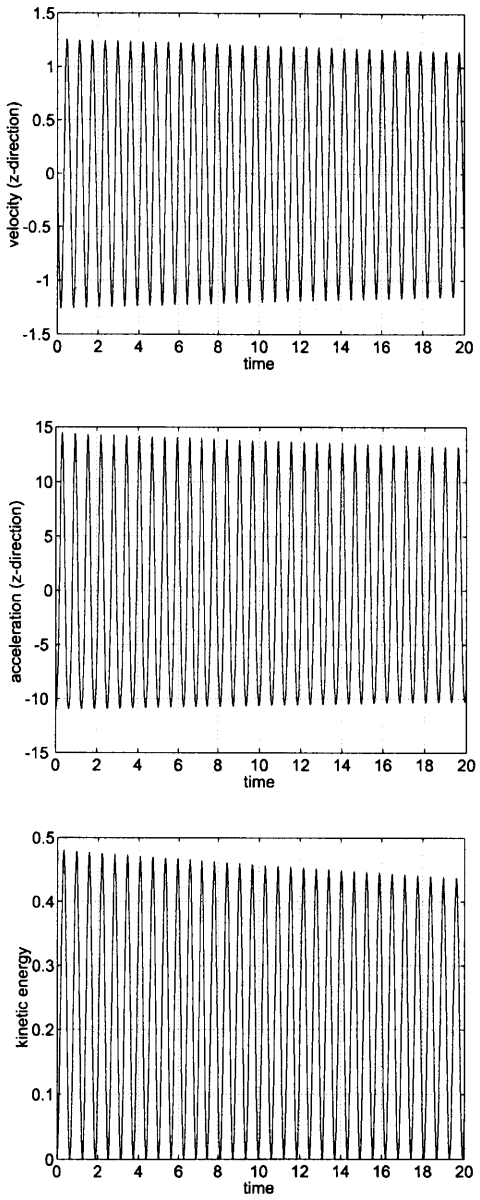

Figure 4-14: The compound pendulum; results using the Wilson θ-method; $\Delta t = 0.02\,s$.

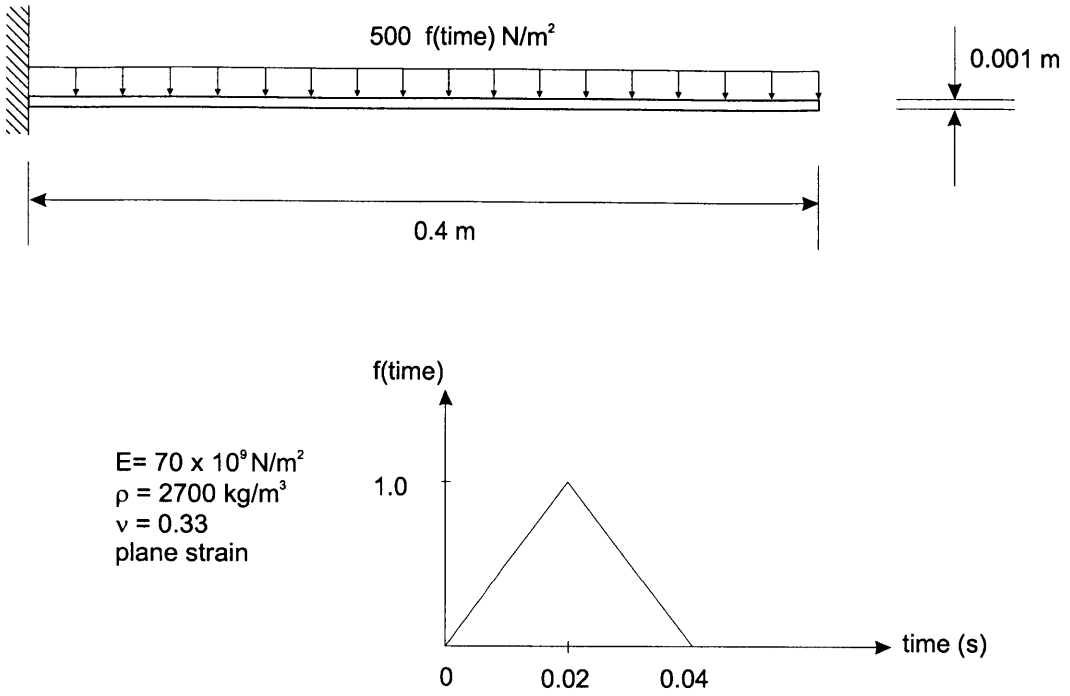

Figure 4-15: Cantilever beam modeled using 9-node elements

is not acceptable, whereas the composite scheme and the Wilson θ-method perform well.

4.6 Conclusions

We have presented a composite single step time integration scheme based on a combination of the trapezoidal rule and a three point backward difference approximation, that does not need any special starting procedure. The performance of the scheme relative to the trapezoidal rule and Wilson-θ was demonstrated by solving test problems that are commonly employed to test time integration methods for stability and energy and momentum conservation. For a given time step size the scheme is about twice as expensive computationally as the usual trapezoidal rule, and hence the method is only of interest for analysis cases where the composite scheme provides much more stability and accuracy than the trapezoidal rule. The Wilson method on the other hand, performs much better in these large diplacement problems. However, the fact

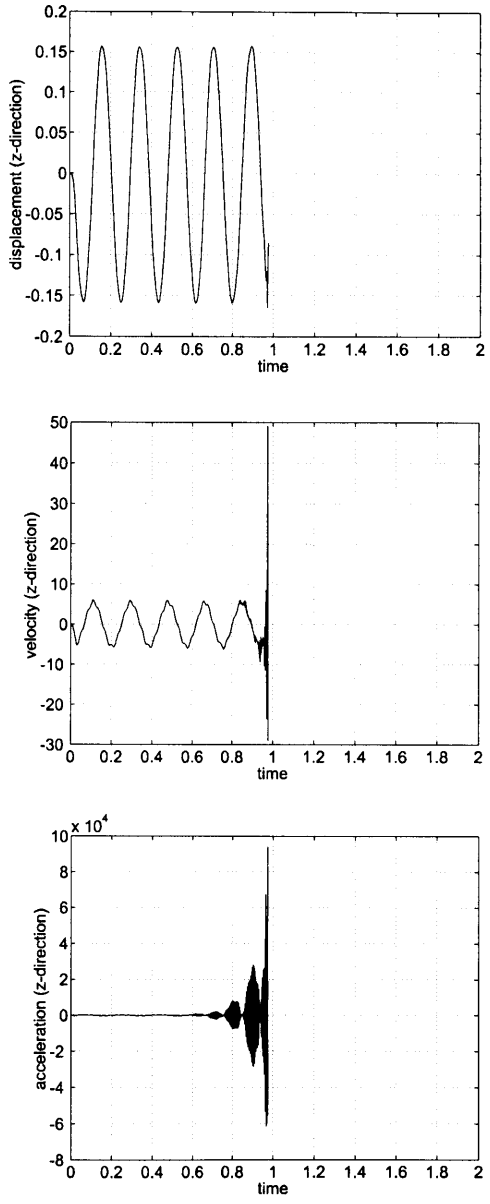

Figure 4-16: Cantilever beam; results using the trapezoidal rule; $\Delta t = 0.002\,s$.

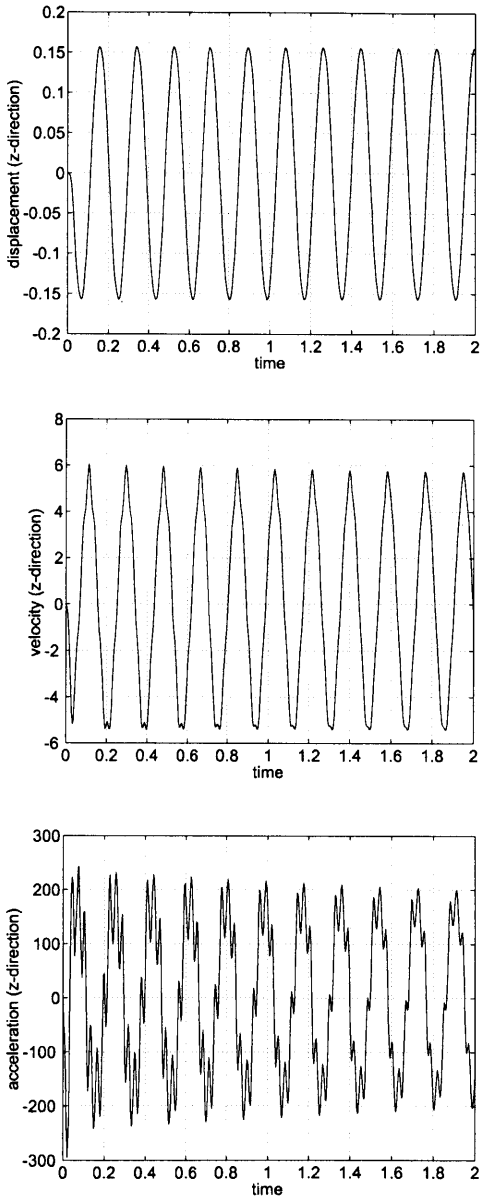

Figure 4-17: Cantilever beam; results using the composite scheme; $\Delta t = 0.004\,s$.

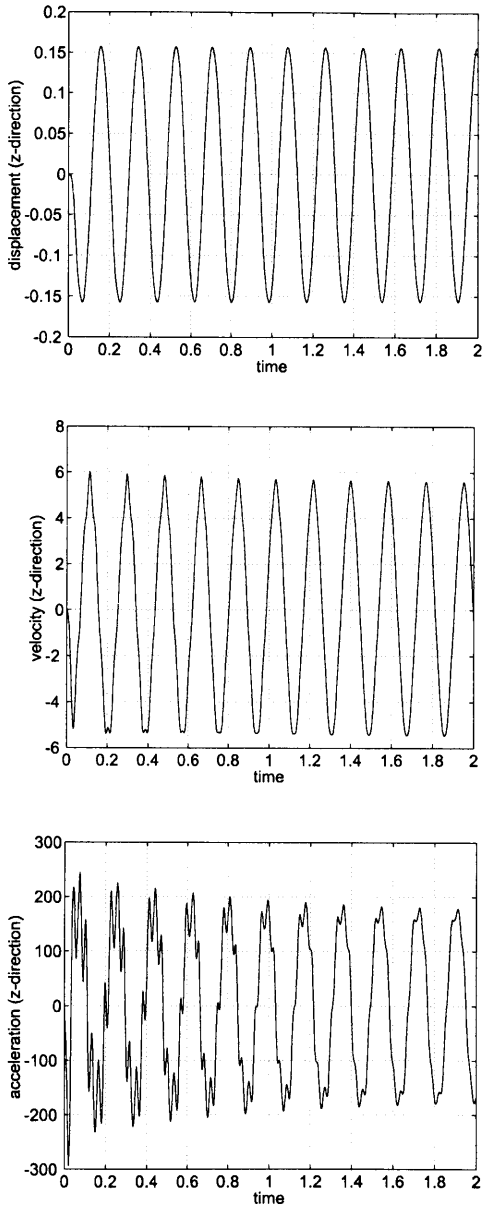

Figure 4-18: Cantilever beam; results using the Wilson θ-method; $\Delta t = 0.002\,s$.

that in Wilson method, equilibrium is *not* satisfied at time $t + \Delta t$, is a drawback in general nonlinear problems involving inelastic deformations. Equilibrium iterations are performed at time $t+\theta\Delta t$, (see [3], and then results are interpolated back at time $t+\Delta t$, in a sense rendering the results less accurate. The composite scheme presented does not suffer from this shortcoming, while at the same time having comparable accuracy, employing even larger time steps than possible with Wilson method. The numerical examples solved show the algorithm to remain stable for large time step sizes; but at relatively larger time steps the numerical damping can be appreciable in the system. Therefore care needs to be exercised in the selection of the time step size. However the method is attractive because it operates on the usual symmetric stiffness and mass matrices, and can be easily implemented, without requiring any coding at the element level; moreover no additional unknown variables need to be solved for in the form of Lagrange multipliers. Therefore the algorithm appears to be of value in instances where the more frequently used trapezoidal rule fails, providing stable and accurate results.

Chapter 5

Dynamic Contact

5.1 Motivation

In dynamic analysis involving contact, instabilities may arise in the numerical solutoin. Though displacement compatability may be satisfied, the velocity and acceleration compatability at the contacting surface may be violated in the normal direction. Moreover, in the presence of frictional contact there may arise situations where the frictional tractions undergo sudden reversals of direction, with the potential for high frequencies to be introduced, though with magnitude so small that the general solution may not be affected. In an implicit solution, the time step size will be usually large enough that highest frequencies are not accurately resolved. In such conditions, solution obtained using such integration schemes, e.g. trapezoidal, rule may become unstable after some time. Much research has been directed towards overcoming these problems. Among the earliest techniques is the post-impact correction presented in Mijailovich and Bathe [32] which attemps to satisfy the velocity and acceleration compatability at the contact nodes by conserving the momentum in the normal direction. This technique works well in many instances where unstable solutions may be obtained otherwise. Also it was reported earlier in Chaudhary and Bathe [14] that using $\alpha = 0.5$ and $\delta = 0.5$ is the implicit Newmark method (see Bathe [3]) improves the quality of solution in many cases. Later much research was directed towards devising time integration schemes that conserved both energy and momenta

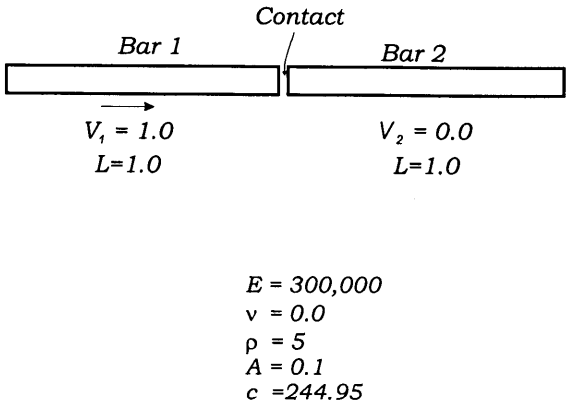

Figure 5-1: Two impacting bars.

in the context of nonlinear dynamic anlaysis, e.g. Simo and Tarnow [36]. Based on this "energy-momentum" approach a solution strategy was proposed in Laursen and Chawla [29] for dynamic contact problems, which however produces solutions that violate the no-penetration condition at the contacting surfaces. Moreover energy-momentum methods may become complicated and are dependent on the continuum finite element formulation and the material model used, as stated in Chapter 4.

In the following examples, the composite direct time integration scheme presented in Chapter 4 is employed (see also Baig and Bathe [1], and Bathe and Baig [5]), resulting in accurate and stable solutions and no special treatment of solution variable at the the contacting nodes is required. Such independency of time integration from the nature of the problem is highly desirable as the scheme is then more general and applicable to a broad spectrum of problems.

5.2 Two Impacting Bars

The problem involves the impact of one bar moving with a constant velocity, on another similar but stationary bar, Figure 5-1.

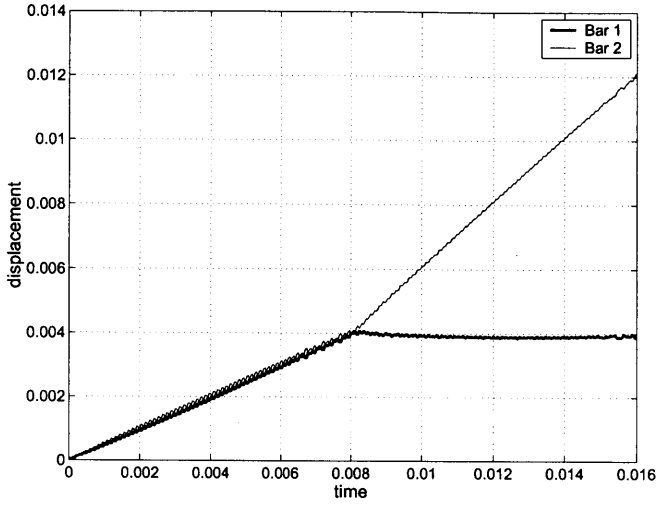

Figure 5-2: The displacements of contacting faces; trapezoidal rule, $\Delta t = 0.00004$ s.

This problem demonstrates that the widely used trapezoidal rule may produce spurious oscillations in the response obtained in dynamic contact problems. Also, since the trapezoidal rule in linear analysis does not introduce any numerical damping, any oscillations introduced in nonlinear contact solution may get amplified, resulting in a blow up of energy of the system.

Each bar is modeled using 100 four node element. The material properties are as given in Figure 5-1. The problem is first solved using the trapezoidal rule with time step size $\Delta t = 4 \times 10^{-5} s$. This time step is chosen based on the element length and the one-dimensional wave velocity, since this is known to give the optimal solution for wave propagation problems in 1D. Figures 5-2 and 5-3 show the calculated displacement and velocity response of the two bars at contacting faces. The displacement compatibility is seen not to be satisfied, during the interval in which the impacting faces remain in contact (time time for the wave to travel to the end of the bar, reflect and return). The numerical solution shows "bouncing" of the faces. This results into much worse velocity response. In fact the velocities are highly oscillatory and are not even close to the exact solution.

The problem is next solved using the composite time integration scheme, Baig and Bathe [1], Bathe and Baig [5]. The time step size is $\Delta t = 8 \times 10^{-5}$, i.e. twice the size of the step used with the trapezoidal rule, so that the solution effort is

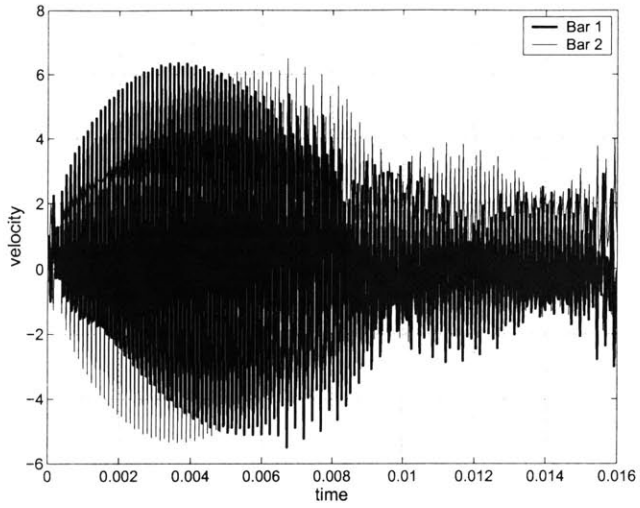

Figure 5-3: The velocities of contacting faces; trapezoidal rule, $\Delta t = 0.00004$ s.

comparable. Figures 5-4 and 5-5 show the response obtained. The displacement and velocity compatibility is satisfied exactly, and the numerical solution is close to the exact solution of the problem. The oscillations in the velocity response once the bars separate is due to the numerical dispersion of the wave in the bar, and is only due to the discretization, and not introduced due to the contact condition.

Figures 5-6 and 5-7 show the evolution of the energy of the bars, and clearly the use of the trapezoidal rule results in an overall increase of the totaly energy, with the oscillations corresponding to the "bouncing" of the contacting faces. The composite integration scheme, on the other hand, produces a slight attenuation in the energy, which corresponds to the damping in the highest frequencies. This example illustrates the merits of using the composite scheme for dynamic contact problems.

5.3 Shaking Table

Figure 5-8 shows a shaking table resting on roller supports, such that the table is free to move in the horizontal direction. A smaller block lies on the table, resting freely under its own weight, as well as an externally applied pressure p. The left end of the shaking table is displaced as time evolves, governed by the sine function given in the figure. There is a normal contact pressure between the contacting surfaces,

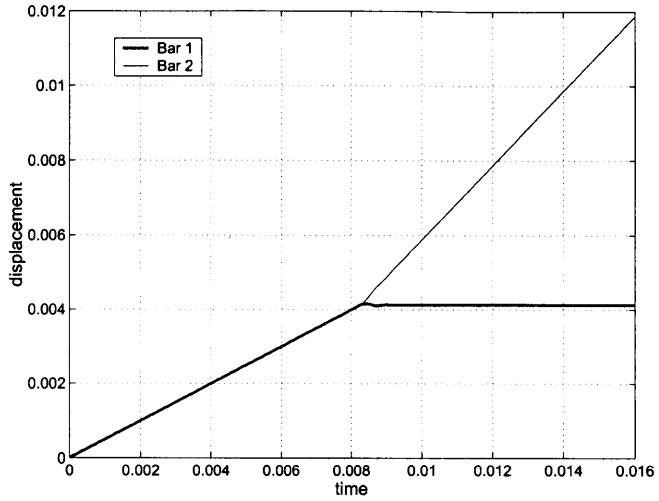

Figure 5-4: The displacements of contacting faces; composite scheme, $\gamma = 0.5$, $\Delta t = 0.00008$ s.

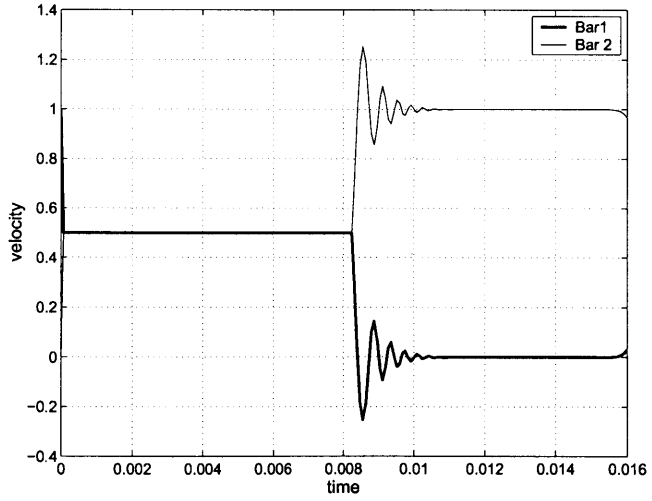

Figure 5-5: The velocities of contacting faces; composite scheme, $\gamma = 0.5$, $\Delta t = 0.00008$ s.

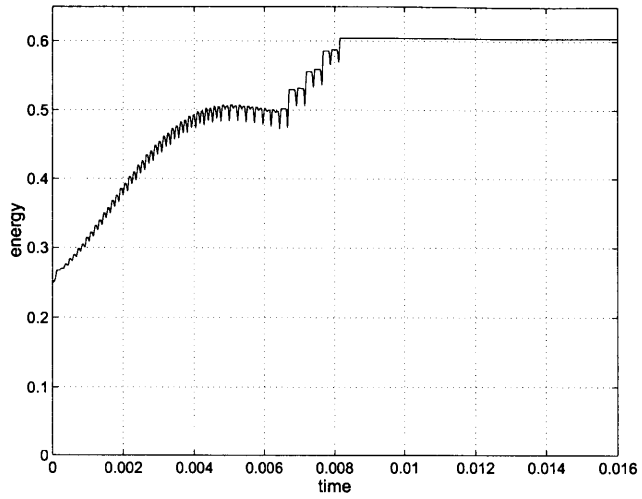

Figure 5-6: The total energy of the two bars obtained using the trapezoidal rule.

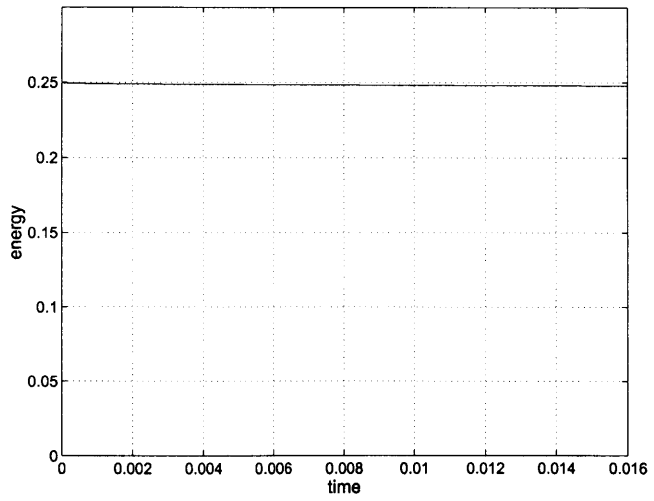

Figure 5-7: The total energy of the two bars obtained using the composite scheme.

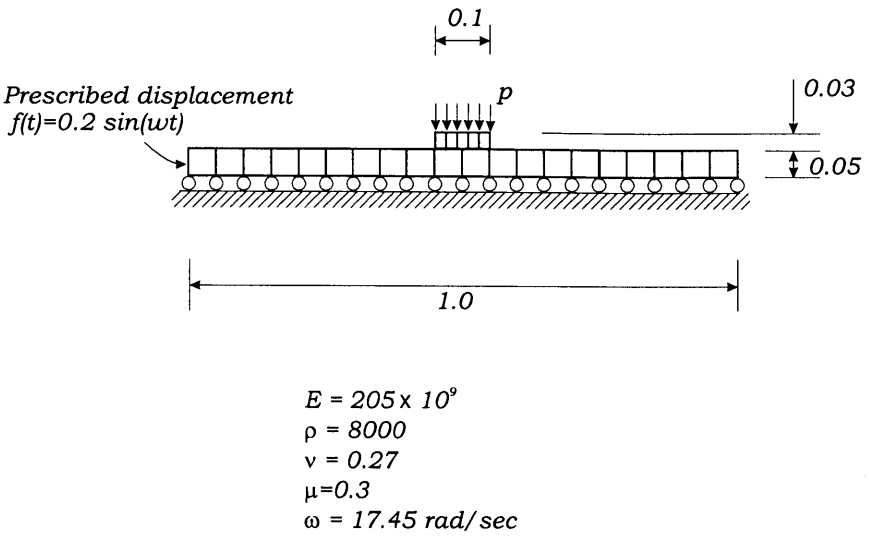

Figure 5-8: The shaking table problem.

and the total normal contact force is always equal to the sum of the weight of the block and the total externally applied force ($\int p\,dS$, where S is the area over which p acts). Friction contact tractions resulting from any relative velocity between the contact surfaces are computed using the Coulomb friction law.

The problem is solved using the composite time integration scheme (Chapter 4) with the consistent segment algorithm for contact conditions. The analysis is performed initially with $p = 0$. The time step used is $\Delta t = 0.005$ with constraint function parameter $\epsilon_t = 10^{-2}$, and the analysis is run for a total of 500 steps. The normal contact pressure in this case is low enough for there to be no stick conditions between the block and the table at any instant. The magnitude of total frictional contact force is always constant at its maximum value (coefficient of friction times weight of the block), and therefore the horizontal acceleration of the block resembles a square wave function. The velocity response of the block, in turn looks like a saw-tooth function. The displacemnet of the block is then piecewise quadratic. Figures 5-9 and 5-11 show these results which are virtually identical for both 4 node and 9 node elements used in the analysis. In figure 5-9, the velocities for both the block and the table are plotted, which clearly show that a stick condition is never encountered, and also confirmed by the displacement response given in figure 5-10. Also in figure 5-11, the acceleration is

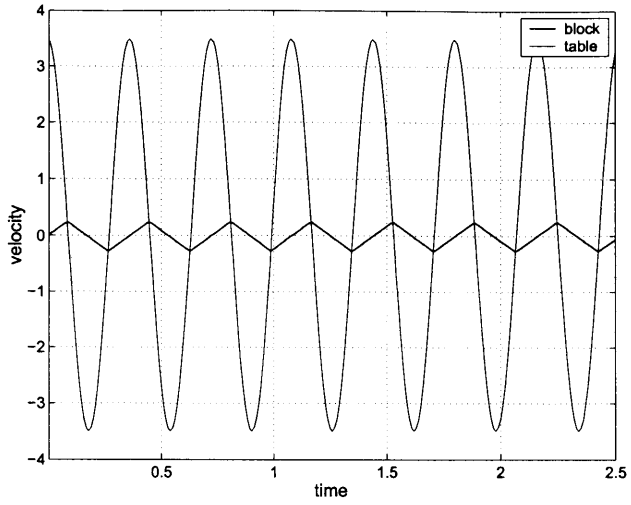

Figure 5-9: The velocity response of the table and the block; $p = 0$.

seen to be captured very accurately with its magnitude remaining constant over the entire run.

Figures 5-12 to 5-15 show the normal and frictional contact stresses at all time steps, for analyses performed using both the 4-node and 9-node element. The contact stress distributions has virtually only two profiles (except for the first couple of steps), as can be seen from these figures, depending on the direction of the relative sliding.

The analysis is next performed using a large value of the applied pressure p, so that the frictional tractions are high enough to keep the block in a state of stick with the shaking table. $p = 50000$ is used, with the same time step size as employed earlier. Figure 5-16 shows the velocity response of both the table and the block. The two curves lie overlapping each other for the entire run, indicating continued sticking of the contact surfaces. Figure 5-17 shows the acceleration response of the block.

Figures 5-18 to 5-19 show the contact stress distribution for all time steps, for this applied pressure p. The contact stress profiles vary from two extremes, to all possible (with the time step size used) variations in between. Although the quality of the solution using the 4-node elements is good, the profiles obtained using 9-node elements are smoother as expected, and also resolve the sharper gradient of stress distribution near the edges, more accurately.

Finally, the problem is solved with a somewhat reduced applied pressure, to ob-

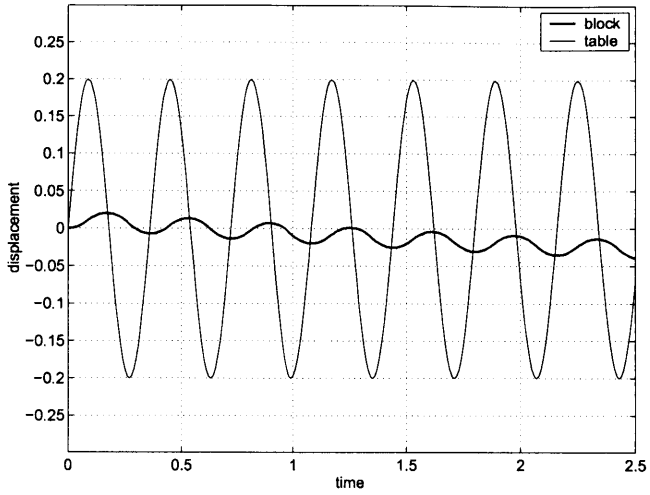

Figure 5-10: The displacements of the table and the block; $p = 0$.

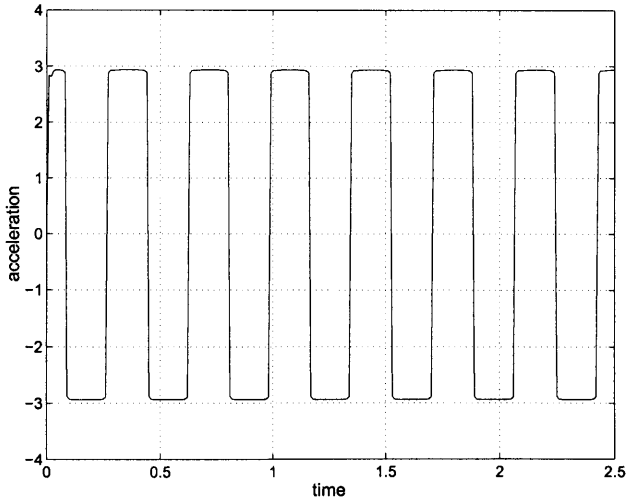

Figure 5-11: The acceleration response of the block; $p = 0$.

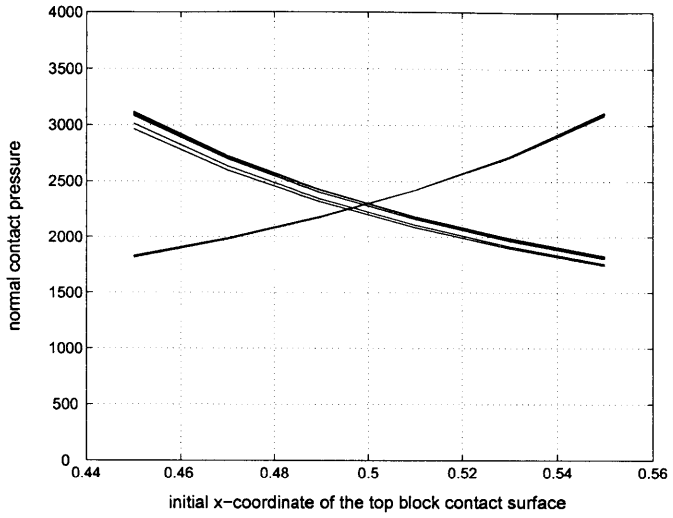

Figure 5-12: The normal contact distributions (for all time steps), 4-node elements; $p = 0$.

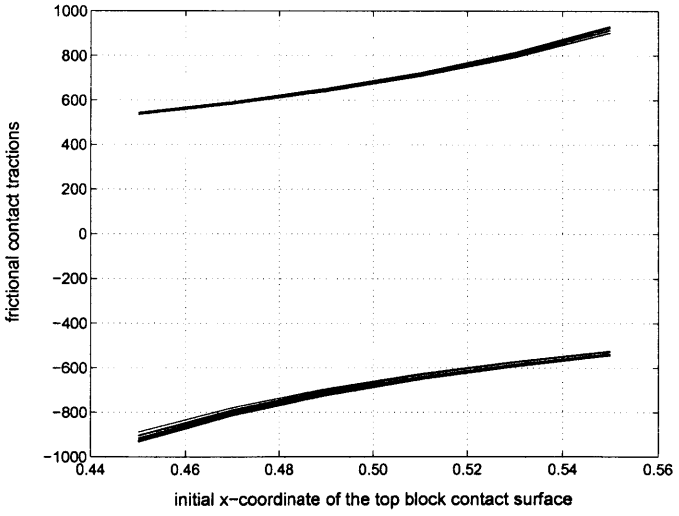

Figure 5-13: The frictional contact distributions (for all time steps), 4-node elements; $p = 0$.

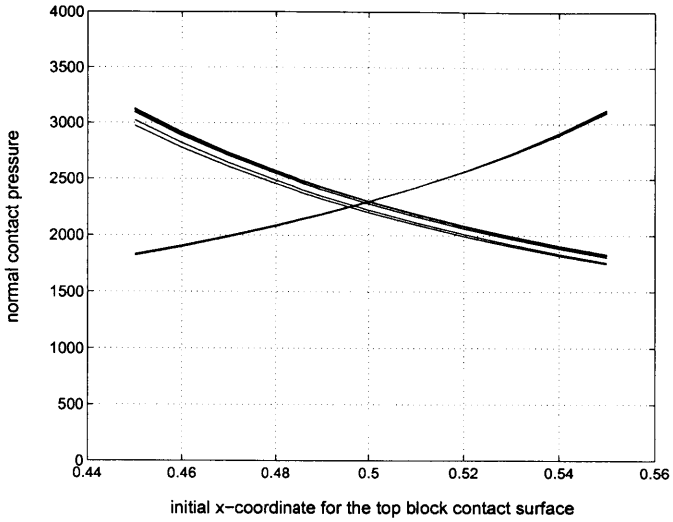

Figure 5-14: The normal contact distributions (for all time steps), 9-node elements; $p = 0$.

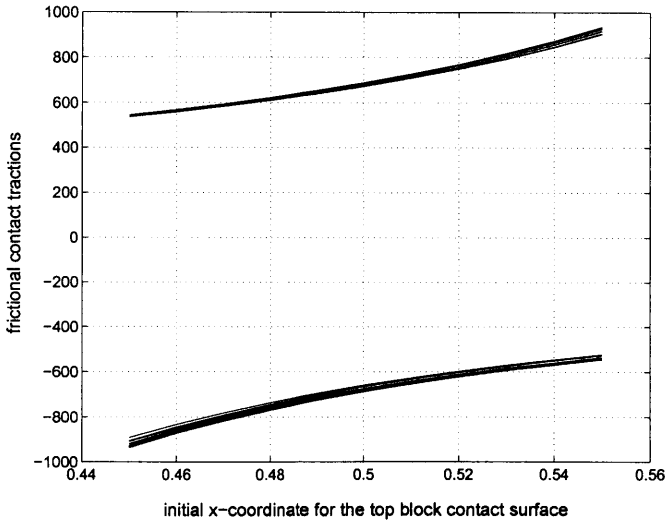

Figure 5-15: The frictional contact distributions (for all time steps), 9-node elements; $p = 0$.

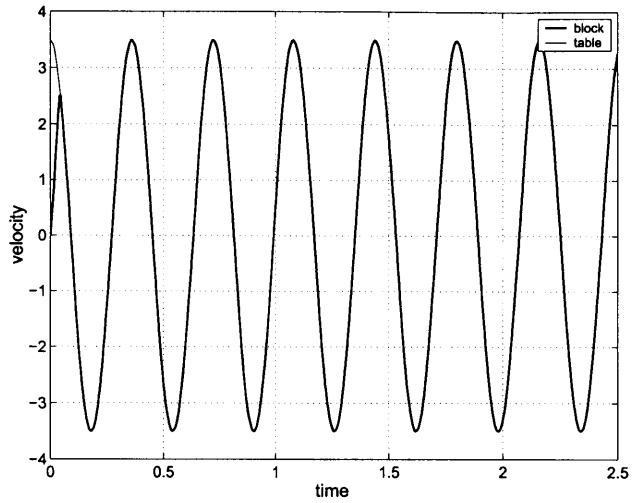

Figure 5-16: The velocity response of the table and the block; $p = 50000$.

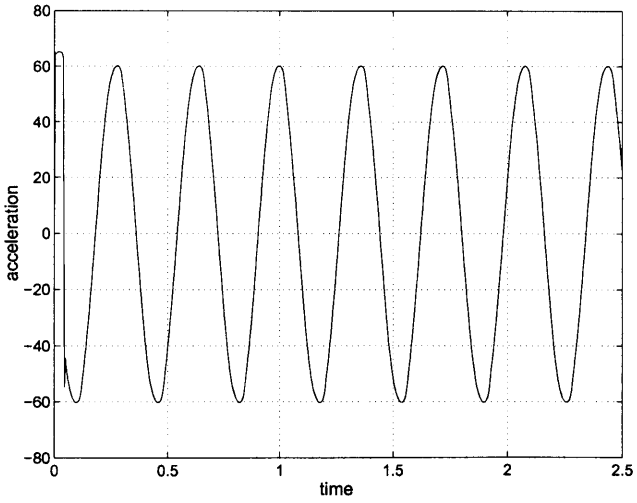

Figure 5-17: The acceleration response of the block; $p = 50000$.

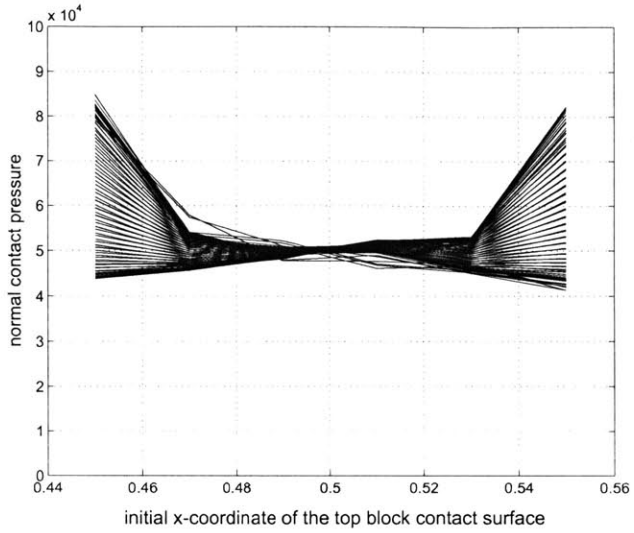

Figure 5-18: The normal contact distributions (for all time steps), 4-node elements; $p = 50000$.

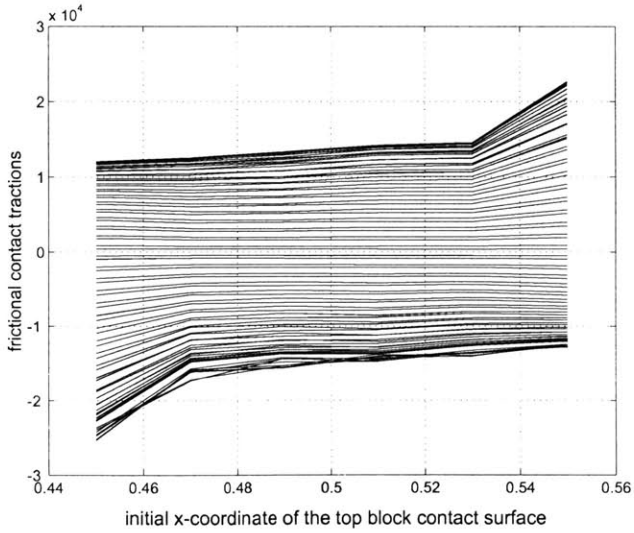

Figure 5-19: The frictional contact distributions (for all time steps), 4-node elements; $p = 50000$.

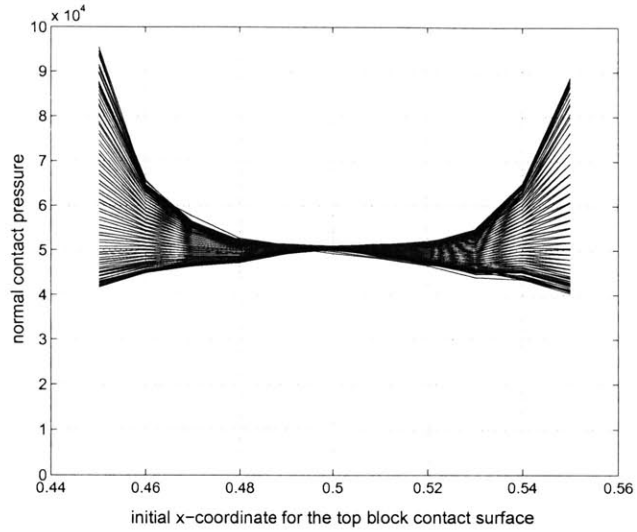

Figure 5-20: The normal contact distributions (for all time steps), 9-node elements; $p = 50000$.

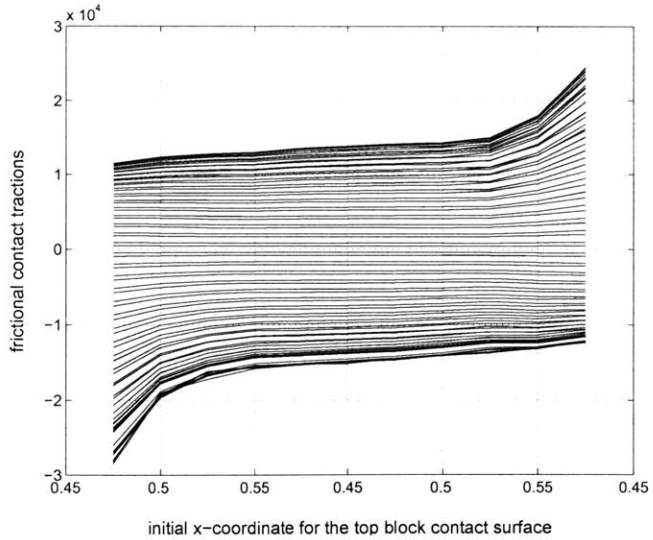

Figure 5-21: The frictional contact distributions (for all time steps), 9-node elements; $p = 50000$.

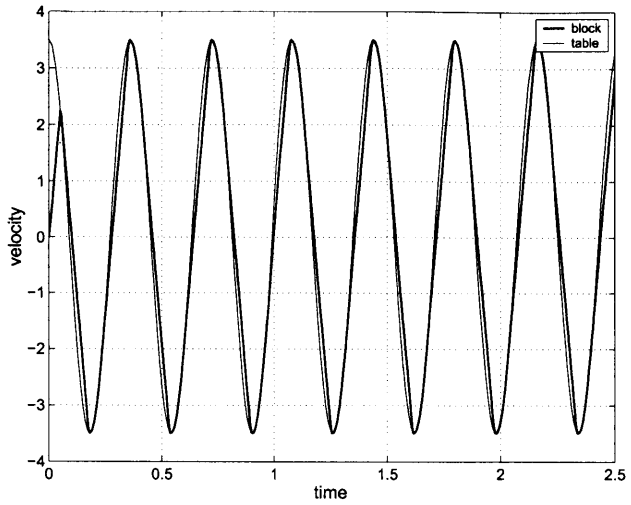

Figure 5-22: The velocity response of the table and the block; $p = 35000$.

serve both stick and slip conditions in the response of the block. $p = 35000$ is used, with the same time step size, again using both 4-node and 9-node elements. Figures 5-22 and 5-23 show the velocity response of the the block and the table. From figure 5-23 it is clearly seen that the velocities of the two surfaces over lap where there is a stick condition, and then separate and sliding (releasing) takes place. Acceleration of the block, figure 5-24 is seen to have a sharp discontinuity when there is a sliding condition, but exhibiting a milder and rounder gradient close to the stick conditions. Figures 5-25 to 5-28 show the contact traction distributions for all time steps, obtained using 4-node and 9-node elements.

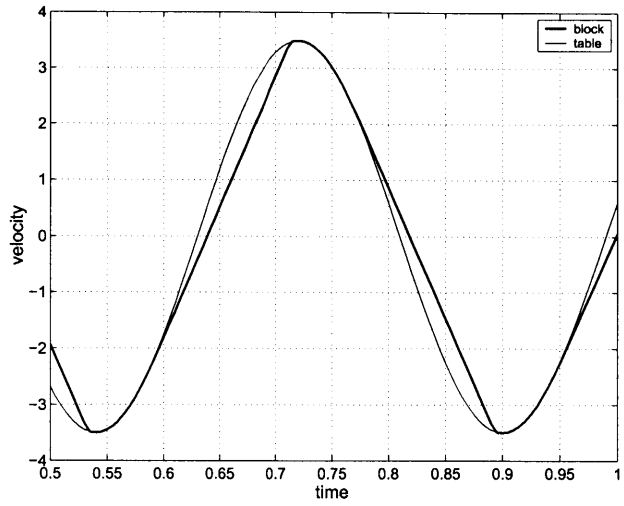

Figure 5-23: The velocity response of the table and the block; $p = 35000$.

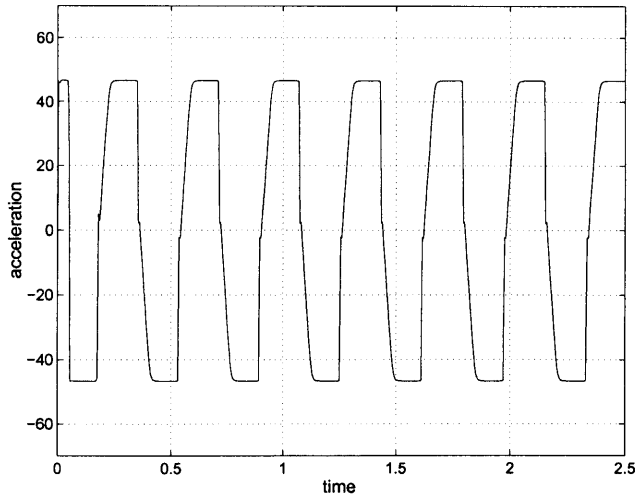

Figure 5-24: The acceleration response of the block; $p = 35000$.

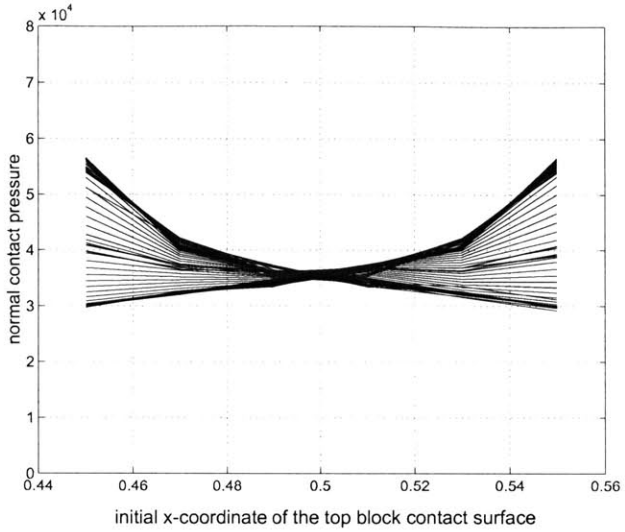

Figure 5-25: The normal contact distributions (for all time steps), 4-node elements; $p = 35000$.

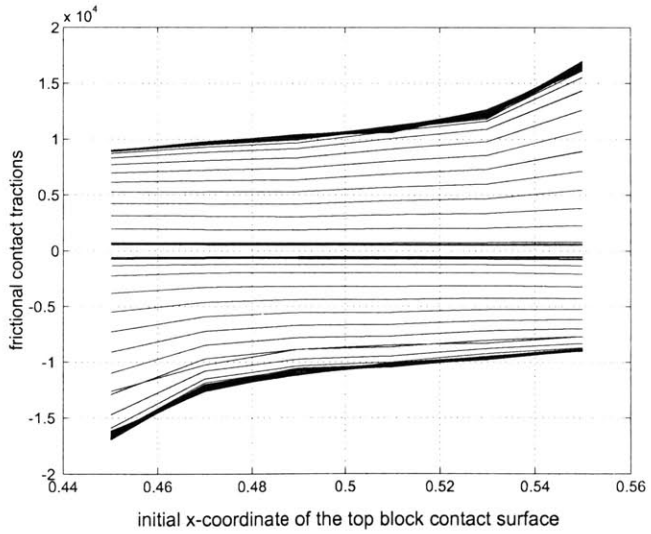

Figure 5-26: The frictional contact distributions (for all time steps), 4-node elements; $p = 35000$.

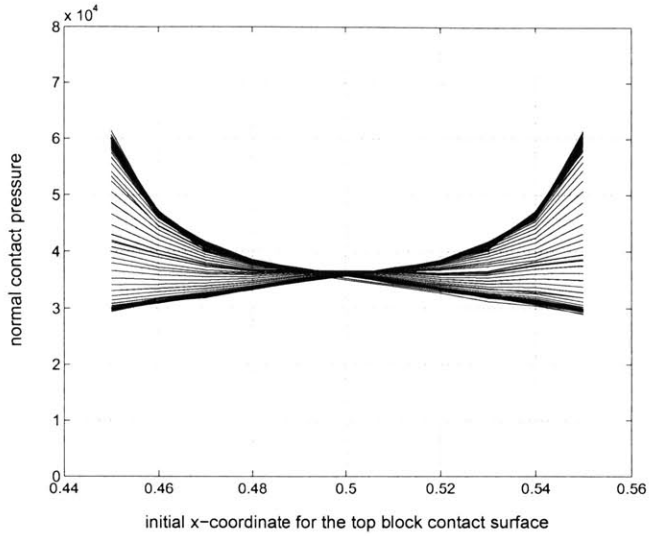

Figure 5-27: The normal contact distributions (for all time steps), 9-node elements; $p = 35000$.

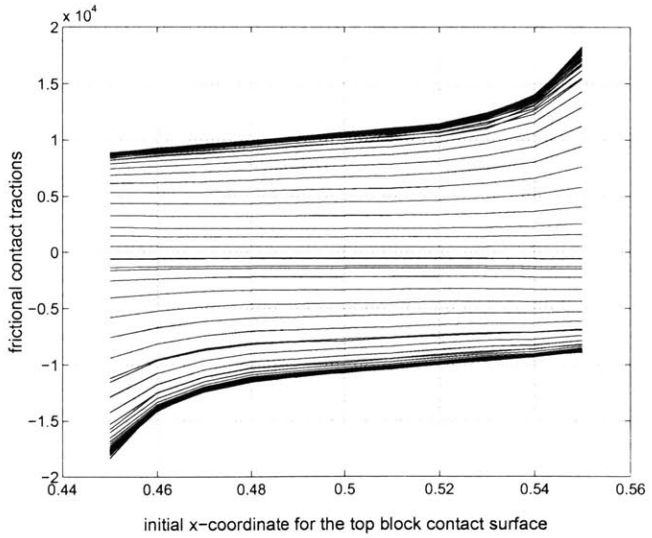

Figure 5-28: The frictional contact distributions (for all time steps), 9-node elements; $p = 35000$.

Chapter 6

A 3D Model Friction Problem and its Solution

6.1 Motivation

Solution of friction contact problems in a general three-dimensional setting is a challenging task. Much research has been conducted for the solution of 2D and 3D contact problems using the finite element method. Among the notable and early contributions in this regard is the solution scheme proposed in Bathe and Caudhary [8] and Chaudhary and Bathe [14] for problems with and without friction. The Coulomb friction model is commonly used for frictional behavior of contacting solids. For both frictionless and friction contact problems, inequality constraints have to be imposed on the equations governing the deformation response of the solid bodies. Constraint function method first proposed in this context in Eterovice and Bathe [21], changes these inequality constrains into a set of equality constraints by introducing appropriate constraint functions, while also regularizing the non-smoothness of contact constraints. This approach has been demonstrated to be very robust and accurate for a wide range of problems, Bathe and Bouzinov [6]. The solution algorithms were further extended to account for 2-D thermo-mechanical contact of solids in Pantuso and Bathe [34]. Other researchers have adopted perturbed Lagrange multiplier and augmented Lagrange multiplier methods. For detailed accounts on these methods,

see Zienkiewicz and Taylor [43] and Wriggers [41], and the references therein.

3D problems typically involve 2D planes coming into contact and sliding over, with or without friction. In the presence of friction accurate solution of such problems is significantly more complicated than similar problems in 2D. In 2D problems the situation is somewhat simplified as the contact surface is simply a curve, and the frictional contact forces are either acting in the direction of the local tangent vector, or opposite to it, see Bathe [3]. In contrast, in general 3D problems involving frictional sliding, the actual direction of sliding of a given point is not known, and must be calculated using appropriate information from the sliding history of the point. Kikuchi and Oden [25] provide a detailed variational framework for contact problems involving friction, and also look into the potential difficulties of non-smoothness and non-uniqueness of solutions that arise from the non-smoothness of local friction models.

In order to obtain insight in the solution of three-dimensional friction contact problems, a model problem is proposed and solved. The problem involves changes in magnitude and direction of the friction force and is formulated for solution using the constraint function algorithm. Particular attention is given to the numerical difficulties that arise in the Newton-Raphson iterations and to obtain solution accuracy in stick/slip conditions.

6.2 Frictional Sliding on a Plane

Figure 6-1 shows the spring-mass system considered, lying in the x-y plane. Point A represents the mass, connected to three linear springs with spring constants k_1, k_2 and k_3. The normal force N (possibly a function of x and y), is acting on the mass in the negative z-direction (i.e. into the paper). The applied force vector $\mathbf{R}$ is a function of time, its components R_x and R_y varying as functions of time $f_1(t)$ and $f_2(t)$. If $\mathbf{R}_c$ is the vector of frictional contact forces acting on the mass, and $\mathbf{F}$ is the vector

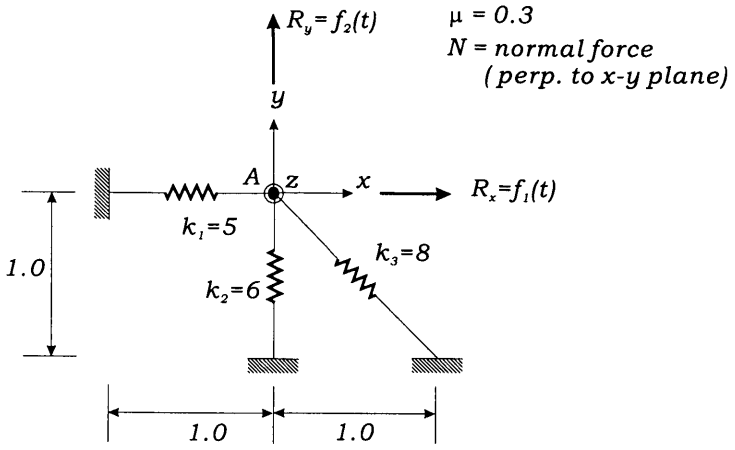

Figure 6-1: Frictional sliding of a point mass.

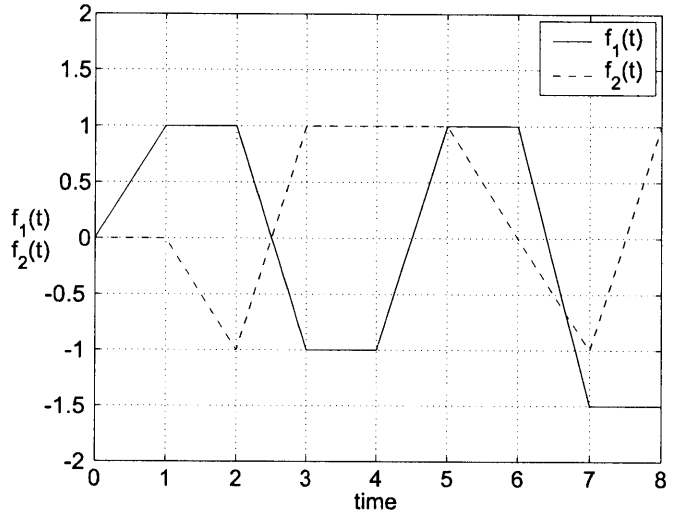

Figure 6-2: Time functions governing the variation of applied loads.

of spring forces, then the equilibrium relation at any given time t is

$$ {}^t\mathbf{R} + {}^t\mathbf{R}_c - {}^t\mathbf{F} = \mathbf{0} \tag{6.1} $$

Let T be the magnitude of the friction force, and let us define a non-dimensional parameter τ

$$ \tau = \frac{T}{\mu N} \tag{6.2} $$

where μ is the coefficient of friction. Let the velocity of the mass be $\mathbf{v}$, then the

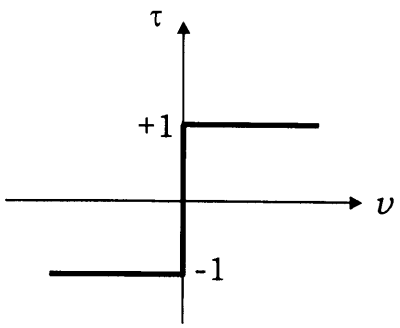

Figure 6-3: Coulomb friction condition.

tangential vector of the sliding trajectory is

$$\mathbf{s} = \frac{\mathbf{v}}{||\mathbf{v}||} \tag{6.3}$$

and we can define $v = \mathbf{v} \cdot \mathbf{s}$. Here v is the relative tangential velocity of the mass point relative to the stationary plane, and is equal to $||\mathbf{v}||$. Coulomb friction law can now be stated as

$$\begin{aligned} &|\tau| \leq 1 \\ &|\tau| < 1 \Longrightarrow v = 0 \\ &|\tau| = 1 \Longrightarrow \text{sign}(v) = \text{sign}(\tau) \end{aligned} \tag{6.4}$$

Eq. (6.4) is a general statement of the Coulomb friction law, depicted in Figure 6-3.

6.3 Numerical Algorithm

For the case considered, a point mass sliding on a rigid plane surface, of course no spatial discretization needs to be carried out. However the problem is nonlinear and time stepping scheme has to be employed to march through time, obtaining the solution at discrete time points Δt apart. The Euler backward finite difference approximation is used for the velocity vector

$${}^{t+\Delta t}\mathbf{v} = \frac{{}^{t+\Delta t}\mathbf{u} - {}^{t}\mathbf{u}}{\Delta t} \tag{6.5}$$

Based on the above relation, the components of the unit tangent vector **s** can be written in terms of the components of the displacement vector, as

$$\begin{aligned} s_x &= \frac{1}{l}({}^{t+\Delta t}u_x - {}^{t}u_x) \\ s_y &= \frac{1}{l}({}^{t+\Delta t}u_y - {}^{t}u_y) \end{aligned} \tag{6.6}$$

where l is the magnitude of the total incremental displacement,

$$l = \sqrt{({}^{t+\Delta t}u_x - {}^{t}u_x)^2 + ({}^{t+\Delta t}u_y - {}^{t}u_y)^2} \tag{6.7}$$

Constraint Function Method

The constraint function method is a regularizing technique which allows the treatment of the friction model without the need to differentiate between the stick and slip conditions. Define a function w_τ of the relative velocity v and τ, such that the solution of the equation $w_\tau(v, \tau) = 0$ satisfies Coulomb friction model given by Eq. 6.4. A suitable choice of function w_τ is given implicitly by the following expression

$$\tau + w_\tau = \frac{2}{\pi} \arctan\left(\frac{v - w_\tau}{\epsilon_\tau}\right) \tag{6.8}$$

where the parameter ϵ_τ provides a control over how closely the constraint function approximates Coulomb friction model in Eq. 6.4. Figure 6-4 shows the regularized friction law using a relatively large ϵ_τ value (for ease of visualization). For the complete solution of the problem, the constraint equation

$$w_\tau(v, \tau) = 0 \tag{6.9}$$

along with the equations of equilibrium, Eq. (6.1), need to be solved for the displacements and the frictional force parameter τ. This means, in essence, to look for a solution along the thick line shown on the surface generated in three dimensions by the constraint function w_τ, see figure 6-5. This line corresponds to $w_\tau = 0$. Also the derivatives of w_τ with respect to the relative velocity v and τ are plotted against v,

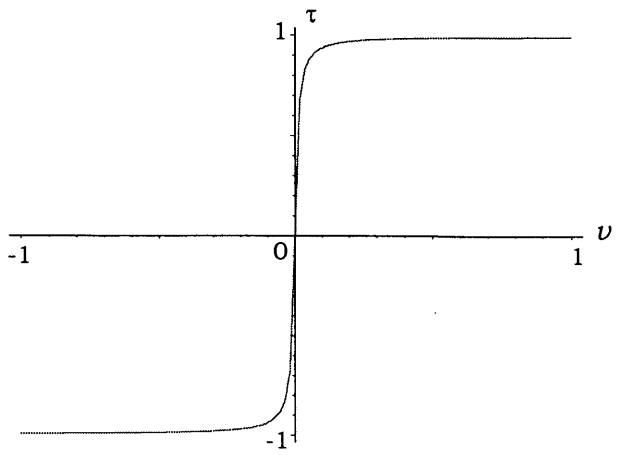

Figure 6-4: Regularization of Coulomb friction by constraint function.

for the case of $w_\tau = 0$, in Figures 6-6 and 6-7. As the constraint function parameter ϵ_τ approaches zero, sharper spikes are obtained, clearly showing the high degree of non-smoothness (close to the stick conditions) in these derivatives.

6.4 Linearization of Governing Equations

The Eqs. (6.1) and (6.9) constitute a set of nonlinear equations to be solved for the unknowns $\Delta\mathbf{u}$ and $\Delta\tau$. The Newton-Raphson method is the most commonly used solution technique for solving a nonlinear system of equations. The resulting incremental equations are obtained by linearizing about the most recently calculated state. This results in the following system of equations, which correspond to the first iteration for solution at time $t + \Delta t$, in which the unknowns are the increments in the displacement $\Delta\mathbf{u}$ and the frictional parameter $\Delta\tau$

$$\begin{bmatrix} \mathbf{K} + {}^t\mathbf{K}^c_{uu} & {}^t\mathbf{K}^c_{u\tau} \\ {}^t\mathbf{K}^c_{\tau u} & {}^t\mathbf{K}^c_{\tau\tau} \end{bmatrix} \begin{bmatrix} \Delta\mathbf{u} \\ \Delta\tau \end{bmatrix} = \begin{bmatrix} {}^{t+\Delta t}\mathbf{R} + {}^t\mathbf{R}_c - {}^t\mathbf{F} \\ {}^tF_c = w_\tau \end{bmatrix} \tag{6.10}$$

where

$${}^t\mathbf{R} = \begin{bmatrix} R_x(t) \\ R_y(t) \end{bmatrix}; \quad {}^t\mathbf{R}_c = \begin{bmatrix} -\mu\,\tau\,N\,s_x \\ -\mu\,\tau\,N\,s_y \end{bmatrix}; \quad {}^t\mathbf{F} = \mathbf{K}\,{}^t\mathbf{u} \tag{6.11}$$

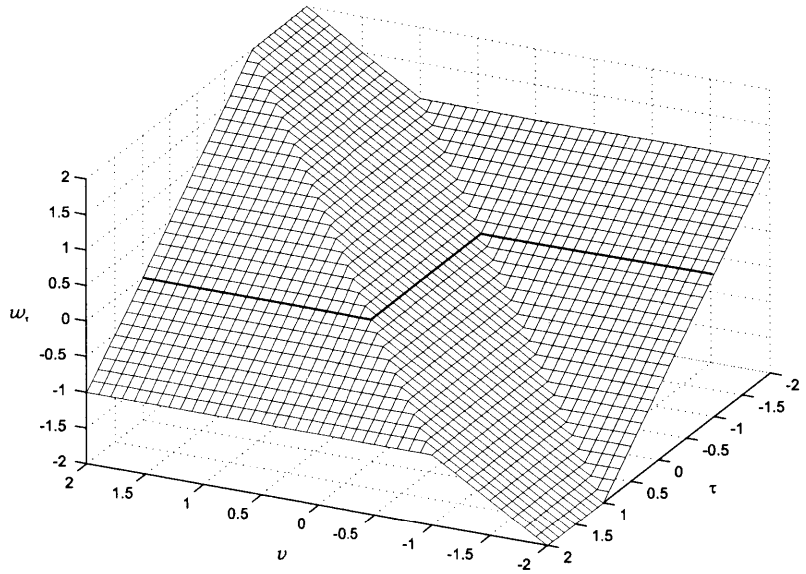

Figure 6-5: The surface generated by the constraint function in Eq. (6.8). The thick line corresponds to $w_\tau = 0$.

with $\mathbf{K}$ being the linear stiffness matrix corresponding to the spring stiffnesses, and ${}^t\mathbf{u} = [{}^t u_x \quad {}^t u_y]^T$ the total displacement vector at time t. ${}^t\mathbf{K}^c_{uu}$, ${}^t\mathbf{K}^c_{u\tau}$, ${}^t\mathbf{K}^c_{\tau u}$ and ${}^t\mathbf{K}^c_{\tau\tau}$ are the contact stiffness matrices, given by

$$\begin{aligned} {}^t\mathbf{K}^c_{uu} &= -\frac{\partial\, {}^t\mathbf{R}_c}{\partial\, {}^t\mathbf{u}}; \qquad {}^t\mathbf{K}^c_{u\tau} = -\frac{\partial\, {}^t\mathbf{R}_c}{\partial\, {}^t\tau} \\ {}^t\mathbf{K}^c_{\tau u} &= -\frac{\partial\, {}^t F_c}{\partial\, {}^t\mathbf{u}}; \qquad {}^t\mathbf{K}^c_{\tau\tau} = -\frac{\partial\, {}^t F_c}{\partial\, {}^t\tau} \end{aligned} \tag{6.12}$$

The details of these matrices are as follows,

$${}^t\mathbf{K}^c_{uu} = \begin{bmatrix} \tau\mu N\frac{\partial s_x}{\partial u_x} + \tau\mu s_x\frac{\partial N}{\partial u_x} & \tau\mu N\frac{\partial s_x}{\partial u_y} + \tau\mu s_x\frac{\partial N}{\partial u_y} \\ \tau\mu N\frac{\partial s_y}{\partial u_x} + \tau\mu s_y\frac{\partial N}{\partial u_x} & \tau\mu N\frac{\partial s_y}{\partial u_y} + \tau\mu s_y\frac{\partial N}{\partial u_y} \end{bmatrix} \tag{6.13}$$

$${}^t\mathbf{K}^c_{u\tau} = \begin{bmatrix} \mu N s_x \\ \mu N s_y \end{bmatrix} \tag{6.14}$$

$${}^t\mathbf{K}^c_{\tau u} = -\begin{bmatrix} \frac{\partial w_\tau}{\partial v}\frac{\partial v}{\partial u_x} & \frac{\partial w_\tau}{\partial v}\frac{\partial v}{\partial u_y} \end{bmatrix} \tag{6.15}$$

$$ {}^{t}\mathbf{K}^{c}_{\tau\tau} = -\frac{\partial w_\tau}{\partial \tau} \tag{6.16} $$

These expressions for the contact stiffness matrices involve the derivatives of the components of the tangent vector $\mathbf{s}$, s_x and s_y, with respect to u_x and u_y. Using Eq. (6.6)

$$ \begin{aligned} \frac{\partial s_x}{\partial u_x} &= \frac{({}^{t+\Delta t}u_y - {}^{t}u_y)^2}{l^3} \\ \frac{\partial s_x}{\partial u_y} &= -\frac{({}^{t+\Delta t}u_x - {}^{t}u_x)({}^{t+\Delta t}u_y - {}^{t}u_y)}{l^3} \\ \frac{\partial s_y}{\partial u_x} &= -\frac{({}^{t+\Delta t}u_x - {}^{t}u_x)({}^{t+\Delta t}u_y - {}^{t}u_y)}{l^3} \\ \frac{\partial s_y}{\partial u_y} &= \frac{({}^{t+\Delta t}u_x - {}^{t}u_x)^2}{l^3} \end{aligned} \tag{6.17} $$

It is important to note that during each iteration for a given time step, the velocity vector $\mathbf{v}$ is computed using the *total* incremental displacement for the time step, i.e.

$$ \mathbf{v}^{(i)} = \frac{{}^{t+\Delta t}\mathbf{u}^{(i)} - {}^{t}\mathbf{u}}{\Delta t} \tag{6.18} $$

Also at the start of each time step, i.e. for the first iteration, the velocity vector computed for the previous time step, at convergence, is used.

6.5 Numerical Results

The problem is first solved with $N = 1$, and the time functions $f_1(t)$ and $f_2(t)$ as shown in Figure 6-2. The applied load vector is changing direction rapidly. A time step size $\Delta t = 1$ is used for the analysis, with the constraint function parameter $\epsilon_\tau = 10^{-5}$. This is the largest time step possible to resolves the time functions given in Figure 6-2 exactly. The convergence tolerance used is 10^{-12} for the norm of the incremental displacement vector $||\Delta\mathbf{u}||$ and the norm of out-of-balance loads $||\mathbf{R} + \mathbf{R}_c - \mathbf{F}||$.

The trajectory of point A is plotted using the x-y coordinates in Figure 6-8. Since the applied load vector does not change from time $t = 3$ to $t = 4$, the point mass is expected to be in a state of sticking. This is clear from the trajectory, where the

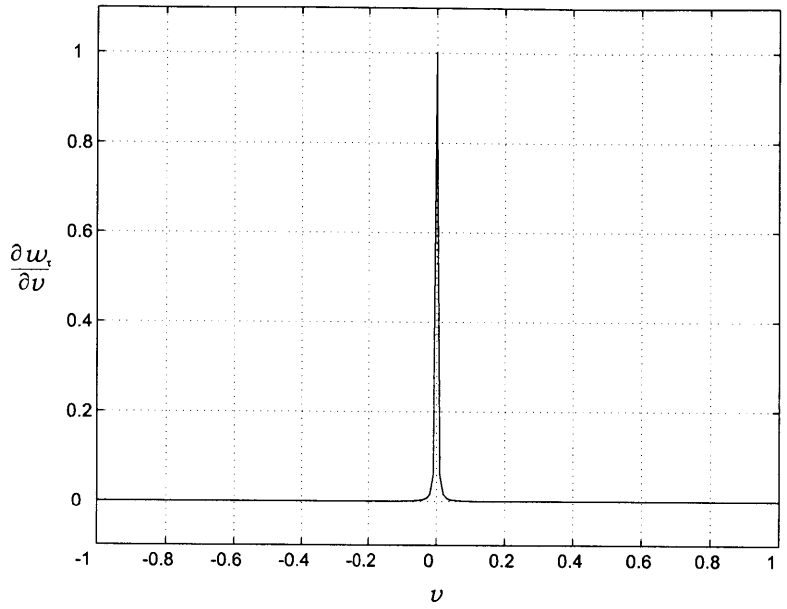

Figure 6-6: The derivative of w_t w.r.t. $\dot{u}$, $\frac{\partial w_t}{\partial \dot{u}}$; for $w_t = 0$.

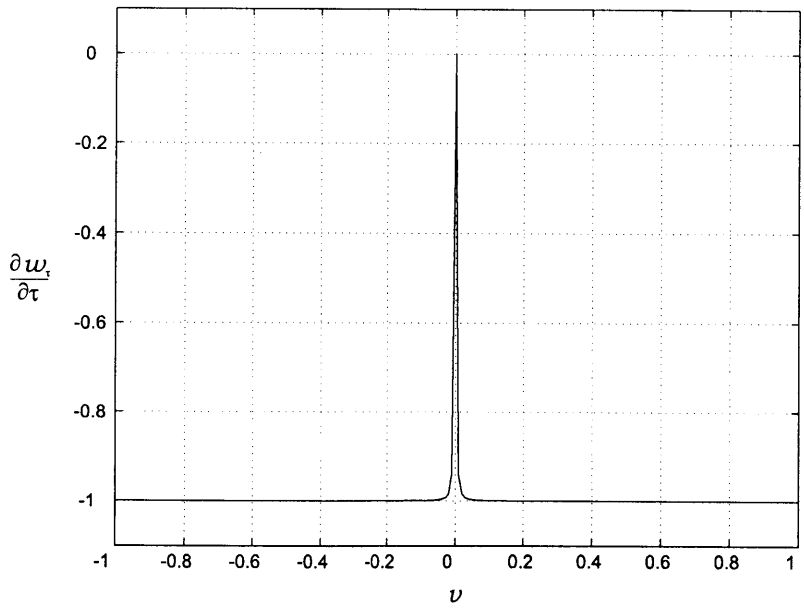

Figure 6-7: The derivative of w_t w.r.t. τ, $\frac{\partial w_t}{\partial \tau}$; for $w_t = 0$.

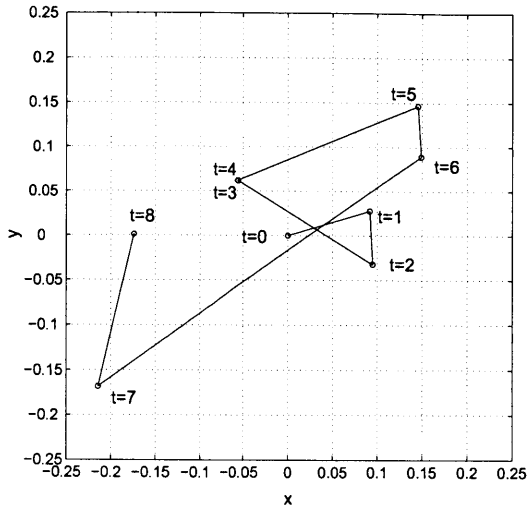

Figure 6-8: The trajectory of point A, under the action of applied loads; $\Delta t = 1$, $\epsilon_t = 10^{-5}$, $N = 1$.

positions at times $t = 3$ and $t = 4$ are seen to coincide. Figure 6-9 gives a plot of the incremental applied load vector, which shows how the direction of the force applied to the point mass changes, its components being governed by the time functions given in Figure 6-2. Figure 6-10 shows the incremental friction force vectors for all time steps. Clearly, the magnitude of the friction force never exceeds the limiting value (0.3). Similarly, Figure 6-11 shows the incremental spring force vectors. Figure 6-12 shows the vector diagrams of the incremental forces at each time point, clearly demonstrating that equilibrium is satisfied, i.e. all the incremental forces are in equilibrium,

$$\Delta\mathbf{R} + \Delta\mathbf{R}_c - \Delta\mathbf{F} = \mathbf{0} \tag{6.19}$$

There is no vector plot for time $t = 4$ as the increments in force vectors are all exactly zero corresponding to this time point. This figure shows the complexity of the solution obtained: the three incremental force vectors are hardly ever acting along the same line

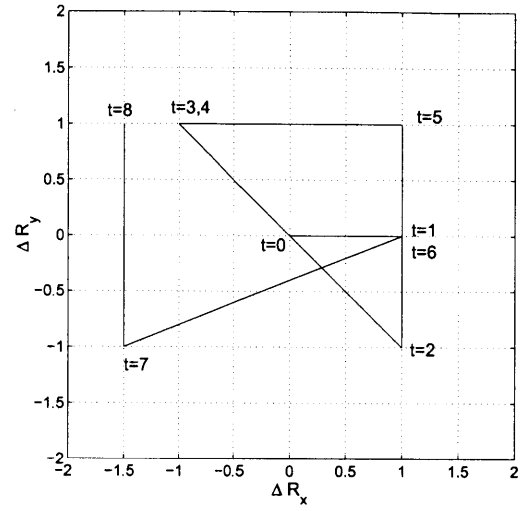

Figure 6-9: Plot of incremental applied load vectors; $\Delta t = 1$.

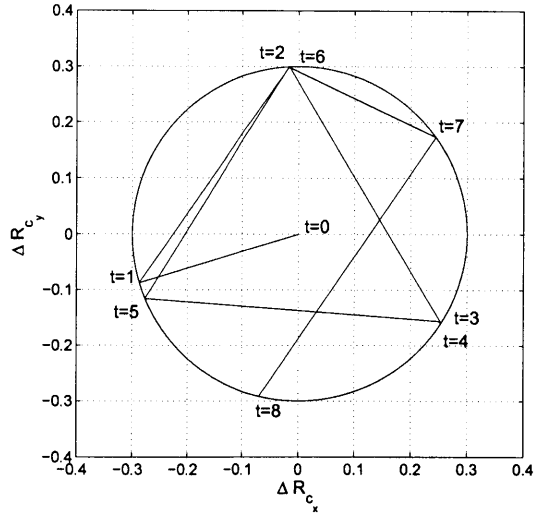

Figure 6-10: Plot of incremental friction force vectors; $\Delta t = 1$, $\epsilon_t = 10^{-5}$, $N = 1$.

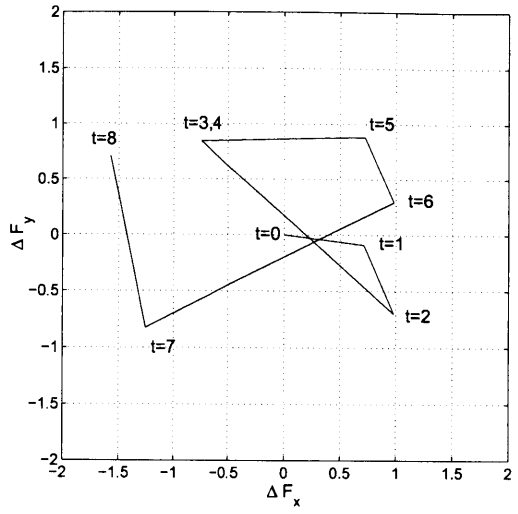

Figure 6-11: Plot of incremental internal spring force vectors; $\Delta t = 1$, $\epsilon_t = 10^{-5}$, $N = 1$.

6.5.1 Accuracy of Solution

It is instructive to solve the problem using smaller time steps, and to compare the trajectories obtained. To this end, we solve the problem using successively smaller time step sizes, for a total time duration of $2\,s$. Figure 6-13 shows the plots obtained when using $\Delta t = 1$, $\Delta t = 0.25$ and $\Delta t = 0.1$.

The trajectory calculated using smaller time steps is more curved than that obtained using a large time step, even though the direction of increment in load vector remains the same (as it does from $t = 0$ to $t = 1$, and from $t = 1$ to $t = 2$). The nonlinearity is due to the friction force vector, which although keeping a constant magnitude during sliding, is changing its direction, such that it always acts in a direction opposite to that of the total incremental displacement vector during a time step. The inaccuracy in the trajectory calculated with $\Delta t = 1$ is not just limited to not being able to resolve the curvature of the trajectory; the positions at times $t = 1$ and $t = 2$ are also not calculated accurately compared to when using $\Delta t = 0.25$ and $\Delta t = 0.1$. But it is interesting to note that the total distance covered by the point mass agrees quite closely for all three time step sizes used. The trajectories obtained for a total duration of $8\,s$ using $\Delta t = 1$ and $\Delta t = 0.1$ are plotted in Figure 6-14. The increments in the friction force vector are plotted in Figure 6-15. All the points

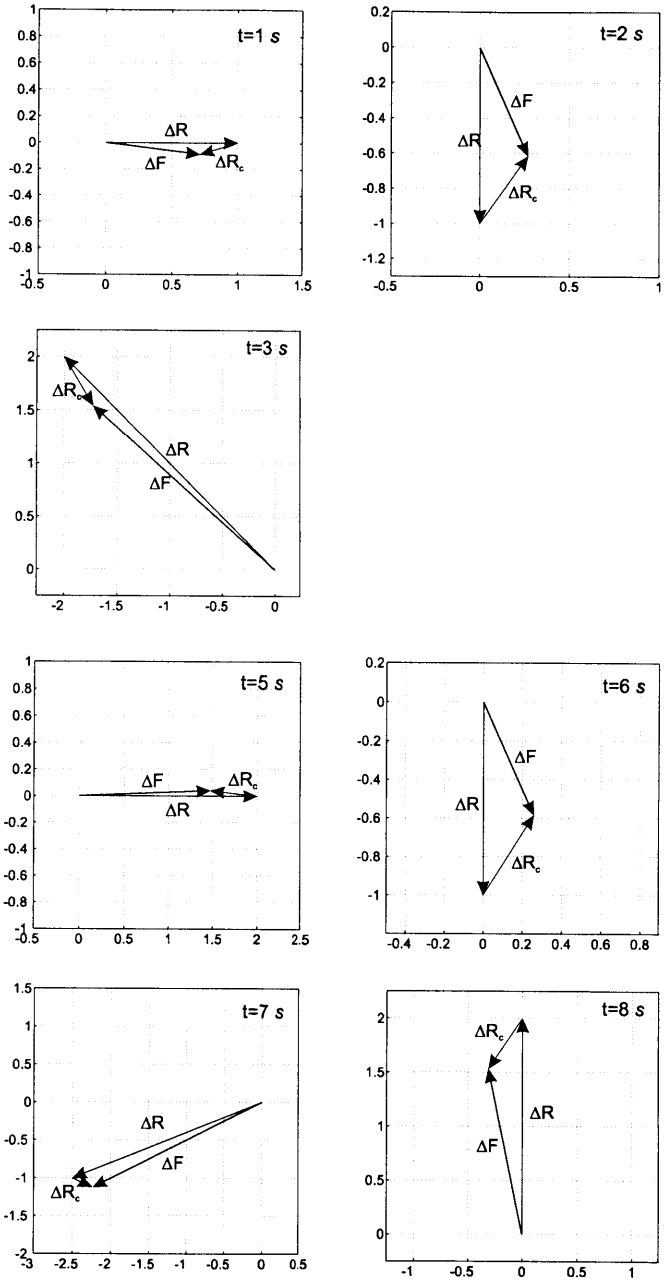

Figure 6-12: Plots of incremental load, spring force and friction force vectors at each time step; the three incremental force vectors are in equilibrium.

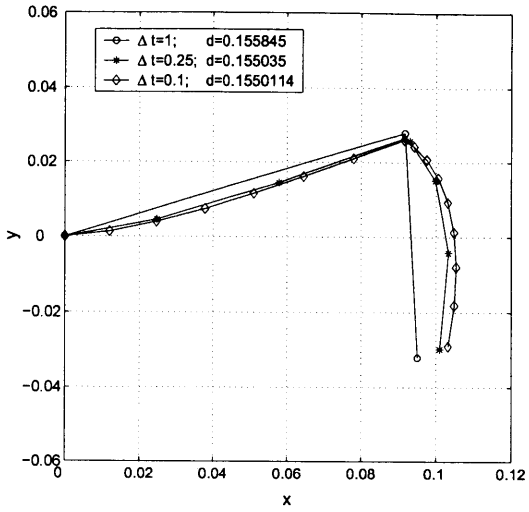

Figure 6-13: Comparison of the trajectory of point A, for different values of time step size Δt; $\epsilon_t = 10^{-5}$; (for total duration of $2\,s$).

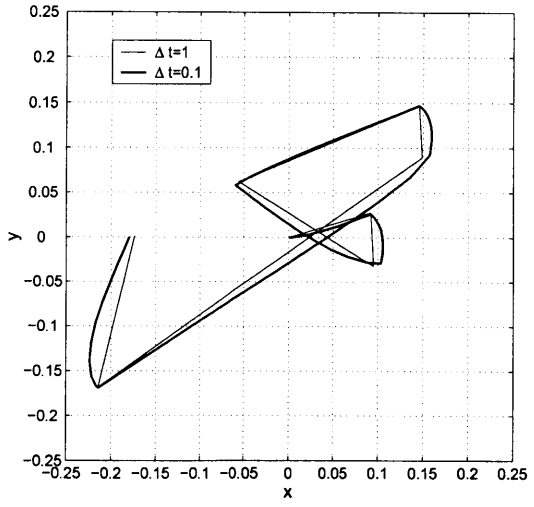

Figure 6-14: Comparison of the trajectory of point A, obtained using $\Delta t = 1$ and $\Delta t = 0.1$; (for total duration of $8\,s$).

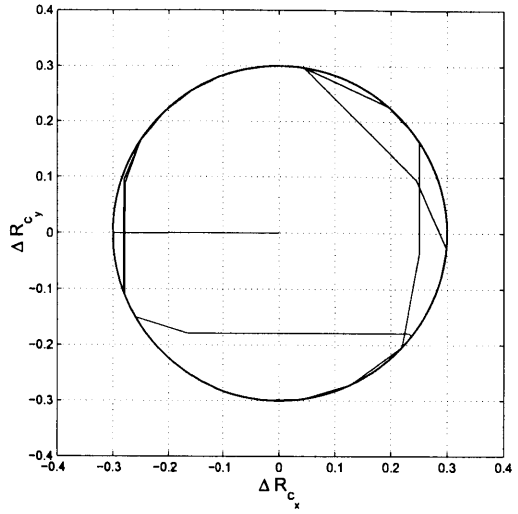

Figure 6-15: Plot of incremental friction force vectors; $\Delta t = 0.1$, $\epsilon_\tau = 10^{-5}$, $N = 1$. The circle shows the limiting value for the frictional force magnitude; at no time is this threshold violated. Points lying within the circle indicate a stick condition.

either lie on the circle, corresponding to slip condition, or within the circle signifying a stick state.

6.5.2 Convergence of Newton-Raphson Iterations

Table 6.1 shows the convergence norms obtained using $\Delta t = 1.0$ at some of the time steps. Quadratic convergence is observed at all time steps. From time $t = 3$ to time $t = 4$, no change in the magnitude *and* direction of applied force occurs, and hence not only the incremental displacement is zero, but also the incremental friction force vector. Therefore only in one iteration the convergence tolerances are satisfied, and no change occurs in the state of the system.

The question that naturally arises is: "What happens with the convergence in the Newton-Raphson iterations if the time step is reduced?"

Assuming a sufficiently small time step size, consider the time step when the load vector changes its direction. For a very small step size, we have a *near stick* condition. Namely, the applied load vector changes very little, the magnitude of the friction force vector $\mathbf{R}_c$, changes very little as well, and an almost zero incremental displacement is obtained. When such a condition is encountered during Newton-Raphson iterations,

Table 6.1: Convergence norms for some time steps; $\Delta t = 1$, $\epsilon_t = 10^{-5}$, $N = 1$

Time step	Iteration no.	$\|\|\Delta \mathbf{u}\|\|$	$\|\|\mathbf{R} + \mathbf{R_c} - \mathbf{F}\|\|$
1	3	4.502944×10^{-2}	3.089381×10^{-1}
	4	5.126421×10^{-3}	4.708601×10^{-2}
	5	6.692529×10^{-5}	5.100840×10^{-4}
	6	8.691213×10^{-9}	7.484651×10^{-8}
	7	5.187049×10^{-16}	1.383957×10^{-15}
3	1	2.110848×10^{-1}	2.828427×10^{0}
	2	4.339628×10^{-2}	5.500720×10^{-1}
	3	9.072446×10^{-4}	7.378370×10^{-3}
	4	3.341192×10^{-7}	3.927812×10^{-6}
	5	4.058864×10^{-14}	2.880263×10^{-13}
4	1	5.894603×10^{-17}	6.206335×10^{-17}
8	2	1.019709×10^{-1}	5.786315×10^{-1}
	3	2.340038×10^{-3}	2.115516×10^{-2}
	4	5.006491×10^{-6}	3.118794×10^{-5}
	5	1.750116×10^{-11}	1.278661×10^{-10}
	6	3.855375×10^{-16}	2.154412×10^{-16}

convergence may not be achieved using a very small value of the constraint function parameter (e.g. 10^{-5}). The reason for this lack of convergence can be attributed to the fact that the derivatives of the constraint function with respect to both v and τ are highly non-smooth for small values of v, see Figures 5 and 6. These derivatives appear in the matrices $\mathbf{K}^c_{\tau u}$ and $\mathbf{K}^c_{\tau\tau}$, and during Newton-Raphson iterations their values may jump suddenly from 1 to 0 or vice versa. Also during the iterations, the direction of $\mathbf{s}$ changes and may oscillate between successive iterations. These difficulties mean that convergence may not be reached in the full Newton-Raphson iterations when using a very small value for the constraint function parameter (e.g. $\epsilon_\tau = 10^{-5}$). Indeed, to obtain the solution with step size $\Delta t = 0.25$ and $\Delta t = 0.1$, a Newton-Raphson increment was calculated in each iteration, but then the following expression was used to update the unknown variables

$$\begin{bmatrix} {}^{t+\Delta t}\mathbf{u}^{(i)} \\ {}^{t+\Delta t}\tau^{(i)} \end{bmatrix} = \begin{bmatrix} {}^{t+\Delta t}\mathbf{u}^{(i-1)} \\ {}^{t+\Delta t}\tau^{(i-1)} \end{bmatrix} + \alpha \begin{bmatrix} \Delta \mathbf{u}^{(i)} \\ \Delta \tau^{(i)} \end{bmatrix} \tag{6.20}$$

where α is a scalar multiplier. The out-of-balance load $({}^{t+\Delta t}\mathbf{R} + {}^{t+\Delta t}\mathbf{R}_c^{(i)} - {}^{t+\Delta t}\mathbf{F}_c^{(i)})$

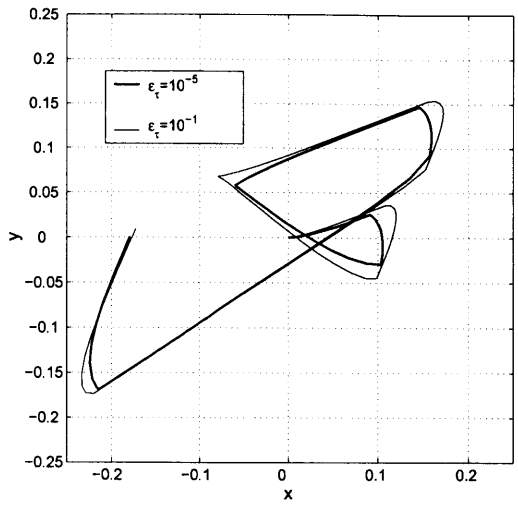

Figure 6-16: Comparison of trajectory of point A, for different values of ϵ_t; time step size $\Delta t = 0.1$, $N = 1$.

was then calculated using these updated displacements, and α was then varied until the magnitude of the out-of-balance loads decreased to the required level, i.e.

$$||^{t+\Delta t}\mathbf{R} + {}^{t+\Delta t}\mathbf{R}_c^{(i)} - {}^{t+\Delta t}\mathbf{F}_c^{(i)}|| \leq STOL\,||^{t+\Delta t}\mathbf{R} + {}^{t+\Delta t}\mathbf{R}_c^{(i-1)} - {}^{t+\Delta t}\mathbf{F}_c^{(i-1)}|| \quad (6.21)$$

with $STOL$ being a line search tolerance.The use of this line search procedure facilitated obtaining the solution with the convergence tolerances defined earlier, but the quadratic convergence rate then may be lost.

Using a larger constraint function parameter eliminates the convergence difficulties, but the solution accuracy is reduced. This can be seen in Figure 6-16, which shows the trajectories obtained by setting $\epsilon_\tau = 10^{-5}$ and $\epsilon_\tau = 10^{-1}$, with time step size $\Delta t = 0.1$. Clearly, the trajectory obtained with the larger ϵ_τ overshoots the point where there is a sudden change in direction in the accurate solution. This is expected since the stick-like conditions are relaxed when using a larger parameter value.

The same experiences are also obtained when solving the problem using a radial-return algorithm approach [26], see Appendix.

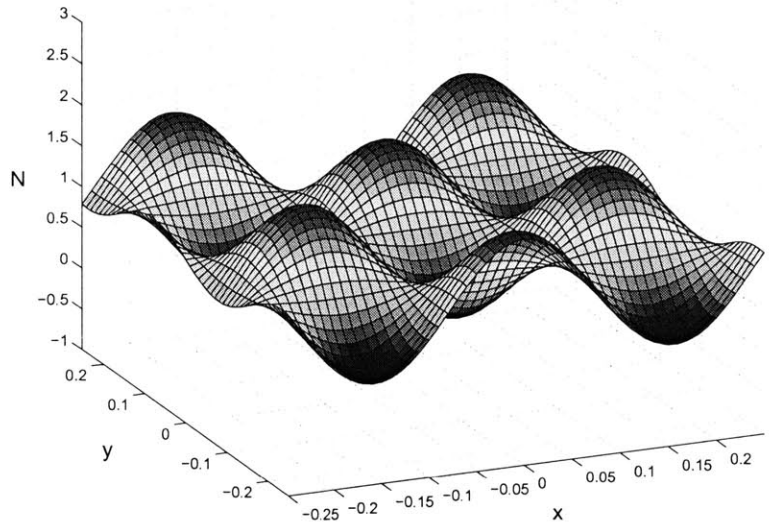

Figure 6-17: Variation of normal force; $N = 1 + 0.8\sin(20x)\cos(20y)$.

6.5.3 Variable Normal Force N

Next the problem is solved using a variable normal force, i.e. $N = N(x, y) = 1 + 0.8\sin(20x)\cos(20y)$, see Figure 6-17. The dependence of N on the coordinates adds to the nonlinearity of the problem, requiring that derivatives of N with respect to x and y be computed. This makes the matrix ${}^t\mathbf{K}^c_{uu}$ also non-symmetric as can be seen in Eq. 6.13.

As above, we used the constraint function parameter $\epsilon_\tau = 10^{-5}$ and the time step $\Delta t = 0.1$. For comparison, the trajectory is plotted along with that obtained using a constant normal force $N = 1$. Figure 6-18 shows these results. With this small time step, similar convergence difficulties were encountered as with a constant normal force. However using a larger value of ϵ_τ again resulted in quadratic convergence of the full Newton-Raphson method.

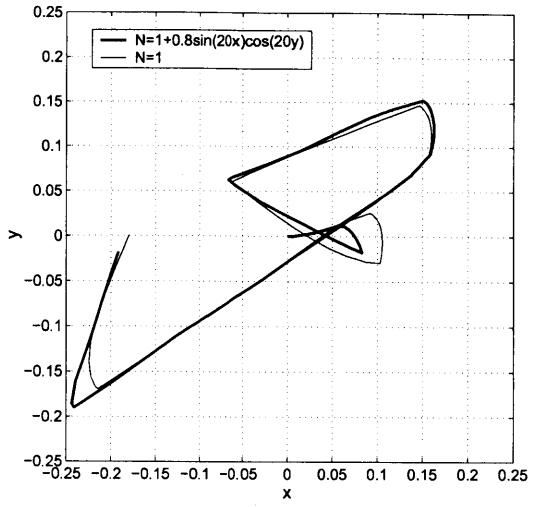

Figure 6-18: Comparison of trajectories obtained; $\epsilon_t = 10^{-3}$, $\Delta t = 0.1$.

6.6 Conclusions

A study is carried out of a model 3D friction problem, using Coulomb friction law, involving sliding of a point on a plane surface. The friction model was regularized by means of the constraint function method.

The use of large time steps resulted in successful solutions in the Newton-Raphson iterations although time step size then may not be small enough to resolve the trajectory accurately. For greater accuracy, smaller time steps are required, and then the transition from stick to slip is also calculated. At those times where the applied force vector changes directions and/or transition from stick to slip takes place, difficulties are encountered in achieving convergence in the iterations, due to the high degree of nonlinearity in the friction conditions. Convergence can be restored if recourse is made to a line search procedure during each Newton-Raphson iteration.

Appendix

It is insightful to consider the problem solution from a so-called 'radial return type algorithm' perspective [26]. In this algorithm the contact force vector is evaluated and then pulled back to the limiting surface defined by the frictional resistance capacity

Table 6.2: The 'radial return algorithm' for the solution of the model problem

1. Establish linear stiffness matrix $\mathbf{K}$.
2. IF $(||^{t+\Delta t}\mathbf{u}^{(i-1)} - {}^{t}\mathbf{u}|| > 0)$ THEN
   - set ${}^{t+\Delta t}\mathbf{R}_c^{(i-1)} = -\mu N\mathbf{s}$, where $\mathbf{s}$ is computed as in Section 2. Linearization follows as shown in Section 3: ${}^{t+\Delta t}\mathbf{K}^{(i-1)} = \mathbf{K} + \mathbf{K}_{uu}^{c}$; compute incremental displacements.
   - GOTO step 5.

   ELSE
   - GOTO step 3.
3. Estimate the friction force vector as ${}^{t+\Delta t}\mathbf{R}_c^{(i-1)} = -{}^{t+\Delta t}\mathbf{R} + {}^{t+\Delta t}\mathbf{F}^{(i-1)}$. Calculate $r = \frac{||^{t+\Delta t}\mathbf{R}_c^{(i-1)}||}{\mu N}$.
   IF $(r \leq 1.0)$ THEN
   - Accept the friction force vector. GOTO step 5.

   ELSE
   - GOTO step 4.
4. Correct the friction force vector as ${}^{t+\Delta t}\mathbf{R}_c^{(i-1)} = \frac{-{}^{t+\Delta t}\mathbf{R} + {}^{t+\Delta t}\mathbf{F}^{(i-1)}}{r}$. The coefficient matrix is then ${}^{t+\Delta t}\mathbf{K}^{(i-1)} = \mathbf{K} - \frac{\partial \mathbf{R}_c}{\partial \mathbf{u}}$, where $\frac{\partial \mathbf{R}_c}{\partial \mathbf{u}}$ is the gradient of $\mathbf{R}_c$ computed taking into account dependency of r on $\mathbf{F}$. Compute increments in displacements.
5. Repeat iteration (GOTO step 2) until convergence.

μN. The unknowns are only the displacements, and for the problem considered the coefficient matrix will be of size 2×2 In the following a constant N is assumed. The algorithm proceeds as given in Table 6.2.

For time step size $\Delta t = 1$, the algorithm produced exactly the same result as obtained using the constraint function algorithm, with quadratic convergence. However, using a small time step, e.g. $\Delta t = 0.25$ and 0.1, convergence difficulties same as those observed using the constraint function algorithm with $\epsilon_\tau = 10^{-5}$ were encountered. Again, the use of a line search method helps in obtaining a convergent and accurate solution. All the solution results that were obtained using the constraint function method were also obtained using this algorithm, with imperceptible differences in results.

Chapter 7

Conclusions

A contact solution algorithms for 2D problems in continuum mechanics is presented. The algorithm and implementation extend the idea of sub-segments presented in [18].The approach is Lagrange multiplier based, and the contact traction variable are interpolated to the same order over contact segments as the order underlying continuum finite elements. This results in optimal convergence and stability of the solution scheme. The contact integral is evaluated explicitly using numerical quadrature over all the subsegments. Linearization of each term in the contact integral is carried out without assuming the order of the contact segments. Once the interpolation order is known based on the finite elements used, the interpolation order of the contact traction variable is chosen accordingly, and then appropriate substitutions made in the linearized terms obtained earlier. The further division of contactor segments into subsegments based on target segment end nodes' projection enables the method to pass the contact patch test, resulting in the above mentioned optimal convergence rates. The inequality constraints arising due to contact conditions are handled using the constraint function method, first introduced in [19, 21]. The approach conveniently transforms the problem into that of equality constraints, regularizing the non-smooth contact conditions at the same time.

The resulting contact algorithm is a synthesis of the two approaches, and performs well for contact analysis of bodies undergoing large displacements. The geometry of the contact surfaces correspond to the geometry of the finite element model. As

pointed out in ref.[20], the continuity of second derivatives of the contact surface is required to obtain quadratic convergence of Newton-Raphson method. This is also seen in the linearized terms in Chapter 2. However, the presented algorithm is a segment approach, with all the linearized terms of the contact integral evaluated at integration points within the subsegments, avoiding the nodal locations where the normal vector is not uniquely defined (jump in the second derivative). Chapters 2 and 3 presented the linearization of the contact integral and details of the algorithm, along with numerical examples.

The objective of Chapter 4 was to present in detail a simple composite direct time integration scheme for nonlinear dynamic analysis for problems involving large displacements. The commonly used implicit schemes that are unconditionally stable in linear analysis, do not retain this desirable property in nonlinear solutions. The composite scheme presented is an extension of the approach first suggested in ref. [2] and also used in ADINA program for fully coupled solution of fluid-structure interactions. In the context of dynamic analysis of structural and solid mechanics problems, the scheme also seems to be a suitable choice for use in instances where the contribution to the response from higher modes is negligible and the use of a relatively larger time step size is warranted, see also refs. [1, 5]. Traditional schemes lose stability in such cases, and more involved procedures to retain stability may become overly complicated, resulting in a non-symmetric coefficient matrix (even when contact conditions are not present), and also being dependent on element and material model used, see ref. [36, 30]. For dynamic analysis involving contact, the composite scheme is used along with the contact solution algorithm of Chapter 3. The dissipative nature of the time integrator stabilizes the solution at the instants of contact events, without performing any additional post-processing of the solution to correct velocity and acceleration at the contact nodes. Even without such post-processing, the solution quality is seen to be good in Chapter 5 where numerical examples involving dynamic contact analysis are presented. Also friction problems involving large sliding are solved successfully using this combination of algorithms.

Chapter 6 focuses on a model friction problem in 3D. For problems in 3D, the

frictional force vector acts over a plane rather than a curve as in 2D problems of Chapters 2 and 3. The tangent vector **s** can not be obtained merely from the geometry of the contact surface, but has to be evaluated based on the direction of the relative velocity between contacting surfaces. In the model problem, sliding of a point over a plane surface was investigated, using the constraint function algorithm. The transition from slip to stick poses numerical difficulties, with lack of convergence in full Newton-Raphson iterations. Similar convergence behavior was also observed using an algorithm that evaluated the friction force vector based on the magnitude of relative velocity, forcing the magnitude of friction force to stay within the limit imposed by Coulomb friction model. Using a line search procedure restored convergence in the case of both algorithms.

Regarding future work in the context of the solution algorithm presented, it would be interesting to see the performance of the sub-segmenting approach in full 3D analysis. In 3D, each sub-segment would be formed based on the projection of the edges of target contact elements onto the contactor elements. The sub-segments may not remain simple triangles or quadrilaterals, but may now be multifaceted polygons. Some results using such an approach for frictionless contact and low order elements have been reported in Puso and Laursen[35], but an implementation using the constraint function method is more desirable, since it allows use of larger time steps and better convergence during time steps when contact establishes or releases. Moreover, for high order elements, e.g. 27-node brick element, each face of a subsegment may now be a parabola. Smart and effective data structures need to be considered for such a situation, to keep track of bounding edges and nodes lying on these. Effective means have to be devised to perform numerical quadrature over this (curved sided) polygon . Also, it would be very interesting to see how friction forces are handled in 3D, in light of the issues (although simplified) encountered in Chapter 6.

Appendix A

Energy and Momentum Conservation

In this section we briefly review the conservation properties of mechanical systems, specifically bodies coming into contact. We state the conservation laws and look at the conditions under which, in the presence of contact conditions these laws are satisfied.

Conservation of Energy

The total energy of an isolated system of n bodies, possibly coming into contact, remains unchanged. This balance of energy is expressed by the following relation:

$$\Delta(KE) + \Delta(SE) = W_{external} + W_{contact} - W_{dissipated} \tag{A.1}$$

where KE is the total kinetic energy of the system, SE is the total strain energy stored in the bodies, $W_{external}$ is the work done by the externally applied forces, $W_{contact}$ is work done by the contact forces, and $W_{dissipated}$ is the internal energy dissipation that might result due to plastic deformations of the contacting bodies. The law of conservation of energy can be expressed in terms of the rates of change of kinetic and

strain energy and all the work terms in the above expression, as

$$\frac{d(KE)}{dt} + \frac{d(SE)}{dt} = P_{external} + P_{contact} - P_{dissipated} \tag{A.2}$$

Conservation of Momenta

In the absence of any externally applied the loads (body and surface loads), the total linear and angular momenta of an isolated system of n contacting bodies remain constant. Let $\boldsymbol{J}_L$ and $\boldsymbol{J}_\omega$ be the total linear and angular momentum respectively of the system, given by

$$\boldsymbol{J}_L = \sum_i \left\{ \int_{{}^tV} {}^t\rho \dot{\mathbf{u}} \, d\,{}^tV \right\} \tag{A.3}$$

$$\boldsymbol{J}_\omega = \sum_i \left\{ \int_{{}^tV} {}^t\rho \mathbf{x} \times \dot{\mathbf{u}} \, d\,{}^tV \right\} \tag{A.4}$$

The rate of change of momenta can then be written as

$$\frac{d\boldsymbol{J}_L}{dt} = \sum_i \left\{ \int_{{}^tV} {}^t\rho \ddot{\mathbf{u}} \, d\,{}^tV \right\} \tag{A.5}$$

$$\frac{d\boldsymbol{J}_\omega}{dt} = \sum_i \left\{ \int_{{}^tV} {}^t\rho \mathbf{x} \times \ddot{\mathbf{u}} \, d\,{}^tV \right\} \tag{A.6}$$

Conservation of linear momentum directly gives us

$$\frac{d\boldsymbol{J}_L}{dt} = 0 \tag{A.7}$$

$$\frac{d\boldsymbol{J}_\omega}{dt} = 0 \tag{A.8}$$

Conservation Laws for Contacting Bodies

In order to look closely at the conditions under which these conservation laws hold in the presence of contact, we concentrate on the equation of virtual work, and consider the case of only two bodies coming into contact $i = 1, 2$. We will subsequently make the following assumptions, to simplify the analysis:

- There is no plastic deformation taking place in either of the contacting bodies, so that the total internal dissipation is exactly zero.
- The contacting bodies are not subject to any externally applied body forces or surface forces.
- The area on the surface of bodies, with prescribed displacements is zero. With this assumption we allow rigid body displacement modes of the system.

The equation of virtual work for two bodies is

$$\sum_i \left\{ \int_{{}^tV} {}^t\rho\ddot{\mathbf{u}} \cdot \delta\mathbf{u}\, d^tV \right\} + \sum_i \left\{ \int_{{}^tV} {}^t\boldsymbol{\tau} \cdot \delta_t\mathbf{e}\, d^tV \right\} = \sum_i \left\{ \int_{{}^tV} {}^t\mathbf{f}^B \cdot \delta\mathbf{u}\, d^tV + \int_{{}^tS_f} {}^t\mathbf{f}^S \cdot \delta\mathbf{u}^S\, d^tS \right\} + \int_{{}^tS_c} {}^t\mathbf{f}^c \cdot (\delta\mathbf{u}^2 - \delta\mathbf{u}^1)\, d^tS \tag{A.9}$$

where $\delta\mathbf{u}$ is the variation in displacements imposed on configuration at time t, and $\delta_t\mathbf{e}$ is virtual strain tensor corresponding to the virtual displacement $\delta\mathbf{u}$. The first term on LHS represents the virtual work due to inertia forces.

In order to prove that the linear momentum is conserved, we choose the virtual displacement (variation in $\mathbf{u}$, $\delta\mathbf{u}$) equal to a constant vector $\mathbf{a}$, i.e $\delta\mathbf{u} = \mathbf{a}$ which is in the space of admissible functions (assuming there are zero Dirichlet boundary conditions). This results in the following expression

$$\sum_i \left\{ \int_{{}^tV} {}^t\rho\ddot{\mathbf{u}} \cdot \mathbf{a}\, d^tV \right\} - \int_{{}^tS_c} {}^t\mathbf{f}^c \cdot (\mathbf{a} - \mathbf{a})\, d^tS = 0 \tag{A.10}$$

$$\mathbf{a} \cdot \frac{d\boldsymbol{J}_L}{dt} = 0 \tag{A.11}$$

Here we have assumed zero external body forces and surface tractions. The above equation hold for any arbitrary vector $\mathbf{e}$, and this proves that the linear momentum is conserved,

$$\frac{d\boldsymbol{J}_L}{dt} = 0 \tag{A.12}$$

Next, to prove that the total angular momentum is conserved, we choose, in the equation of virtual work A.9, $\delta\mathbf{u} = \mathbf{a} \times \mathbf{x}$, where $\mathbf{a}$ is a constant vector. This results in

$$\sum_i \left\{ \int_{{}^tV} {}^t\rho\ddot{\mathbf{u}} \cdot (\mathbf{a} \times \mathbf{x})\, d^tV \right\} = \int_{{}^tS_c} {}^t\mathbf{f}^c \cdot [\mathbf{a} \times (\mathbf{x}^2 - \mathbf{x}^1)]\, d^tS \tag{A.13}$$

where we have made use of the fact that the virtual strains corresponding to this virtual rigid body rotation are zero, and no body or externally applied forces are present. This equation is the same as

$$\sum_i \left\{ \int_{{}^tV} \mathbf{a} \cdot (\mathbf{x} \times {}^t\rho\ddot{\mathbf{u}})\, d^0V \right\} = \int_{{}^tS_c} \mathbf{a} \cdot [{}^t\mathbf{f}^c \times (\mathbf{x}^2 - \mathbf{x}^1)]\, d^tS \tag{A.14}$$

$$\mathbf{a} \cdot \frac{d\boldsymbol{J}_\omega}{dt} = 0 \tag{A.15}$$

where the RHS reduces to zero since at the contacting surfaces, the points $\mathbf{x}^1$ and $\mathbf{x}^2$ coincide as the gap is reduced to zero. Since $\mathbf{e}$ is an arbitrary constant vector, it follows that the angular momentum is conserved,

$$\frac{d\boldsymbol{J}_\omega}{dt} = 0 \tag{A.16}$$

To look at the rate of change of energy of the system, we now, replace the variation in displacements $\delta\mathbf{u}$ by $\dot{\mathbf{u}}$ in the equation of virtual work. This choice of variation is in the space of admissible functions because of the assumption that no displacement boundary conditions exist. Moreover, we assume no internal energy dissipation. Using this variation in the equation of virtual work A.9, one obtains

$$\sum_i \left\{ \int_{{}^tV} {}^t\rho\ddot{\mathbf{u}} \cdot \dot{\mathbf{u}}\, d^tV \right\} + \sum_i \left\{ \int_{{}^tV} {}^t\boldsymbol{\tau} \cdot {}^t\mathbf{D}\, d^tV \right\} = \int_{{}^tS_c} {}^t\mathbf{f}^c \cdot (\dot{\mathbf{u}}^2 - \dot{\mathbf{u}}^1)\, d^tS \tag{A.17}$$

where ${}^t\mathbf{D}$ is the velocity strain tensor, see [3] for details. Recall that ${}^t\mathbf{f}^c = \lambda\mathbf{n} + t\mathbf{s}$, with λ being the normal contact force and t the tangential frictional force, acting on the target surface at point $\mathbf{x}^2$. The above equation is written in the following

simplified form,

$$\frac{d(KE)}{dt} + \frac{d(SE)}{dt} = \int_{{}^tS_c} {}^t\lambda\, \mathbf{n} \cdot (\dot{\mathbf{u}}^2 - \dot{\mathbf{u}}^1)\, d^tS + \int_{{}^tS_c} {}^tt, \mathbf{s} \cdot (\dot{\mathbf{u}}^2 - \dot{\mathbf{u}}^1)\, d^tS \qquad \text{(A.18)}$$

Using similar steps that were used in Chapter 2 to compute δg the variation of gap, the rate of change of gap can be obtained,

$$\dot{g} = (\dot{\mathbf{u}}^2 - \dot{\mathbf{u}}^1) \cdot \mathbf{n} \qquad \text{(A.19)}$$

Also $\frac{d(E)}{dt} = \frac{d(KE)}{dt} + \frac{d(SE)}{dt}$ is the rate of change of total energy of the system. Using the above two expressions, one readily obtains

$$\frac{d(E)}{dt} = \int_{{}^tS_c} {}^t\lambda \dot{g}\, d^tS + \int_{{}^tS_c} {}^tt\, \mathbf{s} \cdot (\dot{\mathbf{u}}^2 - \dot{\mathbf{u}}^1)\, d^tS \qquad \text{(A.20)}$$

If frictionless contact is assumed then the second term on the RHS of the above equation vanishes. In the absence of friction, the system should evolve without loss of energy, and therefore for conservation of energy to be satisfied, i.e. $\frac{d(E)}{dt} = 0$, one finds that the following conditions should be satisfied,

$$\begin{aligned} g &\geqslant 0 \\ \lambda &\geqslant 0 \\ g\lambda &= 0 \\ \dot{g}\lambda &= 0 \end{aligned} \qquad \text{(A.21)}$$

The first three conditions are the Kuhn-Tucker conditions already stated in Chapter 2. The fourth condition actually guarantees that in elastic contact, no energy is either lost or created. Note that if this condition is violated, i.e. $\dot{g}\lambda \neq 0$, energy will be taken out the system (since $\dot{g} < 0$) as contact establishes, and introduced into the system as contact is released ($\dot{g} > 0$).

In the case of frictional contact, the second term in the above equation of rate of change of total energy has to be considered. Since ${}^tt$ acts on the target surface at

point $\mathbf{x}^2$, the direction of ${}^t t\mathbf{s}$ will be always opposite to that of $(\dot{\mathbf{u}}^2 - \dot{\mathbf{u}}^1)$, and hence the term will have a negative sign in case of sliding contact, leading to the general statement

$$\frac{d(E)}{dt} \leq 0 \tag{A.22}$$

This expression guarantees that the energy of the system is either lost or at best conserved, proving energy stability of the system.

Bibliography

[1] M.M.I. Baig and K.J. Bathe. On direct time integration in large deformation dynamic analysis. In K.J. Bathe, editor, *Proceedings of the Third MIT conference on computational fluid and solid mechanics*, pages 1044–1047, Cambridge, 2005. Elsevier.

[2] R.E. Bank, W.M. Coughran Jr, W. Fichtner, E.H. Grosse, D.J. Rose, and R.K. Smith. Transient simulations of silicon devices and circuits. *IEEE Trans CAD*, 4:436–451, 1985.

[3] K.J. Bathe. *Finite Element Procedures.* Prentice Hall, 1996.

[4] K.J. Bathe. "ADINA" system. *Encyclopaedia of Mathematics*, 11:33–35, 1997.

[5] K.J. Bathe and M.M.I. Baig. On a composite implicit time integration procedure for nonlinear dynamics. *Computers & Structures*, 83:2513–2524, 2005.

[6] K.J. Bathe and P.A. Bouzinov. On the constraint function method for contact problems. *Computers & Structures*, 64:1069–1085, 1997.

[7] K.J. Bathe and F. Brezzi. Stability of finite element mixed interpolations for contact problems. *Atti della Accademia Nazionale dei Lincei, s.9*, 12:159–166, 2001.

[8] K.J. Bathe and A.B. Chaudhary. A solution method for planar and axisymmetric contact problems. *Int J Num Methods Engrg*, 21:65–88, 1985.

[9] K.J. Bathe, E. Ramm, and E.L. Wilson. Finite element formulations for large deformation dynamic analysis. *Int J Num Methods Engrg*, 9:353–386, 1975.

[10] K.J. Bathe and E.L. Wilson. Stability and accuracy analysis of direct integration methods. *Int J Earthquake Eng and Struct Dynamics*, 1:283–291, 1973.

[11] K.J. Bathe and H. Zhang. Finite element developments for general fluid flows with structural interactions. *Int J Num Methods Engrg*, 60:213–232, 2004.

[12] D.P. Bertsekas. *Constrained Optimization and Lagrange Multiplier Methods.* Academic Press, New York, 1982.

[13] F. Brezzi and M. Fortin. *Mixed and Hybrid Finite Element Methods.* Springer-Verlag, New York, 1991.

[14] A.B. Chaudhary and K.J. Bathe. A solution method for static and dynamic analysis of three-dimensional contact problems with friction. *Computers & Structures*, 24:855–873, 1986.

[15] J. Chung and G.M. Hulbert. A time integration algorithm for structural dynamics with improved numerical dissipation: the generalized-α method. *J App Mech, Transactions of the ASME*, 60:371–375, 1993.

[16] P.G. Ciarlet. *The Finite Element Method for Elliptic Problems.* North Holland, 1978.

[17] L. Collatz. *The Numerical Treatment of Differential Equations, 3rd ed.* Springer-Verlag, New York, 1966.

[18] N. El-Abbasi and K.J. Bathe. Stability and patch test performance of contact discretizations and a new solution algorithm. *Computers & Structures*, 79:1473–1486, 2001.

[19] A.L. Eterovic. *Finite Element Analysis of Large Deformation Contact Problems.* PhD thesis, Massachusetts Institute of Technology, Department of Civil and Engineering, 1992.

[20] A.L. Eterovic and K.J. Bathe. An interface interpolation scheme for quadratic convergence in the finite element analysis of contact problems. In *Nonlinear Computational Mechanics–State of the Art*, Berlin, 1991. Springer-Verlag.

[21] A.L. Eterovic and K.J. Bathe. On the treatment of inequality constraints arising from contact conditions in finite element analysis. *Computers & Structures*, 40:203–209, 1991.

[22] T.J.R. Hughes. *The Finite Element Method: Linear Static and Dynamic Finite Element Analysis.* Prentice Hall, 1987.

[23] T.J.R. Hughes, T.K. Caughey, and W.K. Liu. Finite element methods for nonlinear elastodynamics which conserve energy. *J App Mech, Transactions of the ASME*, 45:366–370, 1978.

[24] B. Irons and A. Razzaque. Experience with the patch test for convergence of finite elements. In A.K. Aziz, editor, *The Mathematical Foundations of the Finite Element Method with Applications to Partial Differential Equations*, pages 557–587. Academic Press, 1972.

[25] N. Kikuchi and J.T. Oden. *Contact Problems in Elasticity: A Study of Variational Inequalities and Finite Element Methods. SIAM*, 1988.

[26] M. Kojić and K.J. Bathe. *Inelastic Analysis of Solids and Structures.* Springer, 2005.

[27] D. Kuhl and M.A. Crisfield. Energy-conserving and decaying algorithms in nonlinear structural dynamics. *Int J Num Methods Engrg*, 45:569–599, 1999.

[28] D. Kuhl and E. Ramm. Constraint energy momentum algorithm and its application to nonlinear dynamics of shells. *Comp Methods in App Mech and Engrg*, 136:293–315, 1996.

[29] T.A. Laursen and V. Chawla. Design of energy conserving algorithms for frictionless dynamic contact problems. *Int J Num Methods Engrg*, 40:863–886, 1997.

[30] T.A. Laursen and X.N. Meng. A new solution procedure for application of energy-conserving algorithms to general constitutive models in nonlinear elastodynamics. *Comput Methods Appl Mech Engrg*, 190:6309–6322, 2001.

[31] T.A. Laursen and J.C. Simo. Algorithmic symmetrization of coulomb frictional problems using augmented lagrangians. *Comp Methods App Mech and Engrg*, 109:133–146, 1993.

[32] S. Mijailovich and K.J. Bathe. A finite element solution method for 2-D contact-impact problems. Technical Report 88-1, Massachusetts Institute of Technology, Department of Mechanical Engineering, 1988.

[33] J.T. Oden. Exterior penalty methods for contact problems in elasticity. In W. Wunderlich, E. Stein, and K.J. Bathe, editors, *Nonlinear Finite Element Analysis in Structural Mechanics*, pages 655–665. Springer-Verlag, 1980.

[34] D. Pantuso, K.J. Bathe, and P.A. Bouzinov. A finite element procedure for the analysis of thermo-mechanical solids in contact. *Computers & Structures*, 75:551–573, 2000.

[35] M.A. Puso and T.A. Laursen. A mortar segment-to-segment contact method for large deformation solid mechanics. *Comp Methods App Mech Engrg*, 193:601–629, 2004.

[36] J.C. Simo and N. Tarnow. The discrete energy-momentum method. conserving algorithms for nonlinear elastodynamics. *Z angew Mathematical Physics*, 43:757–792, 1992.

[37] J.C. Simo, P. Wriggers, and R.L. Taylor. A perturbed lagrangian formulation for the finite element solution of contact problems. *Comp Methods App Mech and Engrg*, 50:163–180, 1985.

[38] G. Strang and G.J. Fix. *An Analysis of the Finite Element Method.* Wellesley-Cambridge Press, 1997.

[39] S.P. Timoshenko and J.N. Goodier. *Theory of Elasticity.* McGraw-Hill, 1970.

[40] E.L. Wilson, I. Farhoomand, and K.J. Bathe. Nonlinear dynamic analysis of complex structures. *Int J Earthquake Eng and Struct Dynamics*, 1:283–291, 1973.

[41] P. Wriggers. *Computational Contact Mechanics.* John Wiley & Sons Ltd., 2002.

[42] B. Yang, T.A. Laursen, and X. Meng. Two dimensional mortar contact methods for large deformation frictional sliding. *Int J Num Method Engrg*, 62:1183–1225, 2005.

[43] O.C. Zienkiewicz and R.L. Taylor. *The Finite Element Method; Vols 1,2 &3, Fifth Edition.* Butterworth-Heinemann, 2000.